



Theoretical study of reduced tantalum pentoxide for memristive applications

Pedersen, Christian Søndergaard

Publication date:
2020

Document Version
Publisher's PDF, also known as Version of record

[Link back to DTU Orbit](#)

Citation (APA):
Pedersen, C. S. (2020). *Theoretical study of reduced tantalum pentoxide for memristive applications*. Technical University of Denmark.

General rights

Copyright and moral rights for the publications made accessible in the public portal are retained by the authors and/or other copyright owners and it is a condition of accessing publications that users recognise and abide by the legal requirements associated with these rights.

- Users may download and print one copy of any publication from the public portal for the purpose of private study or research.
- You may not further distribute the material or use it for any profit-making activity or commercial gain
- You may freely distribute the URL identifying the publication in the public portal

If you believe that this document breaches copyright please contact us providing details, and we will remove access to the work immediately and investigate your claim.

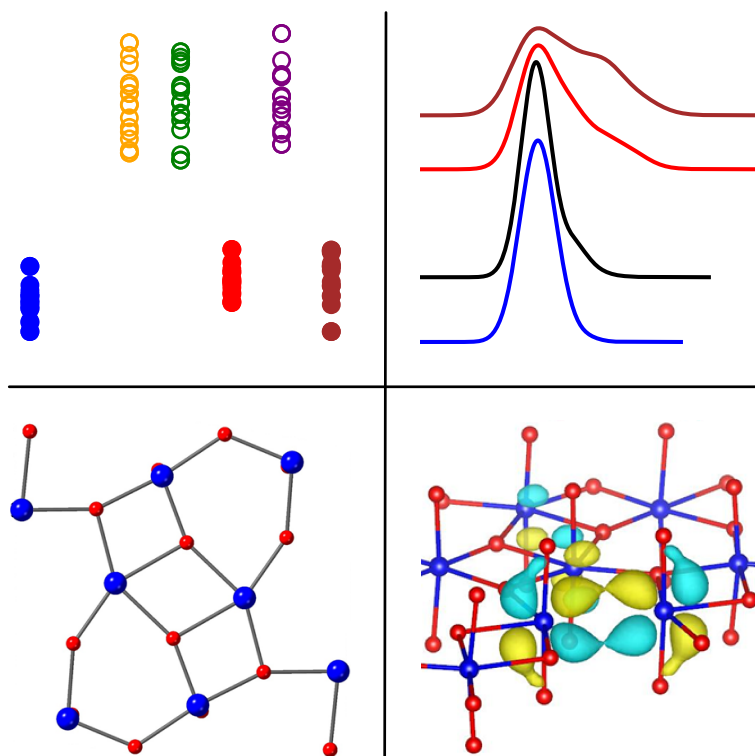
Theoretical study of reduced tantalum pentoxide for memristive applications

Ph.D. Thesis

Technical University of Denmark

Department of Energy Conversion and Storage

Christian Søndergaard Pedersen



Theoretical study of reduced tantalum pentoxide for memristive applications

PhD Thesis

Author

Christian Søndergaard Pedersen

E-mail: chrsop@dtu.dk

Supervisors

Associate Professor Juan María García Lastra
Section for Atomic Scale Materials Modelling
Department of Energy Conversion and Storage
Technical University of Denmark
E-mail: jmgl@dtu.dk

Assistant Professor Jin Hyun Chang
Section for Atomic Scale Materials Modelling
Department of Energy Conversion and Storage
Technical University of Denmark
E-mail: jchang@dtu.dk

Professor Tejs Vegge
Section for Atomic Scale Materials Modelling
Department of Energy Conversion and Storage
Technical University of Denmark
E-mail: teve@dtu.dk

Professor Nini Pryds
Section for Functional Oxides
Department of Energy Conversion and Storage
Technical University of Denmark
E-mail: nipr@dtu.dk

Department of Energy Conversion and Storage

Section for Atomic Scale Materials Modelling
Anker Engelunds Vej, building 301
2800 Kgs. Lyngby
Denmark
www.asm.energy.dtu.dk
E-mail: info@energy.dtu.dk

Submitted August 31st, 2020

Abstract

Resistive Random Access Memory devices are regarded as the successor to existing Flash memory technology. One of the promising materials for use in such devices is tantalum oxide, which is endorsed by industry giants Samsung, Hewlett-Packard, and Panasonic. Despite its success as a resistive switching material, much remains unknown about its switching behaviour. Resistive layers are frequently reported to consist of insulating, oxygen-rich surface layers and a conducting, oxygen-deficient bulk region, while switching operations rely on generating large quantities of oxygen vacancies in the surface layers. To date, few theoretical studies have examined atomic-level phenomena of oxygen-deficient tantalum oxide, while none have achieved the rigour necessary to search for oxygen-deficient phases that may be generated as part of fabrication or switching processes. This dissertation presents three investigations designed to gain atomic-level insight into TaO_x resistive layers.

First, a large-scale study of amorphous tantalum oxide with varying oxygen content is performed to search for possible intermediate stoichiometries between Ta_2O_5 and TaO_2 . Structures are compared in terms of total energies, simulated XPS spectra, and Bader charge spectra. By sampling multiple structures of each stoichiometry, the analysis is able to conclude that some stoichiometries are clearly lower in energy than others. Low total energy is related to increased sixfold coordination of Ta atoms, and to the existence of crystalline Group V metal oxide phases of same stoichiometry. The XPS analysis reproduces the Ta^{5+} and Ta^{4+} peaks reported in literature, and finds that the XPS spectrum of stoichiometric TaO_2 contains a strong signal from Ta_2O_5 . The study of amorphous tantalum oxide concludes with a partial reproduction of an experimental XPS depth profile.

Second, a study of crystalline λ -phase tantalum oxide is performed, where oxygen deficiency is modelled by introducing oxygen vacancies. The vast configuration space for distribution of multiple oxygen vacancies presents a challenge in terms of study size, which is overcome by accelerating the search with the machine-learning approach known as Cluster Expansion. The study establishes a new metastable phase, Ta_4O_9 , which is stable with respect to phase separation between Ta_2O_5 and TaO_2 . The stability of the Ta_4O_9 phase arises from a unique defect structure, in which defects aggregate pair-wise with no decrease of coordination number anywhere in the system. The defect states are spatially localised, and bear character of the d orbitals of neighbouring Ta atoms. Finally, a search among documented crystalline Group V metal oxide phases finds three hitherto unknown stable or metastable structures. These are $\text{Ta}_{11}\text{O}_{27}$, $\text{Ta}_{12}\text{O}_{29}$, and TaO – all of them based on niobium oxide structures.

Third, a parametrisation of tantalum oxide is developed for the Density Functional Tight-Binding code DFTB+. The tight-binding approach presents a desirable boost to computational speed, which can scale calculations up to realistic device sizes. The parametrisation is benchmarked against DFT-obtained results with respect to lattice parameters and oxygen vacancy formation energies, and shows good performance for modelling amorphous Ta_2O_5 .

The results presented in this dissertation provide important atomic-level knowledge of the behaviour of both amorphous and crystalline tantalum oxide. Several avenues for further study are opened, in particular pertaining to the discovery of in total five new stable or metastable structures. Further, the parametrisation of Ta–O for Density Functional Tight-Binding allows studying of realistic devices, and helps speed up future studies of amorphous tantalum oxide.

Resumé

Resistiv Random Access Memory-enheder anses for at være efterfølgeren til eksisterende Flash Memory-teknologi. Et af de lovende materialer for brug i sådanne enheder er tantaloxid, som anvendes af industrigiganterne Samsung, Hewlett-Packard og Panasonic. På trods af materialets succes indenfor resistiv skiftning, er der meget som endnu ikke vides om dets omskiftningsadfærd. Resistive lag rapporteres ofte som bestående af isolerende, oxygenrige overfladelag, og en ledende, oxygenmanglende bulk. Til dags dato har få teoretiske studier undersøgt fænomener i tantaloxid på atomær skala, mens ingen har opnået den grundighed, det kræver at søge efter, finde og karakterisere metastabile faser i tantal-oxygensystemet. Denne afhandling præsenterer tre undersøgelser, som er tilrettelagt med det formål at opnå indsigt i TaO_x på atomær skala.

Først udføres et studie i amorf tantaloxid med varierende oxygenindhold, med henblik på at søge efter mulige intermediære støkiometrier mellem Ta_2O_5 og TaO_2 . Strukturer sammenlignes med hensyn til totalenergi, simulerede XPS-spektra og Bader-ladningsspektra. Ved at sample adskillige strukturer af hver støkiometri er analysen i stand til at konkludere, at visse støkiometrier tydeligt har lavere energi end andre. Lav totalenergi er relateret til øget seksfoldig koordination af Ta-atomer, samt til eksistens af krystalline Gruppe V metaloxidfaser med samme støkiometri. XPS-analysen genskaber de Ta^{5+} - og Ta^{4+} -peaks, som rapporteres i litteraturen, og opdager desuden at XPS-spektret fra støkiometrisk TaO_2 indeholder et kraftigt signal fra Ta_2O_5 . Studiet afsluttes med en delvis genskabelse af en eksperimentel XPS-dybdeprofil.

Dernæst udføres et studie i krystallinsk tantaloxid i λ -fasen, hvor oxygenmangel modelleres ved introduktion af oxygenvacancer. Det enorme konfigurationsrum for fordeling af flertallige oxygenvacancer udgør en udfordring for så vidt angår studiets størrelse, hvilket imødegås ved hjælp af maskinlæringsmetoden kendt som Cluster Expansion. Studiet fastslår en ny metastabil fase, Ta_4O_9 , som er stabil i forhold til faseseparation mellem Ta_2O_5 og TaO_2 . Stabiliteten opstår af fasens unikke defektstruktur, i hvilken defekter samles parvist uden nedgang i koordinationstal for noget atom i systemet. Defekternes tilstande er lokaliserede i rum og besidder karakter af f-orbitalerne fra Ta naboomer. Sluttelig søges der mellem dokumenterede krystallinske Gruppe V-metaloxidfaser, hvor tre hidtil ukendte stabile eller metastabile strukturer opdages. Disse er $\text{Ta}_{11}\text{O}_{27}$, $\text{Ta}_{12}\text{O}_{29}$ og TaO – allesammen baseret på strukturer af nioboxid.

Endelig udvikles en parametrisering af tantaloxid for Tæthedsfunktional-Tight-Binding-koden DFTB+. Tight-Binding-metoden indebærer en ønskværdig forøgelse af beregnings-hastigheden, som kan skalere beregninger op til størrelsen af realistiske enheder. Parametriseringen evalueres i forhold til gitterparametre og energier for dannelse af oxygenvacancer, og udviser god duelighed til modellering af amorf Ta_2O_5 .

Resultaterne i denne afhandling giver vigtig indsigt i både amorf og krystallinsk tantaloxid på atomær skala. Adskillige muligheder for fremtidige studier åbnes, særligt vedrørende opdagelserne af samlet set fem nye stabile eller metastabile strukturer. Endvidere tillader parametriseringen af tantaloxid at enheder på realistiske størrelser kan studeres, og bidrager til at øge hastigheden af fremtidige studier af amorf tantaloxid.

Acknowledgements

Christian Søndergaard Pedersen, PhD student, DTU

First and foremost, I would like to thank my project supervisor, Associate Professor Juan María García Lastra, for his efforts in directing this work towards something useful. Thanks to my co-supervisor, Assistant Professor Jin Hyun Chang, whose phenomenally critical gaze and do-or-die work ethic have served as examples to follow. Thanks to Professor Tejs Vegge for creating an open and pleasant research department that I have been happy to be a part of. And thanks to Professor Nini Pryds and Doctor Yang Li for their hard work on the experimental part of the project; work which has inspired more than one investigation in this thesis.

Besides supervisors and collaborators, I wish to extend my gratitude to Professor Thomas Frauenheim of BCCMS at Universität Bremen for inviting me to study and work within his research group. Assistance with DFTB parametrization is acknowledged of Dennis Franke and Bálint Aradi of BCCMS, Jolla Kullgren and Akshay Kandy of Uppsala University, as well as Lee Taeho of DTU Energy. Thanks to Alexander Sougaard Tygesen for his Python skills, for proofreading the manuscript, and for aiding with the document setup. Henrik Høgh Kristoffersen of DTU Physics has provided invaluable counsel on molecular dynamics simulations in particular. Thanks to Steen Lysgaard for maintaining software, in particular installing VMD on Nifheim at my request. Thanks to Karina Ulvskov Frederiksen at DTU Energy for lending her considerable organisational skills on numerous occasions when my own failed. *Gracias a Merche, José Angel, Diego y Alejandra por cuidarse de mi hijo. Tak til mine forældre, Jesper og Lone, og deres respektive partnere, Mai og Peter.* Finally, a very special thanks goes to my partner, Alba, and our son, Ragnar. Alba has worked hard to make sure I had time for preparing this thesis, while Ragnar has worked equally hard to make sure I did not. Both efforts are greatly appreciated.

Contents

Abstract	iv
Resume	v
Acknowledgements	vi
Table of Contents	vii
List of Figures	ix
1 Introduction	1
2 Theory	5
2.1 Resistive random access memory	5
2.2 Tantalum oxide as resistive layer	8
2.3 Electronic structure calculations and DFT	12
2.4 Density functional tight-binding	19
2.5 Computational Methods	22
3 Amorphous tantalum oxide	24
3.1 Introduction	24
3.2 Convex Hull of the a-Ta ₂ O ₅ -TaO ₂ system	25
3.3 Simulated XPS spectra	26
3.4 Bader charge analysis	28
3.5 Bader charge/XPS peak fitting	30
3.6 Simulated XPS depth profile	31
4 Crystalline tantalum oxide	33
4.1 Introduction	33
4.2 Convex hull of v _O -defective λ-Ta ₂ O ₅	34
4.3 Primitive cell of the Ta ₄ O ₉ phase	36
4.4 Energetics of defect aggregation	38
4.5 Convex hull of crystalline phases	39
5 DFTB-parametrisation of Ta₂O₅	42
5.1 Introduction	42
5.2 Parametrisation	43
5.3 Benchmarking	45

6	Summary and outlook	48
6.1	Amorphous TaO _x	48
6.2	Crystalline TaO _x	49
6.3	Parametrisation of TaO _x for DFTB	49
6.4	Outlook	50

Appendix

A	Evaluation of DFT+U	63
B	Comparison of single-v_O charge densities	64
C	Density of amorphous TaO_x	65
Publications		66
	Publication 1	66
	Publication 2	75

List of Figures

2.1	Model IV curves of unipolar and bipolar resistive switching.	6
2.2	Comparison of v_O diffusion barriers and formation energies for amorphous HfO_x and TaO_x	10
2.3	Primitive cell of λ -phase Ta_2O_5	12
2.4	Flowchart describing the self-consistent cycle in DFT calculations.	15
3.1	Convex hull of the amorphous Ta_2O_5 - TaO_2 system; CDF for sixth-nearest neighbours; Percent-wise distribution of Ta coordination numbers.	25
3.2	Simulated XPS spectra of a- Ta_2O_5 and a- TaO_2	28
3.3	Core level energy plotted versus Bader charge for a- Ta_2O_5 , a- Ta_6O_{13} , and a- TaO_2 ; total energy of strained λ - Ta_2O_5	29
3.4	Fitting of Gaussians to XPS and Bader charge spectra; Comparison between Gaussian peak locations of XPS and Bader charge.	30
3.5	Stoichiometry-controlled comparison between experimental XPS depth profile and simulated XPS spectra.	32
4.1	Convex hull of the v_O -defective crystalline Ta_2O_5 - TaO_2 system.	34
4.2	Oxygen vacancy arrangement in Ta_4O_9 ground state; Structural rearrangement upon relaxation.	35
4.3	Primitive cell of the Ta_4O_9 phase.	36
4.4	Band structure and DOS spectrum of the Ta_4O_9 phase.	38
4.5	Real-space wave functions of pair-defect for the primitive Ta_4O_9 cell.	38
4.6	Oxygen vacancy formation energy per vacancy versus distance between individual vacancies.	39
4.7	Convex hull of hypothetical crystalline Ta_xO_y structures.	40
5.1	Evolution of repulsive spline fitting.	44
5.2	NVE MD-run of Ta_2O_5 cell.	44
5.3	Benchmarking of DFTB-calculated lattice parameters and v_O formation energies versus results obtained using DFT.	45
5.4	Comparison of a- Ta_2O_5 RDF and CDF spectra using DFT and DFTB.	46
A.1	PBE+U-calculated v_O formation energies for $U=0$ eV to 5 eV.	63
B.1	Charge densities for singular v_O	64
C.1	Boxplot of mass densities of amorphous tantalum oxide systems.	65

Chapter 1

Introduction

David Friedman once wrote: “If the median income rises to \$100,000 a year, we shall have no difficulty spending it.” Likewise, if the average smart phone storage capacity rises to 100 TB, we shall have no problem filling it up. Non-volatile memory goes wherever computers go, and computers have spread to virtually everywhere in the developed world.

Flash memory is one of the dominant types of non-volatile memory, with individual flash-containing chip sales numbering in the hundreds of billions. In design, a flash bit resembles a Metal Oxide Semiconductor (MOS) Field Effect Transistor (FET – MOSFET), with an extra so-called Floating Gate coupled capacitively to the control gate.¹ Due to electrons tunneling across the floating gate and being stored there, the dual-gate setup effectively acts as memory even when the device powers off, making the MOSFET suitable for non-volatile memory applications. However, Flash technology responds poorly to scaling, in particular because charge retention is not good enough to maintain reliable readouts below ~ 10 nm device sizes. This issue has caused researchers to search for alternatives in order to further increase memory density.

Several emerging memory technologies are poised to take over. So-called “Racetrack” memory relies on manipulating and reading individual magnetic domains in a vertical or horizontal nanowire.² Phase-change memory (PCM), originally from the late-60’s, relies on changing a chalcogenide glass between an amorphous and a crystalline state.³ Graphene has been proposed for a great many applications, memory being one of them.⁴ In 2002, researchers at Sharp Laboratories demonstrated “colossal magnetoresistive thin films”, thus conceiving the field of Magnetoresistive Random-Access Memory (MRAM).⁵ Finally, in Resistive Random Access Memory (ReRAM), the device region is switched between a high-resistance state (HRS) and a low-resistance state (LRS). Of the above, analysis experts regard MRAM as the likely successor to existing Dynamic RAM (DRAM) technology, while ReRAM is expected to take over for Flash.¹

ReRAM uses the resistive switching effect originally discovered for binary transition metal oxides (TMOs) by Hickmott in 1962,⁶ where a resistive material switches to a conducting state upon application of an electric field of sufficient strength. Although termed a “memory effect” as early as 1963,⁷ research interest waned around 1980, until it resurfaced at the turn of the millenium.^{8–10} Baek et al. suggests inadequate materials processing technology as responsible for the decades of lacking interest,¹¹ while Yang et al. cites the rise of Si integrated circuit technology.¹² Regardless of the reason, the first actual ReRAM cell

¹T. Coughling, R. F. Hoyt, and J. Handy, *IEEE report on digital storage and memory pt. 1*, IEEE, 2017

was presented at the 2004 IEEE International Electron Devices Meeting by a research team of the Samsung Corporation,¹¹ using TMO as switching layer.

Although early studies in ReRAM research had focused on perovskites,^{9,10} Baek et al. argued that TMOs were desirable due to being compatible with complementary MOS (CMOS) technology and resistant to thermal and chemical changes.¹¹ Even limited to TMOs, resistive switching has been demonstrated in many materials. Hickmott himself reported on SiO, Al₂O₃, Ta₂O₅, ZrO₂, and TiO₂ in his seminal paper,⁶ while Baek et al. reported having tried various TMOs, although they only named NiO explicitly. Also CuO_x,¹³ Nb₂O₅,¹⁴ Fe₃O₄,¹⁵ and CoO¹⁶ have been investigated, among others.

The 2008 IEEE International Electron Devices Meeting saw important contributions in the field of ReRAM research on Ta₂O₅¹⁷ and HfO₂,¹⁸ by the Panasonic Corporation and Industrial Technology Research Institute (ITRI), respectively. In particular, the demonstration of tantalum oxide ReRAM by Panasonic, and subsequent switch from TiO₂ to TaO_x by Hewlett-Packard in 2013,^{19,20} has contributed to increasing research efforts into this material.

Apart from being one of the materials originally investigated by Hickmott, Ta₂O₅ found its way to the semiconductor industry as a high- κ dielectric for use in e.g. MOSFETs. Its performance for ReRAM technology was well evaluated in comparison to TiO₂ in a 2014 review by Ho et al.²¹ In spite of the popularity of Ta₂O₅ as resistive-switching TMO, however, there is much that is still not known about it in the context of resistive switching. In particular, devices are frequently reported as non-stoichiometric, consisting of a thin (<5 nm) layer of Ta₂O_{5- δ} and a thicker region of TaO_{2- β} , where δ and β imply that the sample is not quite stoichiometric.^{17,22-29} The term TaO_x is commonly used to describe the resistive layer(s) in this type of cell, once again suggesting that the stoichiometry is unknown.

The non-stoichiometric nature of TaO_x devices implies they are amorphous, although this is rarely reported directly in literature. Yang et al. report predominantly amorphous films with nanocrystalline inclusions of Ta₂O₅.²³ Additionally, it is known that TaO_x films fabricated at room temperature are amorphous,²⁹⁻³¹ further implying that as-fabricated resistive switching layers are also amorphous. For this reason, in order to better understand the switching process on the atomic scale, it is necessary to investigate in detail the amorphous TaO_x (a-TaO_x) system.

However, a few studies suggest that crystalline TaO_x has a role to play as well. Recently, the presence of Ta₂O₅ crystallites was observed in a switched device,³² which adds to the observation by Yang et al. that crystalline Ta₂O₅ is present in as-fabricated devices.²³ Therefore, it is clearly necessary to investigate not only amorphous, but also crystalline, tantalum oxide.

This thesis presents a rigorous materials study of the tantalum oxide system using the theoretical framework of Density Functional Theory (DFT). The primary aim is to gain understanding of the switching process of TaO_x ReRAM devices by investigating both the amorphous and crystalline systems in various stages of oxygen deficiency. The thesis is organised as follows:

Chapter 2 provides an overview of the switching mechanism in ReRAM technology. Special attention is paid to relevant materials parameters. The relevance of Ta₂O₅ in relation to these parameters is discussed. Finally, the methodology of DFT is presented, followed by general computational details used in this study.

Chapter 3 presents a large-scale DFT study of amorphous tantalum oxide with varying oxygen content. Oxygen-deficient phases are compared in terms of DFT-calculated total energies. Simulated X-ray Photoelectron Spectroscopy (XPS) spectra are presented and compared to experiment, along with simulated oxidation states. The chapter concludes with the reproduction of an experimental XPS depth profile.

Chapter 4 presents a corresponding large-scale DFT study of crystalline tantalum oxide, accelerated by Cluster Expansion. Oxygen-deficiency is modeled in the form of increasing oxygen vacancy concentrations, leading to the discovery of a new theoretical metastable phase. This phase is found to have a unique defect structure, which is discussed in relation to ReRAM devices. Finally, a similar investigation modelling oxygen deficiency as phases with lower O content observed in Group V metals vanadium and niobium is performed.

Chapter 5 performs a parametrisation of tantalum oxide for the density functional tight-binding method, and evaluates the performance of said parametrisation both for crystalline and amorphous phases. Some problems related to fitting the repulsive potential are also discussed.

Chapter 6 summarises the main conclusions of Chapters 3 to 5, and provides an outlook for further study based on these conclusions as well as the literature review performed in Chapter 2.

Chapter 2

Theory

2.1 Resistive random access memory

The working principles of resistive switching are presented in this section. The aim is to provide the reader with a basic outline of key concepts, and describe desirable materials parameters for use in ReRAM devices. Ultimately, the benefits of TaO_x for purposes of resistive switching will be discussed.

2.1.1 Resistive switching to memristive switching

Although the focus of this thesis is on the performance of tantalum oxide, one topic has become so ingrained in ReRAM history as to be inseparable from it. In 1971, Chua theorised the existence of a fourth circuit element,³³ which he called the “memristor” – a contraction of the words “memory” and “resistor”. The memristor would at any instantaneous time t_0 behave like a resistor, except the “memristance” (analogous to resistance) would depend on the current integral from time $t = -\infty$ to t_0 . Thus, the instantaneous resistance would depend on the history of the device, which was therefore said to have memory. In 2008, Strukov et al. identified their resistive switching devices as performing like a memristor, “remembering” their history through their resistance state.¹⁹ Since then, the terms “resistive switching” and “memristive switching” have been used interchangeably, just as the term “memristor” is frequently used to describe resistive switching devices. For a full description of the memristor, see the seminal paper by Chua.

2.1.2 Unipolar versus bipolar switching

Depending on device geometry, the switching scheme may be either “unipolar” – where the switching is independent of voltage polarity – or “bipolar” – where one polarity switches ON (SET operation) and another switches OFF (RESET operation). Unipolar switching, depicted in Figure 2.1(a), occurs in a device which is symmetric with respect to electrode work functions; in the simplest case, a device using the same material for top electrode (TE) and bottom electrode (BE), respectively. In this scheme, a SET operation occurs at some voltage threshold V_{set} , while RESET occurs at a lower voltage threshold $V_{\text{reset}} < V_{\text{set}}$ at high current. A compliance current may be enforced by the control circuit. Examples of unipolar switching are found in Hickmott’s seminal paper,⁶ and the world premier device by Baek et al.¹¹

The contrast with bipolar switching is seen in Figure 2.1(b). Increasing the positive voltage results in a SET operation, while a subsequent negative voltage results in a RESET

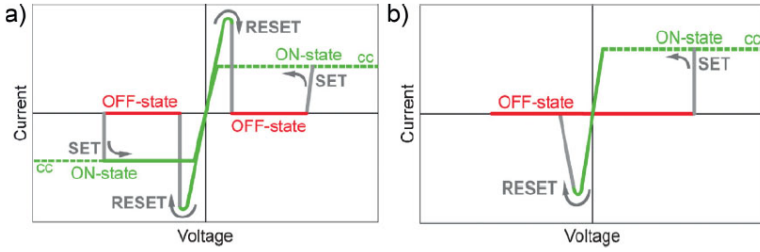


Figure 2.1: Model IV curves associated with unipolar (a) and bipolar (b) switching. Adapted from reference 34. ©2009 John Wiley & Sons, Inc. Reprinted with permission.

operation. This requires an asymmetric setup, which in the simplest case is achieved by using different electrode materials, but which may also be achieved in the device layer. In such a setup, it makes sense to refer to an Active Electrode (AE) in the region where the switching process occurs, and a Counter Electrode (CE) in the opposite region. The counter electrode must form an Ohmic contact with the device layer to avoid switching near the counter electrode. Examples of bipolar switching devices include the HfO_x prototype by Lee et al.,¹⁸ in which the device geometry was $\text{TiN}/\text{Ti}/\text{HfO}_x/\text{TiN}$, and the TaO_x prototype by Wei et al.,¹⁷ with geometry $\text{Pt}/\text{Ta}_2\text{O}_{5-\delta}/\text{TaO}_{2-\beta}/\text{Pt}$. The treatment of this section is based on Waser et al.’s 2009 review article.³⁴

2.1.3 Switching mechanism of ReRAM

There exist two fundamentally different ways in which to achieve conduction across an otherwise non-conducting ionic solid; namely i) to inject cations into the material (called the “electrochemical metallisation mechanism” – ECM³⁴), or ii) to remove anions from the material (called the “valence change mechanism” – VCM³⁴). The former is most notably achieved using Ag^+ cations. This method has been applied e.g. in Si/a-Si core-shell nanowires by Dong et al.,³⁵ which is the device used by Crossbar Inc.ⁱ The latter is the focus of this dissertation, and will be elaborated upon in the following.

On the nanoscale, applying an electric potential across an insulating ionic solid provides a driving force for drift of charged particles in the ionic solid. In particular, O ions will tend to migrate towards the cathode, which is equivalent to saying that oxygen vacancies (v_{O}) will form and migrate towards the anode. In an asymmetric bipolar device, the electric field gradient will be steeper at the Schottky contact (compared to the Ohmic contact). This steep gradient results in increased local Joule heating, which accelerates the v_{O} migration in the heated region (called the “thermochemical mechanism” – TCM³⁴). As the v_{O} migrate towards the anode, the metal oxide becomes increasingly metallised at the metal-insulator interface. This, in turn, shifts the Schottky contact further into the device layer, where the now metallized region meets a more intact region of the device layer. As this process continues, it results in the growth of conducting nanofilaments across the active layer, each of which is a highly v_{O} -deficient “version” of the original ionic solid. The device has then been turned ON. To turn it OFF within the bipolar switching scheme, the voltage polarity is reversed, which drives O ions back into the Schottky barrier region, restoring it to its initial insulating state.

Nanofilamentary resistance switching has been observed for NiO ,³⁶ TiO_2 ,³⁷ TaO_x ,³⁸ and HfO_2 .³⁹ The phenomenon of local Joule heating has been reported for TiO_2 ,^{40–42} NiO ,⁴³

ⁱSee webpage for Crossbar Inc.: <https://www.crossbar-inc.com/>

and Sr-based perovskites.⁴⁴ The significance of the Schottky barrier will be discussed in the following outline of key materials parameters.

2.1.4 Key materials parameters

Vacancy formation energy

The previous section established that a large part of resistive switching materials operate by creation and subsequent migration of v_O under an applied electric field. Within DFT, the formation energy, E_F , of charge-neutral defects in a metal oxide (M_xO_y) may be determined from the DFT-calculated total energies E as:

$$E_F = \left(E [M_xO_{y-1}] + \frac{1}{2}E [O_2] \right) - E [M_xO_y] \quad (2.1)$$

The v_O formation energy of a material is partly predicted by its formation enthalpy, H_F , in the sense that a higher (more negative) H_F will result in greater (more positive) vacancy formation energies. However, the precise v_O formation energy will depend on the energy level of the induced defect states, which requires dedicated research effort to determine.

Vacancy diffusion barrier

Apart from supplying the driving force needed to overcome the energy barrier in Equation (2.1), the applied electric potential must also provide an adequate driving force for v_O migration. In order for a v_O to diffuse towards the anode, it must overcome a series of local potentials referred to as diffusion barriers, which arise due to the surrounding lattice. Vacancy diffusion follows the Arrhenius equation:

$$D = D_0 e^{-E_A/k_B T} \quad (2.2)$$

where D_0 is a pre-exponential factor, E_A is the material-specific diffusion (or “activation”) barrier, and k_B is Boltzmann’s constant. The Arrhenius equation shows how local Joule heating contributes to the switching process by mediating diffusion through the temperature factor, and how some materials may exhibit greater diffusion than others through comparatively lower diffusion barriers.

Equation (2.2) implies that higher switching speed is achieved for lower diffusion barriers. However, too low diffusion barriers will result in decreased retention times. The reason is partly contained in Fick’s first law, stated here for oxygen vacancies:

$$J_{v_O} = -D \nabla C_{v_O} = -D_0 e^{-E_A/k_B T} \nabla C_{v_O} \quad (2.3)$$

J_{v_O} and C_{v_O} are the v_O diffusion flux and concentration, respectively. The implication for ReRAM devices is that the existence of a v_O -rich region, such as a nanofilament, provides a driving force for a net diffusion flux of v_O towards O-rich regions, even in the absence of an external potential. Hence, retention times are reduced for materials with low v_O -diffusion barriers in comparison with materials with higher diffusion barriers. Clima et al. therefore argue for an optimal range of diffusion barriers, namely between 1.0 eV to 2.0 eV.⁴⁵ The diffusion barrier of a v_O should be viewed in conjunction with its formation energy; i.e. it must be the lowest-energy vacancies that exhibit optimal diffusion barriers, since these are the vacancies most likely to form.

Factors governing the Schottky barrier

The Schottky barrier formed at the interface between the metal electrode and the resistive layer is important for device function. The specifics of the Schottky barrier depend both on the electrode material and the resistive material; hence a full treatment is beyond the

scope of this dissertation. However, key concepts are discussed here in order to present the important parameters for the resistive layer.

The Schottky barrier represents the height of the potential experienced by electrons traveling from the electrode into the resistive layer. The idealised Schottky barrier, ϕ_{B0} , is simply the difference between the electrode work function, ϕ_m , and the resistive layer electron affinity, χ :

$$\phi_{B0} = (\phi_m - \chi) \quad (2.4)$$

There are several effects that may alter the barrier height from the ideal case to the effective Schottky barrier, ϕ_{Bn} . One such effect, the Schottky effect, arises from the fact that electrons in the resistive layer induce image charges in the metal, creating an electric field, E . This lowers the barrier by:

$$\delta\phi = \sqrt{\frac{eE}{4\pi\kappa}}, \quad (2.5)$$

in which κ describes the dielectric constant of the resistive layer. Hence, a higher dielectric constant will indirectly result in a higher Schottky barrier, by reducing the Schottky effect. The effect of the Schottky barrier on metal-to-semiconductor current density J is given by Richardson's law of thermionic emission:

$$J(V, T) = \left[A^* T^2 \exp\left(\frac{-e\phi_{Bn}}{k_B T}\right) \right] \left[\exp\left(\frac{eV}{k_B T}\right) - 1 \right] \quad (2.6)$$

where A^* is Richardson's constant. A low Schottky barrier can thus result in relatively high zero-voltage thermionic emission, which reduces the I_{ON}/I_{OFF} ratio. Chand et al. provided an overview of work functions and electron affinities in their proposed Ti/Al₂O₃/HfO_x/TiN device, in which Al₂O₃ acts as a tunnelling barrier layer to reduce leakage currents.⁴⁶ The electron affinities of Al₂O₃ and HfO_x are 1.35 and 2.65, respectively. The importance of the Schottky barrier was highlighted by Hur et al., who created a theoretical model which accurately captured bipolar switching behaviour.²²

2.2 Tantalum oxide as resistive layer

The previous dissection of ReRAM highlighted the role of oxygen vacancies in the ON/OFF switching of the resistive layer. This section will discuss tantalum oxide as material for ReRAM devices, and explain its popularity as resistive material. Although several different stoichiometries of tantalum oxide have been reported,^{47–49} the main body of work has focused on tantalum pentoxide, Ta₂O₅. Crystalline Ta₂O₅ has been extensively studied since the 1930's, with many structural models being proposed. In spite of this, it does not seem like a scientific consensus as to the precise atomic structure has been reached.

Generally, tantalum oxide films fabricated under most conditions are amorphous. This has been observed using thermal oxidation (300–700 °C),⁵⁰ Chemical Vapour Deposition (CVD; temperature not reported),⁵¹ Radio Frequency (RF) sputtering (substrate temperature of 576 °C),⁵² ion beam sputtering (temperature not reported),³⁰ and Pulsed Laser Deposition (PLD; room temperature).³¹ Crystalline films have been obtained using CVD (900 °C),⁵³ and RF sputtering (substrate temperature of 946 °C).⁵² An amorphous-to-crystalline transition has been observed by annealing at 1100 °C for 8 h,⁵⁴ 600 °C for 14 h,⁵⁵ 900 °C for 30 min,⁵⁵ and partly by annealing at 700 °C for 10 h (“partly” here means that the Raman

spectrum contains signatures from, but is not equal to, crystalline reference spectra).³⁰ Both amorphous and crystalline tantalum oxide are investigated in this dissertation, and will be described separately in the following.

2.2.1 Amorphous tantalum oxide

The amorphous Ta₂O₅ system exhibits good performance on most of the parameters described above. Tantalum oxide entered the electronics industry as a proposed high- κ dielectric; Indeed, Murawala et al. obtained values of $\kappa = 25 - 38$ for MOS devices consisting of Au/Ta₂O₅/n⁺Si,⁵¹ where n⁺ denotes significant n-doping. The authors note (without explicit citation) that previous studies yielded $\kappa = 15 - 25$ which by Murawala et al. is attributed to the presence of SiO₂ in the cited studies' devices, which may result in the measured κ being the average of SiO₂ and Ta₂O₅. This claim could not be verified for this dissertation, however, the table value of κ for SiO₂ is 3.9 (see e.g. Neamen,⁵⁶ Appendix B), by which standard Ta₂O₅ definitely qualifies as a high- κ dielectric.

Several studies have reported on the band gap of amorphous Ta₂O₅, yielding values of 4.1 eV (thermal oxidation of Ta and e-beam evaporation of Ta₂O₅),⁵⁰ 4.4 eV (anodized Ta),⁵⁷ and 5.28 eV (amorphous CVD).⁵¹ In 2000, Fleming et al. noted that the cited studies used different definitions of the band gap.⁵⁸ To correct this, they fitted their measured absorption spectra to the power-law absorption edge:⁵⁹

$$\alpha = \text{const} \cdot \frac{(E - E_G)^n}{E^2} \quad (2.7)$$

where α is the measured absorption coefficient, E (here) denotes the energy of the absorbed photon, and E_G is the band gap. The authors find the best fit for $n = 2.2$ and $E_G = 4.0$ eV, and use the same method to correct the aforementioned band gaps to 4.1 eV (thermal oxidation/e-beam evaporation; no change), 3.8 eV (anodized Ta), and 4.3 eV (amorphous CVD), for an average of $E_G = (4.05 \pm 0.18)$ eV. A critical review of the various methods of determining the band gap is beyond the scope of this report. The work of Fleming et al. seems to have resulted in a scientific consensus of ~ 4.0 eV for the band gap of a-Ta₂O₅. This value is supported by DFT calculations, for instance in the works of Lee et al. (Supplemental Material),⁶⁰ and Guo and Robertson.⁶¹

The work of Clima et al. included an unprecedented, to the knowledge of this author, DFT study of all v_O-formation energies *and* first-neighbour diffusion barriers for their models of a-TaO_x and a-HfO_x.⁴⁵ The results are reprinted in Figure 2.2. Although the authors did not report on computational details, it is here assumed that they were similar for both materials, and that the comparison is valid. The study showed that Ta₂O₅ contained comparatively lower diffusion barriers, as seen from the Cumulative Distribution Function (CDF) in Figure 2.2(a). Further, a larger amount of v_O was found within the optimal area of E_F (<1.0 eV) and E_A (1.0 eV to 2.0 eV) than HfO₂; see Figure 2.2(b-c). Finally, the study pointed to a larger amount of barrier-less v_O jumps (5%) as contributing to a pre-selection of stable defects. The study pointed to the comparatively better retention in Ta₂O₅ as originating from the differences in E_F and E_A . Such a study requires a phenomenal computational effort, however, and this author knows of no such data on other metal oxide phases to which one could compare the cited results. However, HfO_x is considered a top-of-the-line material for ReRAM devices, as evidenced by its endorsement by ITRI (see Chapter 1). Hence, a direct comparison that shows TaO_x performing even better is strong support for using TaO_x.

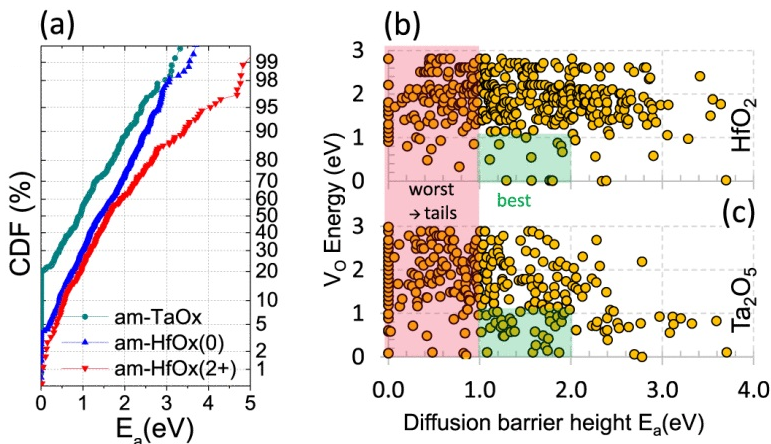


Figure 2.2: (a): CDF of v_O diffusion barriers for amorphous HfO₂ and Ta₂O₅. (b-c): v_O formation energy versus diffusion barrier for HfO₂ (b) and Ta₂O₅ (c). Shaded areas show disadvantageous (red) and advantageous (green) regions. Figure reprinted from reference 45. ©2015 IEEE.

Amorphous tantalum oxide presents formidable advantages for ReRAM technology. An immediate benefit of using an amorphous resistive layer is that material isotropy is guaranteed, which simplifies manufacturing processes. In addition, TaO_x devices are reported to consist of a thin layer of Ta₂O_{5- δ} formed over a bulk region of TaO_{2- β} .^{17,25,29,38} In fact, a similar effect was observed as early as 1993 by Murawala et al.,⁵¹ who remarked that the surface of their TaO_x film was O-rich due to surface oxidation. (The sample of Murawala et al. had significantly higher O content, however.) This allows the oxygen-deficient TaO_{2- β} region to function as an oxygen “sink”, where migrating O ions may be captured and stored until mobilized by a reset operation (see e.g. reference 21 for more information about this argument). In contrast, Kwon et al. found that migrating O ions from a uniform rutile-TiO₂ layer form a pocket of O₂ at the cathode.³⁷ For large enough device cross sections, the gas buildup was enough to blow part of the electrode off.

The high dielectric constant, relatively wide band gap, and comparatively high amount of low-energy v_O with mid-sized diffusion barriers contribute to making amorphous TaO_x one of the dominant materials for valence-change ReRAM devices. Its marketability is further compounded by its status as a CMOS-compatible binary metal oxide, the amorphous nature of as-fabricated films, and asymmetric Ta/O ratio. Tantalum has one possible drawback, however, in scarcity. According to the U.S. Geological Survey,ⁱⁱ Ta makes up ~ 2 atoms per 10^6 Si atoms in the upper crust of the earth, comparable to rare-earth elements like Dysprosium and Erbium. Hf fares little better at ~ 5 atoms per 10^6 Si. In fact, any internet search for “Tantalum” will yield results of Ta jewellery due in part to its scarcity. Nevertheless, no concerns as to whether Ta is abundant enough to replace Si-based Flash memory have been raised to the knowledge of this author.

As alluded to in the opening paragraph of this section, as well as in Chapter 1, crystalline Ta₂O₅ coexists along amorphous TaO_x in resistive layers.^{23,32} Hence, a treatment of this

ⁱⁱCarried out by Gordon B. Haxel, James B. Hedrick, and Greta J. Orris; available at URL: <https://pubs.usgs.gov/fs/2002/fs087-02/>

material is presented in the following, beginning with a review of the literature on its crystal structure.

2.2.2 Crystalline tantalum pentoxide

The most common form of (low-temperature) tantalum pentoxide is orthorhombic and labelled β . Apart from an early study in 1932,⁶² the majority of x-ray diffraction data on β -Ta₂O₅ was gathered in the post-war period of the 1950's and 1960's. The earliest study of this period was performed by Lagergren and Magnéli,⁶³ with the first x-ray study attributed to Schönberg.⁶⁴ Note that in the work of Schönberg, the orthorhombic form of Ta₂O₅ is referred to as ξ . The earliest reference to β -Ta₂O₅, to the knowledge of this author, was made by Holser in 1956.⁶⁵ Kofstad and Spyridelis et al. later adopted the term,^{66,67} with the latter citing Kofstad as the origin.

Despite considerable research efforts,^{49,54,62–65,67–74} the atomic structure of β -Ta₂O₅ was elusive throughout the entire 20th century. It was established by Calvert and Draper in 1962⁷³ and Lehovc in 1964⁵⁴ that β -Ta₂O₅ consists of planes of Ta₂O₃ joined by Ta–O chains in the out-of-plane direction. Unit cell parameters were determined as $a = (6.20 \pm 0.02) \text{ \AA}$, $b = n \cdot 3.66 \text{ \AA}$ (n signifies that some studies found an integer multiple of the cited lattice parameter), and $c = (3.89 \pm 0.01) \text{ \AA}$.^{49,54,73–76} These parameters are averaged across multiple references. Several structural models were proposed,^{54,65,67,73,74} but it was not until 2002 that the matter was settled, at least for some years.⁷⁵

Development of the β model

Aleshina and Loginova considered four structural models theorized by Spyridelis et al. (based on UO₃ – Model 1),⁶⁷ Calvert and Draper (based on U₂O₅ – Model 2),⁷³ Holser (based on U₃O₈ – Model 3),⁶⁵ and a modified version of the proposed structure of Lehovc (Model 4).⁵⁴ Of these, Aleshina and Loginova remark that Models 1–3 were originally proposed based on similarities between X-ray diffraction patterns, whereas only Lehovc attempted to determine the atomic coordinates (which were criticized and suitably modified in Aleshina and Loginova's study). Connections between Ta₂O₅ and uranium oxides can be traced to Elson et al.,⁷⁷ and Holser.⁶⁵

Of the proposed models, Aleshina and Loginova found low reliability factors (signifying a close match) for models 1 and 4. However, the theoretical pattern for model 1 failed to reproduce some weak reflections from the experimental diffraction, and hence the authors proposed model 4 as the true atomic structure of β -Ta₂O₅, with cell parameters $a = 6.217 \text{ \AA}$, $b = 3.677 \text{ \AA}$, and $c = 7.794 \text{ \AA}$.

Criticism of the β model and development of the λ model

In 2010, Andreoni and Pignedoli examined the β and the similar, but hexagonal δ (not covered here) phases.⁷⁸ Using DFT calculations, the authors found imaginary phonon modes signifying intrinsic instability for both structures. Recognizing a need for further study, Lee et al. evaluated existing structural models using DFT and proposed their own, novel λ model – depicted in Figure 2.3.⁶⁰ While the β and δ models were found to be unstable with total DFT energies 1.27 eV/fu (“fu” – formula unit) and 0.91 eV/fu, respectively, as compared to an amorphous Ta₂O₅ model, the 11 fu model of Stephenson and Roth⁷⁴ and the λ models were found to be stable with -0.75 eV/fu and -0.81 eV/fu , respectively. In addition, the authors used hybrid functional calculations to determine E_G for the scrutinized phases, and found $\sim 2 \text{ eV}$ for β and δ , while they obtained $\sim 4 \text{ eV}$ for the amorphous and λ models. The obtained lattice parameters for the β phase were $a = 6.52 \text{ \AA}$, $b = 3.69 \text{ \AA}$, and $c = 3.89 \text{ \AA}$ while the λ phase yielded $a = 6.25 \text{ \AA}$, $b = 3.70 \text{ \AA}$, and $c = 3.83 \text{ \AA}$. This strongly suggests that the λ phase is the correct structural model for crystalline Ta₂O₅, or at least the correct

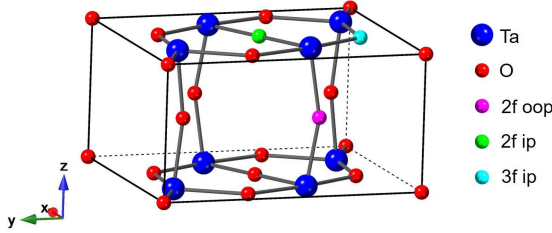


Figure 2.3: Primitive cell of the λ phase of Ta_2O_5 developed by Lee et al.⁶⁰ Note the characteristic Ta_2O_3 structure in the XY plane connected by Ta–O chains along the Z axis. Magenta, green, and cyan atoms show twofold out-of-plane, twofold in-plane, and threefold in-plane vacancies, respectively.

model to incorporate in DFT calculations in order to accurately model real samples. To the knowledge of this author, no Rietveld refinement study has been attempted on the λ phase.

Properties of orthorhombic Ta_2O_5

In addition to the review on materials properties of α - Ta_2O_5 , a corresponding review is performed here for crystalline (orthorhombic) Ta_2O_5 . Pavlovic determined dielectric constants of ~ 24.0 at 300 K and ~ 25.5 at 400 K for ceramic β - Ta_2O_5 .⁷⁹ Knausenberger and Tauber determined the dielectric constant of pyrolytic β - Ta_2O_5 films as ~ 42.0 – 44.0 at ~ 280 K.⁵³ Knausenberger and Tauber further commented that lack of experiments on the dielectric constant of β - Ta_2O_5 meant there was little basis for comparison, except to the work of Pavlovic. Despite the disagreement in values, orthorhombic Ta_2O_5 may be considered a high- κ dielectric along with amorphous Ta_2O_5 .

The band gap of orthorhombic Ta_2O_5 has been determined as 4.2 eV by Knausenberger and Tauber.⁵³ As with the amorphous band gaps, this was corrected by Fleming et al., who obtained a value of 4.0 eV.⁵⁸ As such, there is good agreement between the values of E_G for crystalline and amorphous Ta_2O_5 . Lee et al. calculated a value of ~ 3.8 eV for their λ model (see DOS spectra in the supplemental information for reference 60). The value represents this author’s interpretation.

The structure of λ - Ta_2O_5 depicted in Figure 2.3 has three symmetrically inequivalent O atoms, and hence, three different v_O sites. These are twofold coordinated in-plane (2f ip), threefold coordinated in-plane (3f ip), and twofold coordinated out-of-plane (2f oop). The v_O formation energies and diffusion barriers of λ - Ta_2O_5 were studied by Jiang and Stewart.⁸⁰ The formation energies obtained for neutral v_O were 5.33 eV to 5.74 eV for the 2f ip vacancy (depending on atomic rearrangement), 4.99 eV for the 3f ip vacancy, and 5.51 eV for the 2f oop vacancy. Diffusion barriers for these defects were strongly anisotropic, ranging from ~ 0.55 eV to 0.70 eV for in-plane diffusion to ~ 1.70 eV to 2.20 eV for diffusion from an in-plane site to an out-of-plane site. Finally, the theoretical density of orthorhombic Ta_2O_5 is $8.73 \times 10^3 \text{ kg/m}^3$,⁸¹ while Reisman et al. reported a value of $8.18 \times 10^3 \text{ kg/m}^3$ for the β phase.⁸²

2.3 Electronic structure calculations and DFT

This section presents the framework of DFT, and highlights the key parameters which must be considered when performing studies using DFT. The focus will be on aspects relevant to this dissertation; hence the treatment is far from complete.

2.3.1 The Schrödinger equation

At the heart of electronic structure calculations, and of quantum mechanics as a whole, lies the Schrödinger equation. The Schrödinger equation is a wave equation, and as such describes propagation in space *and* time. But although time-dependent DFT does exist, this dissertation will exclusively use time-independent DFT, and hence the time-independent form of the Schrödinger equation. In this picture, the Schrödinger equation describes the energy levels E_i of a system with eigenfunctions ψ_i and Hamiltonian operator \hat{H} :

$$\hat{H}\psi_i(\mathbf{r}) = \left[\frac{-\hbar^2}{2m}\nabla^2 + V(\mathbf{r}) \right] \psi_i(\mathbf{r}) = E_i\psi_i(\mathbf{r}), \quad (2.8)$$

in which \hbar is the reduced Planck constant, m is the electron mass, and V is a potential associated with the system. From now on, the treatment will adopt atomic units, so that $\hbar = e = m = 1$. The time-independent Schrödinger equation contains information on all stationary eigenstates ψ of a system described by the Hamiltonian \hat{H} . In solid-state physics, the system usually consists of N electrons with position vectors $\mathbf{r} \in \{\mathbf{r}_i, i = 1, \dots, N\}$, and K atoms with positions vectors $\mathbf{R} \in \{\mathbf{R}_I, I = 1, \dots, K\}$, atomic mass M_I and charge Z_I :

$$\begin{aligned} \hat{H} = & - \overbrace{\sum_{I=1}^K \frac{\nabla_I^2}{2M_I}}^{\hat{T}_n} - \overbrace{\sum_{i=1}^N \frac{1}{2}\nabla_i^2}^{\hat{T}_e} + \overbrace{\frac{1}{2} \sum_{I=1}^K \sum_{J \neq I}^K \frac{Z_I Z_J}{|\mathbf{R}_I - \mathbf{R}_J|}}^{\hat{V}_{nn}} \\ & + \underbrace{\frac{1}{2} \sum_{i=1}^N \sum_{j \neq i}^N \frac{1}{|\mathbf{r}_i - \mathbf{r}_j|}}_{\hat{V}_{ee}} - \underbrace{\sum_{I=1}^K \sum_{i=1}^N \frac{Z_I}{|\mathbf{R}_I - \mathbf{r}_i|}}_{\hat{V}_{ne}} \end{aligned} \quad (2.9)$$

The labels attached to the braces denote kinetic energy ($\hat{T}_{e,n}$) of electrons (e) and nuclei (n), respectively, and electrostatic interactions ($\hat{V}_{ee,nn,ne}$) between pairs of electrons (ee), nuclei (nn), and electrons and nuclei (ne).

2.3.2 Adiabatic and Born-Oppenheimer approximations

The mass of a proton is roughly 1833 times greater than that of an electron and, by extension, the electrons move thousands of times faster than the nuclei. This allows for a significant simplification: The electrons respond instantaneously to any perturbation in the nuclear subsystem, and are thus considered as being in a stationary state. The many-body wave function Ψ of a system can then be divided into an electronic part, Φ , and a nuclear part, Θ :

$$\Psi(\mathbf{R}, \mathbf{r}, t) = \sum_j \Theta_j(\mathbf{R}, t) \Phi_j(\mathbf{R}, \mathbf{r}) \quad (2.10)$$

This is the ‘‘adiabatic approximation’’, referring to the fact that the electrons remain in their instantaneous eigenstate. In simplifying the many-body wave function, the possibility of nuclear dynamics inducing electronic transitions has been ignored.

Within the adiabatic approximation, the time-independent Schrödinger equation is first solved for the electronic wave functions. Afterwards, the time-dependent Schrödinger equation is solved for the nuclear wave functions, in which the electronic eigenenergies enter as a parameter:

$$\left(-\sum_{I=1}^P \frac{1}{2M_I} \nabla_I^2 + \tilde{\epsilon}_n(\mathbf{R}) \right) \Theta_m(\mathbf{R}, t) = E_m \Theta(\mathbf{R}) \quad (2.11)$$

The $\tilde{\epsilon}_n$ parameters contain both the as-calculated electronic eigenenergies ϵ_n and a correction term arising from the dependence of the electronic wave functions on the nuclear coordinates:

$$\tilde{\epsilon}_n(\mathbf{R}) = \epsilon_n(\mathbf{R}) + \sum_{I=1}^P \frac{1}{2} \langle \Phi_q | \nabla_I^2 | \Phi_q \rangle \quad (2.12)$$

Within the ‘‘Born-Oppenheimer approximation’’, the second term is neglected, effectively decoupling the electronic and nuclear solutions to the Schrödinger equations completely. Both the Born-Oppenheimer and the adiabatic approximations rely on a small ratio of m/M as validity criterium, although the adiabatic approximation requires the additional condition that nuclear and electronic eigenenergies not be too close. Both these criteria are assumed to be satisfied; Indeed, for the Born-Oppenheimer approximation, Kohanoff gives the error as smaller than 0.5%.⁸³

2.3.3 Density Functional Theory

The modern powerhouse of computational physics, DFT, offers a desirable tradeoff between speed and accuracy. The method builds on the pioneering work of Hohenberg and Kohn,⁸⁴ who considered the electronic density ρ associated with N electrons under the influence of an external potential, $V_{\text{ext}}(\mathbf{r})$. Their work then derived the two so-called Hohenberg-Kohn theorems, stated here in their original phrasing with the notation of this treatment:

HK 1: The external potential $V_{\text{ext}}(\mathbf{r})$ is (to within a constant) a unique functional of $\rho(\mathbf{r})$; since, in turn, $V_{\text{ext}}(\mathbf{r})$ fixes H , [...] the full many-particle ground state is a unique functional of $\rho(\mathbf{r})$.

HK 2: The energy functional $E[\rho(\mathbf{r})]$ assumes its minimum value for the correct $\rho(\mathbf{r})$, if the admissible functions are restricted by the condition:

$$N[\rho] \equiv \int \rho(\mathbf{r}) d\mathbf{r} = N$$

A corollary of HK 1 is that, since V_{ext} is determined by ρ , so is the ground state many-body wave function Ψ . The following year, Kohn and Sham proposed that the density produced by interacting electrons be approximated by a non-interacting electron gas,⁸⁵ providing a crucial simplification. In this picture, many-body interactions are gathered in the so-called ‘‘exchange and correlation’’ (XC) term. Kohn and Sham’s proposed potential V_{KS} and energy functional E_{KS} then take the form:

$$V_{\text{KS}}[\rho] = \frac{1}{2} \int \frac{\rho(\mathbf{r}')}{|\mathbf{r} - \mathbf{r}'|} d\mathbf{r}' + V_{\text{ext}}(\mathbf{r}) + V_{\text{XC}}[\rho] \quad (2.13)$$

$$E_{\text{KS}}[\rho] = T_{\text{R}}[\rho] + \frac{1}{2} \int \int \frac{\rho(\mathbf{r})\rho(\mathbf{r}')}{|\mathbf{r} - \mathbf{r}'|} d\mathbf{r}d\mathbf{r}' + \int \rho(\mathbf{r}) V_{\text{ext}}(\mathbf{r}) d\mathbf{r} + E_{\text{XC}}[\rho], \quad (2.14)$$

where XC interactions are collected in the functionals V_{XC} and E_{XC} , and T_{R} is the kinetic energy. The first and second terms in V_{KS} are the Hartree potential, V_{H} , and the external

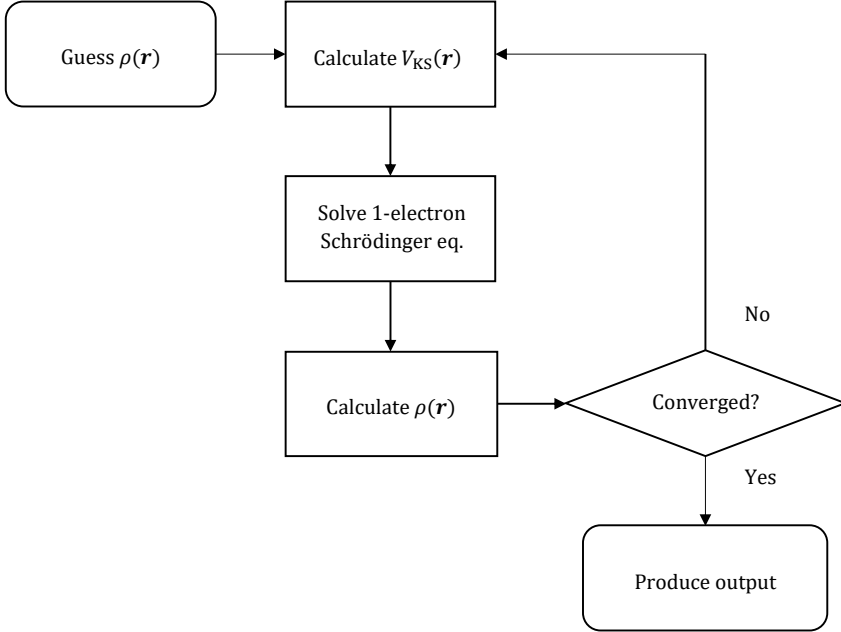


Figure 2.4: Flowchart describing the self-consistent cycle in DFT calculations.

potential arising from the surrounding nuclei, respectively. The one-electron Schrödinger equation then becomes:

$$\hat{H}_{\text{KS}}\phi_i(\mathbf{r}) = \left[-\frac{1}{2}\nabla^2 + V_{\text{KS}}(\mathbf{r}) \right] \phi_i(\mathbf{r}) = \epsilon_i\phi_i(\mathbf{r}), \quad (2.15)$$

where ϕ_i denotes a one-electron wave function, and ϵ_i is a Lagrangian multiplier whose physical meaning is debatable. Finally, the density ρ may be straightforwardly calculated:

$$\rho(\mathbf{r}) = \sum_i |\phi_i(\mathbf{r})|^2 \quad (2.16)$$

Equations (2.13), (2.15) and (2.16) are commonly called the Kohn-Sham equations. These must be solved self-consistently, since the density is used to compute the solutions ϕ_i to the Schrödinger equation, which in turn are used to compute the density. Figure 2.4 provides a flowchart of the self-consistent cycle in DFT.

So far, no approximations have been made in Eqs. (2.13) and (2.15) due to the inclusion of the many-body XC effects as the functional V_{XC} . This functional will be discussed in the following.

2.3.4 Exchange and Correlation

Providing a reasonable approximation of V_{XC} is the key issue for DFT. “Exchange” interactions arise due to the requirement that the overall wave function be antisymmetric upon exchange of two electrons. “Correlation” refers to the change in probability of finding an electron at position \mathbf{r} due to the presence of another electron at position \mathbf{r}' . In other words, Coulomb repulsion gives rise to a correlation between each individual electron and

every other electron in the system. The exchange part is known exactly within Hartree-Fock (HF) theory:

$$E_X^{\text{HF}} = -\frac{1}{2} \sum_{i,j} \int \int \frac{\phi_i^*(\mathbf{r})\phi_j^*(\mathbf{r}')\phi_i(\mathbf{r}')\phi_j(\mathbf{r})}{|\mathbf{r} - \mathbf{r}'|} d\mathbf{r}d\mathbf{r}' \quad (2.17)$$

Note that the above expression allows for an exchange self-interaction in the case where $i = j$. This is purposefully kept, in order that it may cancel out with the same term in the Coulomb repulsion integral.

While it is possible to calculate the exchange integral exactly, it is not always desirable. First, it implies splitting E_{XC} into E_X and E_C , when usually the sum $E_{\text{XC}} = E_X + E_C$ is the meaningful quantity. Second, the integral is too computationally expensive to be feasible in larger studies. Rather than looking for exact solutions, which will necessarily scale unfavourably with the number of one-electron wave functions, DFT searches for a reasonable approximation of the XC functional.

In their seminal paper, Kohn and Sham proposed that an inhomogeneous electronic system be considered locally homogeneous.⁸⁵ The exchange-correlation energy can then be determined from the homogeneous electron gas, for which the theoretical groundwork is much more accurate. This is referred to as the ‘‘Local Density Approximation’’ (LDA):

$$E_{\text{XC}}^{\text{LDA}}[\rho] = \int \rho(\mathbf{r}) \epsilon_{\text{XC}}[\rho(\mathbf{r})] d\mathbf{r}, \quad (2.18)$$

in which ϵ_{XC} denotes an energy *density* with the expression:

$$\epsilon_{\text{XC}}[\rho] = \frac{1}{2} \int \frac{\rho_{\text{XC}}(\mathbf{r}, \mathbf{r}')}{|\mathbf{r} - \mathbf{r}'|} \quad (2.19)$$

Although the performance is quite good for systems with strong bonding (i.e. covalent, ionic, and metallic bonding), the most commonly used XC-functional in solid state physics is the ‘‘Generalized Gradient Approximation’’ (GGA) proposed by Perdew, Burke, and Ernzerhof (PBE).⁸⁶ Since LDA necessarily produces electron densities that are more homogeneous than exact densities, a natural way to improve upon it is to include the density gradient in the approximation:

$$E_{\text{XC}}^{\text{GGA}}[\rho] = \int \epsilon_{\text{XC}}[\rho(\mathbf{r}), \nabla\rho(\mathbf{r})] \rho(\mathbf{r}) d\mathbf{r} \quad (2.20)$$

A known limitation of both LDA and GGA are their tendencies to greatly underestimate band gaps of semiconductors and insulators. This stems partly from the fact that, when moving away from exact exchange, the self-interaction no longer cancels out completely. This drives occupied states up in energy, reducing the energy gap to unoccupied states. Another important aspect is the lack of the so-called ‘‘derivative discontinuity’’, Δ , which will not be covered here. (The GLLB-sc method exists to calculate and correct for the derivative discontinuity; see Kuisma et al.)⁸⁷

The self-interaction error may be corrected by ‘‘hybrid’’ functionals, so called because they include a fraction of exact exchange in addition to the approximated XC functional:

$$E_{\text{XC}}^{\text{hyb}} = \alpha E_X^{\text{HF}} + (1 - \alpha) E_X^{\text{DFT}} + E_C^{\text{DFT}} \quad (2.21)$$

in which α is the fraction of HF exchange. In an attempt to reduce the computational effort required to calculate the HF exchange integral, Heyd, Scuseria, and Ernzerhof (HSE) proposed a method widely used today.⁸⁸ The HSE method splits the Coulomb operator $1/r$ into short-range and long-range components, and applies the Gaussian error function, erf, to screen the long-range term:

$$\frac{1}{r} = \frac{\overbrace{\text{erfc}(\omega r)}^{\text{short-range}}}{r} + \frac{\overbrace{\text{erf}(\omega r)}^{\text{long-range}}}{r} \quad (2.22)$$

In which ω is an adjustable parameter and $\text{erfc} = 1 - \text{erf}$. For $\omega = 0$, the long-range term becomes zero. The introduction of the parameters α and ω may in principle be fitted on a case-by-case basis. However, a common choice is $\alpha = 0.25$ and $\omega = 0.20$, which is referred to as HSE06. Although HSE promises increased efficiency, the CPU time consumption still increases drastically as compared to “pure” DFT; e.g. PBE.

2.3.5 Representation of electronic wave functions

Two of the most important methods of describing the one-electron wave functions are in a basis of atomic orbitals (AO), and in a basis of plane waves (PW). This dissertation exclusively uses the PW basis for DFT calculations, whose background will be stated here, followed by a brief discussion at the end. The periodic structure of crystalline solids ensures that the potential $v(\mathbf{r})$ experienced by electrons in the solid is periodic:

$$v(\mathbf{r}) = v(\mathbf{r} + \mathbf{a}_i) \quad (2.23)$$

where \mathbf{a}_i represents a lattice vector of the crystal. Bloch’s theorem then states that the wave function of any electron ϕ with wave vector \mathbf{k} in the system is given by a similarly periodic function u and a phase factor:⁸⁹

$$\phi_{\mathbf{k}}(\mathbf{r}) = e^{i\mathbf{k}\cdot\mathbf{r}} u_{\mathbf{k}}(\mathbf{r}) \quad (2.24)$$

Translating by a lattice vector \mathbf{a}_i yields:

$$\phi_{\mathbf{k}}(\mathbf{r} + \mathbf{a}_i) = e^{i\mathbf{k}\cdot\mathbf{a}_i} e^{i\mathbf{k}\cdot\mathbf{r}} u_{\mathbf{k}}(\mathbf{r}), \quad (2.25)$$

which utilises the fact that $u_{\mathbf{k}}(\mathbf{r} + \mathbf{a}_i) = u_{\mathbf{k}}(\mathbf{r})$. The phase factor $e^{i\mathbf{k}\cdot\mathbf{a}_i}$ drops out when calculating the probability density $|\langle\phi_{\mathbf{k}}(\mathbf{r})|\phi_{\mathbf{k}}(\mathbf{r})\rangle|^2$. The function $u_{\mathbf{k}}(\mathbf{r})$ in real-space can be written as a Fourier transform of the function $\tilde{u}_{\mathbf{k}}(\mathbf{g})$ for the reciprocal-space coordinate \mathbf{g} :

$$u_{\mathbf{k}}(\mathbf{r}) = \int e^{i\mathbf{g}\cdot\mathbf{r}} \tilde{u}_{\mathbf{k}}(\mathbf{g}) d\mathbf{g} \quad (2.26)$$

Now, since $u_{\mathbf{k}}(\mathbf{r})$ is periodic, the reciprocal-space coordinate \mathbf{g} must obey $e^{i\mathbf{g}\cdot\mathbf{a}_i} = 1 \Rightarrow \mathbf{g} \cdot \mathbf{a}_i = 2n\pi$ in order to satisfy the periodicity of the lattice. This requirement corresponds to \mathbf{g} being an integer multiple of the reciprocal lattice vectors \mathbf{G} , which discretises the Fourier transform to a Fourier series with coefficients $C_{\mathbf{k}}$:

$$\phi^{(\mathbf{k})}(\mathbf{r}) = \frac{e^{i\mathbf{k}\cdot\mathbf{r}}}{\sqrt{\Omega}} \sum_{\mathbf{G}=\mathbf{0}}^{\infty} C_{\mathbf{k}}(\mathbf{G}) e^{i\mathbf{G}\cdot\mathbf{r}}, \quad (2.27)$$

in which Ω is the volume of the cell. Finally, this results in the PW basis functions $\phi_{\mathbf{G}}(\mathbf{r})$ and eigenstates j given by:

$$\phi_{\mathbf{G}}(\mathbf{r}) = \frac{1}{\sqrt{\Omega}} e^{i\mathbf{G}\cdot\mathbf{r}}, \quad \phi_j^{(\mathbf{k})}(\mathbf{r}) = e^{i\mathbf{k}\cdot\mathbf{r}} \sum_{\mathbf{G}=0}^{\infty} C_{j\mathbf{k}}(\mathbf{G}) \phi_{\mathbf{G}}(\mathbf{r}) \quad (2.28)$$

Note that the eigenstate ϕ_j describes the entire system (i.e. all Brillouin zones in reciprocal space) through the sum over \mathbf{G} , while it describes the first Brillouin zone through the wave vector \mathbf{k} .

Cutoff energy

The Fourier series of the PW basis set is in principle infinite, and must be truncated for practical purposes. Fortunately, the coefficients $C_{\mathbf{k}}(\mathbf{G})$ decrease with increasing \mathbf{G} , so the truncation can be performed without considerable loss of functionality. The standard measure of truncation is the cutoff energy of the PW's:

$$\frac{1}{2} |\mathbf{k} + \mathbf{G}| < E_{\text{cut}} \quad (2.29)$$

Using this measure, the Fourier series is calculated for all $|\mathbf{k} + \mathbf{G}|$ which satisfy the above equation. Typical energy cutoffs range in the hundreds of electron volts.

Discussion of the PW basis

As the derivation of the PW basis set might suggest, it provides a powerful description of three-dimensional and periodic systems, such as crystalline solids. This makes it ideal for this project, which is limited to such materials except for a single O_2 molecule needed as reference for calculating v_{O} formation energies. For calculations of lower-dimensional systems, which by definition includes some amount of vacuum in the supercell, a considerable amount of computational effort goes into calculating PW's in the vacuum. For these systems, local basis sets consisting of AO's are usually more efficient. However, to allow for comparison, the O_2 molecule will be calculated using a PW basis as in all other calculations.

The pseudopotential method

The PW method seems like the most natural way to treat electrons in periodic solids. However, the wave functions exhibit steep gradients close to the nuclei, which requires large numbers of PWs to describe. The solution to this problem, as with other problems within DFT, lies in approximation. In 1935, Hellmann proposed treating atom kernels according to Thomas-Fermi theory, and valence electrons according to Schrödinger.⁹⁰ This is the first instance of the ‘‘pseudopotential’’ methodology, in which the actual potential is replaced with a different potential close to the nuclei for ease of computation. In 1937, Slater published what is known colloquially as the ‘‘muffin-tin approximation’’.⁹¹ Slater's idea was to approximate the potential exerted by the nuclei as spherically symmetric close to the atoms (the augmentation region), and constant in the interstitial regions between atoms, enforcing continuity on the boundary between the two regions. Electronic wave functions could then be treated using spherical harmonics close to the atoms, and using PWs in the interstitial regions.

Finally, Blöchl popularised the Projector Augmented-Wave (PAW) method,⁹² which is a generalization of the pseudopotential and muffin-tin approximation methods. In the PAW method, the physical valence wave functions are mapped onto pseudo wave functions by the linear transformation

$$\hat{L}_{\text{R}} = 1 + \sum_{\Omega} \hat{L}_{\Omega} \quad (2.30)$$

where \hat{L}_R operates only within some (atom-centered) augmentation region Ω_R . Generating good pseudopotentials is a non-trivial task, and they are generally supplied with any commercial package that uses them.

2.3.6 k point sampling

Analytically speaking, the Kohn-Sham equations “exist” everywhere in the scrutinised system. For computational purposes, though, a number of \mathbf{k} points are chosen in reciprocal space to evaluate the equations. Since a short lattice vector in real space results in a comparatively long lattice vector in reciprocal space, more \mathbf{k} points should be used to sample along short real-space lattice vectors. The conventional way of distributing \mathbf{k} points in the Brillouin zone is in a $(n \times m \times k)$ grid, as described by Monkhorst and Pack.⁹³

Special attention must be paid to the \mathbf{k} sampling when calculating electronic band structures. In this case, the electronic ground state density is first determined using a standard Monkhorst-Pack grid of \mathbf{k} points, followed by a “path” of \mathbf{k} points in the irreducible Brillouin zone, which visits the high-symmetry points. This dissertation uses the paths outlined in the work of Setyawan and Curtarolo.⁹⁴

2.4 Density functional tight-binding

The approximations of DFT allows the user to calculate properties for systems up to the order of ~ 1000 atoms, depending on the specific code used. However, real physical systems often have much larger sizes. For instance, in order to simulate a 10 nm thick resistive layer of λ -Ta₂O₅, one would need to simulate between $\sim 3 \times 10^4$ to $\sim 6 \times 10^4$ atoms, depending on the charge carrier transport direction relative to the cell. One method of pushing electronic structure calculations into the 10^4 range is the Density Functional Tight-Binding (DFTB) method.^{95–97}

2.4.1 DFT to DFTB

A full derivation of DFTB is beyond the scope of this dissertation; rather, key concepts are explained here. For a more thorough, yet immediate introduction, see e.g. Koskinen and Mäkinen,⁹⁸ upon which this summary is based. Starting from the Kohn-Sham energy functional Eq. (2.14), a system with density $\rho(\mathbf{r})$ is considered, which is written as a superposition of a reference density ρ_0 in the vicinity of ρ , and a fluctuation term $\delta\rho$, which is small compared to ρ_0 . Then, expanding the Kohn-Sham energy functional $E_{\text{KS}}[\rho]$ to second order in the fluctuation term $\delta\rho$ yields:

$$\begin{aligned}
 E_{\text{KS}}[\delta\rho] \approx & \sum_a f_a \langle \psi_a | -\frac{1}{2}\nabla^2 + V_{\text{ext}} + V_{\text{H}}[\rho_0] + V_{\text{XC}}[\rho_0] | \psi_a \rangle \\
 & + \frac{1}{2} \int \int \left(\frac{\delta^2 E_{\text{XC}}[\rho_0]}{\delta\rho\delta\rho'} + \frac{1}{|\mathbf{r} - \mathbf{r}'|} \delta\rho\delta\rho' \right) d\mathbf{r}d\mathbf{r}' \\
 & - \frac{1}{2} \int V_{\text{H}}[\rho_0](\mathbf{r}) \rho_0(\mathbf{r}) d\mathbf{r} + E_{\text{XC}}[\rho_0] + E_{\text{II}} - \int V_{\text{XC}}[\rho_0](\mathbf{r}) \rho_0(\mathbf{r}) d\mathbf{r} \quad (2.31)
 \end{aligned}$$

in which ψ_a is a single-particle state related to ρ with occupation $f_a \in [0, 2]$, and E_{II} denotes repulsion between ions. Equation (2.31) is structured such that the first term contains the band structure energy, E_{BS} , which is the zeroth order term of the charge transfer $\delta\rho$. Meanwhile, the second line contains charge-fluctuation terms in the form of Coulomb and XC interactions, E_{Coul} , and the third line constitutes the repulsive energy:

$$E_{\text{rep}} = -\frac{1}{2} \int V_{\text{H}}[\rho_0](\mathbf{r}) \rho_0(\mathbf{r}) d\mathbf{r} + E_{\text{XC}}[\rho_0] + E_{\text{II}} - \int V_{\text{XC}}[\rho_0](\mathbf{r}) \rho_0(\mathbf{r}) d\mathbf{r} \quad (2.32)$$

named after the ion-ion repulsive term E_{II} . The repulsive energy contains all effects from the core electrons. The charge density fluctuation $\delta\rho$ has an associated charge fluctuation, Δq , which may be related to each particular atom by dividing the entire space, Ω , into subspaces Ω_I . Each subspace then carries a local charge density fluctuation, $\delta\rho_I$, and corresponding charge fluctuation, Δq_I , the latter of which may be calculated as:

$$\Delta q_I \approx \int_{\Omega_I} \delta\rho(\mathbf{r}) d\mathbf{r} \quad (2.33)$$

This division is used to convert the energy contribution E_{Coul} from a double integral to a sum over atom pairs I, J and integrations over $\Omega_{I,J}$. In the case $I = J$, the coulombic energy contribution (second line of Equation (2.31)) reduces to:

$$E_{\text{Coul},IJ} \xrightarrow{I=J} \frac{1}{2} \Delta q_I^2 \int_{\Omega_I} \int_{\Omega_I} \left(\frac{\delta^2 E_{\text{XC}}[\rho_0]}{\delta\rho\delta\rho'} + \frac{1}{|\mathbf{r} - \mathbf{r}'|} \right) d\mathbf{r} d\mathbf{r}' \quad (2.34)$$

Meanwhile, when $I \neq J$, the XC-contribution vanishes for local XC-functionals if

$$\frac{\delta^2 E_{\text{XC}}}{\delta\rho(\mathbf{r})\delta\rho(\mathbf{r}')} \propto \delta(\mathbf{r} - \mathbf{r}') \quad (2.35)$$

In which $\delta(\mathbf{r} - \mathbf{r}')$ denotes the Dirac delta function. Then, the interaction is exclusively electrostatic:

$$E_{\text{Coul},IJ} \xrightarrow{I \neq J} \frac{1}{2} \Delta q_I \Delta q_J \int_{\Omega_I} \int_{\Omega_J} \frac{\delta\rho_I \delta\rho_J}{|\mathbf{r} - \mathbf{r}'|} d\mathbf{r} d\mathbf{r}' \quad (2.36)$$

In order to more concisely describe the electrostatic interactions, the following notation is introduced:

$$\gamma_{IJ} \equiv \int_{\Omega} \int_{\Omega} \frac{\delta\rho_I \delta\rho_J}{|\mathbf{r} - \mathbf{r}'|} d\mathbf{r} d\mathbf{r}' \quad (2.37)$$

For an analytic calculation of γ_{IJ} using a Gaussian distribution for $\delta\rho$, see Koskinen and Mäkinen.⁹⁸ With the subspace division, the repulsive energy becomes a sum over two-body repulsive functions, dependent only on atomic numbers:

$$E_{\text{rep}} \sum_{I < J} V_{\text{rep}}^{IJ}(|\mathbf{R}_J - \mathbf{R}_I|), \quad (2.38)$$

which will be elaborated upon shortly. Until now, no reference has been made to tight-binding; The derivation has focused solely on recasting the Kohn-Sham energy functional, introducing the concepts of charge and charge-density fluctuations, and dividing the computation space into subspaces. Now, the tight-binding formalism is introduced in order to describe the valence electrons.

2.4.2 Tight-binding

The tight-binding method refers to the electrons of the system being tightly bound to the atoms of the system. In DFTB, the valence electrons are expanded in a minimal local basis:

$$\psi_a(\mathbf{r}) = \sum_i c_{a,i} \phi_i(\mathbf{r}) \quad (2.39)$$

in which ϕ_i are basis functions analogous to in Section 2.3. ‘‘Minimal’’ refers to only having one radial function per angular momentum state (one, three, five, and seven for s , p , d , and f -states). The first term in Equation (2.31), E_{BS} , then becomes:

$$E_{\text{BS}} = \sum_a f_a \sum_{i,j} c_{a,i}^* c_{a,j} H_{ij}[\rho_0] \quad (2.40)$$

where the matrix elements of the Hamiltonian are

$$H_{ij}[\rho_0] = \langle \phi_i | H[\rho_0] | \phi_j \rangle \quad (2.41)$$

Returning to the basis functions ϕ_i , the electron population q on atom I may be determined as:

$$q_I = \sum_a f_a \int_{\Omega_I} |\psi_a(\mathbf{r})|^2 d\mathbf{r} = \sum_a f_a \sum_{i,j} c_{a,i}^* c_{a,j} \int_{\Omega_I} \phi_i^*(\mathbf{r}) \phi_j(\mathbf{r}) d\mathbf{r}, \quad (2.42)$$

Three different cases for indices i and j exist: i) if neither i or j refer to orbitals on atom I , the integral is roughly zero. ii) if both i and j refer to orbitals in atom I , the integral is roughly δ_{ij} (i.e., the Dirac δ function). iii) if i and j refer to orbitals on different atoms I and J , the integral becomes:

$$\int_{\Omega_I} \phi_i^*(\mathbf{r}) \phi_j(\mathbf{r}) d\mathbf{r} \approx \frac{1}{2} \int_{\Omega} \phi_i^*(\mathbf{r}) \phi_j(\mathbf{r}) d\mathbf{r} = \frac{1}{2} S_{ij}, \quad (2.43)$$

where S_{ij} is the overlap integral of basis functions ϕ_i and ϕ_j . Note the change from integrating over the local region Ω_I to integrating over cell volume Ω . The interpretation of Equation (2.43) is that approximately half of the overlap exists within Ω_I (the other approximate half exists within Ω_J). The total charge q_I on atom I is then given by

$$q_I = \sum_a f_a \sum_{i \in I} \sum_j \frac{1}{2} [c_{a,i}^* c_{a,j} + \text{c.c.}] S_{ij} \quad (2.44)$$

where c.c. stands for ‘‘complex conjugate’’ (of the preceding term). With this, the charge fluctuation term Δq may be given meaning as $\Delta q_I = q_I - q_I^0$, which recovers the population analysis of Mulliken.⁹⁹ Finally, the DFTB expression for the total energy is:

$$E = \sum_a f_a \sum_{i,j} c_{a,i}^* c_{a,j} H_{ij}[\rho_0] + \frac{1}{2} \sum_{I,J} \gamma_{IJ} \Delta q_I \Delta q_J + \sum_{I < J} V_{\text{rep}}^{IJ}(|\mathbf{R}_J - \mathbf{R}_I|), \quad (2.45)$$

in which the first term is the band structure energy, the second is the charge-fluctuation term, and the third is the repulsive term to be fitted as part of the parametrisation procedure.

2.4.3 The pseudo-atom

The majority of the tight-binding formalism has now been presented, and the derivation is approaching the practicalities of parametrisation. The basis functions ϕ_i were introduced in Equation (2.39) without much discussion, but it was hinted that they are described by spherical harmonics:

$$\phi_i(\mathbf{r}) = R_i(r)\tilde{Y}_i(\theta, \varphi) \quad (2.46)$$

with radial function R and spherical function \tilde{Y} . Since these are supposed to model bound electrons, it will not do to use the orbitals of a free atom. Instead, the “pseudo-atom” is introduced (analogous to pseudopotential), which is subjected to an additional confinement potential:

$$V_{\text{conf}}(r) = \sum_{i=0}^{\infty} v_{2i}r^{2i} \quad (2.47)$$

for which the symmetry requirement at $r = 0$ eliminates odd terms. To a first approximation, then, the confinement potential may be chosen as:

$$V_{\text{conf}}(r) = \left(\frac{r}{r_0}\right)^2 \quad (2.48)$$

where r_0 is the cutoff radius parameter which must be fitted for each (valence) orbital. Koskinen and Mäkinen suggests working from the covalent radius, $r_0 = 2 \cdot r_{\text{cov}}$, as a rule of thumb. For solids, the parameters are adjusted by comparing the band structure to a DFT reference.

2.4.4 Fitting the repulsive potential

The other, and more difficult, aspect of parametrising an element for DFTB lies in fitting the repulsive potential, V_{rep} . One method is to perform bulk modulus calculations using DFT and DFTB (with no repulsive potential), and fit a repulsive potential to the difference between these two. This requires that the material in question contain only uniform bond lengths, which is not the case for $\lambda\text{-Ta}_2\text{O}_5$. In general, there is no method that guarantees success, and this is the main sticking point of working with DFTB. More details on the fitting of the repulsive potential for the purposes of this dissertation are given in Chapter 5.

2.5 Computational Methods

With the above presentation of DFT, the general computational methods used in this dissertation will be presented now. In the few specific cases where a calculation deviates from the outline in this section, the deviation will be stated explicitly when that particular calculation is discussed.

All DFT calculations have been performed using the Vienna Ab initio Standard Package (VASP).^{100–103} The core electrons are described by PAW pseudopotentials,⁹² with valence electron configurations of $5p^65d^36s^2$ for Ta and $2s^22p^4$ for O. XC-effects are described by the PBE-GGA functional,⁸⁶ with some individual calculations employing HSE06, and still others employing the SCAN functional developed by Sun et al.ⁱⁱⁱ (noted in text where

ⁱⁱⁱMethod presented at APS March Meeting 2016 by J. Sun. Article available as pre-print at <https://arxiv.org/ftp/arxiv/papers/1511/1511.01089.pdf>

applicable). Atomic relaxations are considered converged when the difference in atomic forces between two iterations fall below $2.5 \times 10^{-2} \text{ eV \AA}^{-1}$, while the convergence threshold for electronic iterations is 10^{-5} eV .

The k point sampling standard employed is $(n_{k_a}, n_{k_b}, n_{k_c}) = (2 \times 2 \times 2)$ for a $\text{Ta}_{48}\text{O}_{120}$ supercell generated as a $(2 \times 2 \times 3)$ -repetition of the $\lambda\text{-Ta}_2\text{O}_5$ cell depicted in Figure 2.3. The supercell has lattice parameters $a = 12.50 \text{ \AA}$, $b = 14.80 \text{ \AA}$, and $c = 11.49 \text{ \AA}$. For systems presented in Chapter 4 deviating from this size, either a k point density of $3.5/\text{\AA}^{-3}$ is used, or k points are entered manually to ensure that the product of lattice vector and number of k points is ~ 25 . A cutoff energy of 520 eV is used for all calculations, which was determined from VASP’s guidelines for high precision, $E_{\text{cut}} = 1.3 \cdot E_{\text{max}}$, where $E_{\text{max}} = 400 \text{ eV}$ for the O pseudopotential ($E_{\text{max}} = 223.667 \text{ eV}$ for the Ta pseudopotential).

Amorphous structures are generated with Ab Initio Molecular Dynamics (AIMD), using the Nosé-Hoover algorithm to describe the heat reservoir.^{104,105} The template structure is the $\text{Ta}_{48}\text{O}_{120}$ supercell described above. Stoichiometries are varied by randomly generating 0, 8, 12, 16, 20, and 24 v_{O} in the template structure, which resulted in stoichiometries Ta_2O_5 , Ta_3O_7 , Ta_4O_9 , Ta_6O_{13} , $\text{Ta}_{12}\text{O}_{25}$, and TaO_2 , respectively. Each stoichiometrically different supercell is then expanded by a factor of 1.06 along each lattice vector, to reach the density of amorphous Ta_2O_5 and give ample room for atoms to move around. For each stoichiometry, an initial equilibration at 5000 K for 10 ps is performed to melt the structure. Continuing the equilibration, fourteen structure snapshots are extracted per stoichiometry in intervals of 2 ps for a total equilibration time of 36 ps. Following the initial equilibration, each individual snapshot is quenched to 300 K at a rate of 200 K ps^{-1} . Snapshots are then equilibrated at 300 K for 2 ps, concluding the AIMD structure generation procedure. Equilibrations use a MD time step of 1 fs, while quenches use 2 fs. The AIMD calculations use a high speed/low accuracy setup with cutoff energy 300 eV, sampling only the Γ point. The (expanded) cell vectors are kept fixed for the entire AIMD procedure. Having obtained completely randomized structures, a relaxation of atomic positions and lattice vector is performed using the standard DFT accuracy outlined above. Finally, a single Γ -point calculation for each snapshot is performed using HSE06 to generate accurate descriptions of key quantities.

Chapter 3

Amorphous tantalum oxide

3.1 Introduction

As described in Section 2.2, the resistive layer in TaO_x-based ReRAM devices likely consist predominantly of amorphous regions. Further, the stoichiometry of as-fabricated thin films seems to change continuously from slightly oxygen-deficient Ta₂O₅ near the surface, to similarly oxygen-deficient TaO₂ in the bulk of the thin film. Although this characteristic has been known since 2008 for ReRAM devices and 1993 for a-TaO_x in general, few theoretical studies have investigated amorphous TaO_x on the atomic scale. Lee et al. sampled an amorphous Ta₂O₅-structure to serve as basis for comparison to their λ model.⁶⁰ Bondi et al. performed rigorous sampling of both stoichiometric and sub-stoichiometric Ta₂O₅, however, their focus was on conductivity of O-deficient phases,¹⁰⁶ interfacial effects on v_O formation energy,¹⁰⁷ and relations between single-vacancy conductivity and atomic structure.¹⁰⁸ Xiao and Watanabe simulated amorphous TaO_x with varying oxygen content,¹⁰⁹ but the study was limited to a single sample per stoichiometry.

So far, no study has investigated the stability in terms of total energy of any sub-stoichiometric a-TaO_x phase to the knowledge of this author. Such a study is an important piece of the picture, when stoichiometry change constitutes the working principle of a device. Stoichiometries can be determined experimentally, for instance by use of XPS analysis. Obtained XPS spectra may be deconvoluted using Gaussian/Lorentzian functions, after which the individual Gaussian/Lorentzians are assigned either to different Ta oxidation states or to their corresponding stoichiometries, i.e., Ta₂O₅ (Ta⁵⁺), TaO₂ (Ta⁴⁺), etc. This method is hardly exact, owing partly to the size of realistic samples and partly to the stochastic nature of amorphous materials. DFT studies may model such an XPS spectrum through calculation of the core level energies of electrons belonging to the constituent atoms, providing basis for comparison to experiment. An important benefit of using DFT simulations is that knowledge of the atomic structure is complete.

This chapter presents AIMD-calculations on six amorphous phases of a-Ta₂O_{5-x} with $x \in \{0.00, 0.33, 0.50, 0.67, 0.80, 1.00\}$, corresponding to stoichiometries of Ta₂O₅, Ta₃O₇, Ta₄O₉, Ta₆O₁₃, Ta₁₂O₂₅, and TaO₂. The structures are investigated with respect to their total energies, XPS spectra, and oxidation states based on a Bader charge analysis. Due to the stochastic nature of amorphous structures, it is necessary to sample several structures of the same stoichiometry in order to extract reliable information. For this reason, each considered stoichiometry samples fourteen individual snapshots extracted at 2 ps intervals

and independently quenched. Each snapshot is subsequently relaxed, and the total energy is calculated for the relaxed structure and converted to a relative energy in terms of phase separation into the end points, Ta_2O_5 and TaO_2 . The relative energy analysis reveals that a hitherto unknown phase with stoichiometry Ta_6O_{13} may be metastable. Simulated XPS spectra for Ta_2O_5 and TaO_2 agree well with experiment in terms of Ta 4f peak locations. However, the TaO_2 spectrum contains both the Ta^{5+} and the Ta^{4+} peaks, and further, the Ta^{4+} peak consists of a wide range of disproportionated atoms with very different oxidation states. This information suggests that the conventional understanding of a- TaO_x XPS spectra – and possibly amorphous ionic solids in general – is lacking. The relation between oxidation state spectrum and XPS spectrum is examined using a Gaussian peak fitting model, which is found to provide a remarkably good fit between peak values.

3.2 Convex Hull of the a- Ta_2O_5 – TaO_2 system

The convex hull of the a- Ta_2O_5 – TaO_2 system is visualised in Figure 3.1(a). Most notably, the hull shows preference for phase separation into Ta_2O_5 and TaO_2 . However, the stoichiometry Ta_6O_{13} lies considerably closer (108 meV/fu) to the hull than the three other intermediate stoichiometries, which all lie far above the hull (>600 meV/fu). For this reason, the stoichiometries Ta_2O_5 , Ta_6O_{13} , and TaO_2 will henceforth be referred to as “low-energy” stoichiometries, while Ta_3O_7 , Ta_4O_9 , and $\text{Ta}_{12}\text{O}_{25}$ will be referred to as “high-energy” stoichiometries. The calculated mean density of a- Ta_2O_5 is $6.87 \times 10^3 \text{ kg m}^{-3}$, which matches the experimental density of $6.88 \times 10^3 \text{ kg m}^{-3}$ (for more information, see Appendix C).

To investigate what sets the low-energy stoichiometries apart from the high-energy stoichiometries, the CDF of every stoichiometry is examined in Figure 3.1(b). Since the preferred

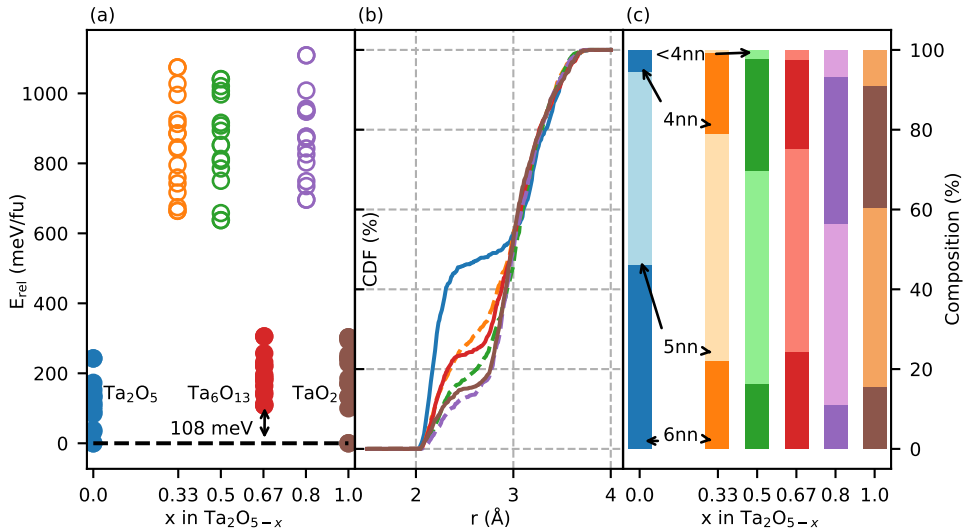


Figure 3.1: (a): Convex hull for the Ta_2O_5 – TaO_2 system. (b): CDF for each considered stoichiometry, limited to the sixth-nearest neighbours. Dashed lines correspond to stoichiometries with empty circles in (a). (c): Percentwise distribution of Ta coordination numbers. Colour coding is consistent throughout. (b+c) share y axis scale.

coordination number of Ta in crystalline phases is six, the CDF analysis is limited to the sixth-nearest neighbours; i.e. the five closest O atoms are not included. In each case, the CDF spectrum exhibits an ascent beginning at $\sim 2.0 \text{ \AA}$ and a subsequent plateau slightly before 2.5 \AA . The low-energy stoichiometries, however, exhibit steeper ascents and more flat plateaus than the high-energy stoichiometries, indicating that more Ta atoms may be considered sixfold coordinated. Since coordination numbers are poorly defined in amorphous systems, the location of the plateau – i.e. 2.5 \AA – is designated as the “cutoff radius” for Ta coordination. Hence, an O atom will count towards the coordination number of a Ta atom if it lies within a radius of 2.5 \AA of said Ta atom. The height of the initial ascent in Figure 3.1(b) thus approximates the degree of sixfold coordination.

Based on this definition, a compositional analysis is made for coordination numbers of Ta atoms in each stoichiometry. Figure 3.1(c) presents this analysis for numbers of nearest neighbours (nn) 6, 5, 4, and < 4 . The relatively higher degrees of sixfold coordination in the low-energy stoichiometries is found to go hand in hand with lower degrees of fourfold and less-than-fourfold coordination.

3.2.1 Comparison to crystalline Group V metal oxides

Revesz et al. remarked that their observed optical spectra of a-Ta₂O₅ closely resembled spectra of crystalline Ta₂O₅, and that this indicates a strong similarity in their short-range order structures.⁵⁰ The following analysis builds on this statement by explaining the relatively high degree of sixfold coordination and energetic stability of Ta₂O₅, Ta₆O₁₃, and TaO₂ by means of a parallel to crystalline structures.

Of the stoichiometries considered in Figure 3.1, only Ta₂O₅ and TaO₂ have a corresponding crystalline phase. In all the simple low-temperature phases of Ta₂O₅ (β , δ , and λ), the Ta ions are sixfold coordinated. Likewise, TaO₂ has crystallised both in the rutile structure and in the larger tetragonal structure of Khitrova et al.,¹¹⁰ with full sixfold Ta coordination in both cases. However, since neither Ta₃O₇, Ta₄O₉, Ta₆O₁₃, nor Ta₁₂O₂₅ have been observed, this study instead considers vanadium, which shares periodic table Group V with tantalum. Vanadium has been observed to crystallise in stoichiometries V₃O₇,¹¹¹ V₄O₉,¹¹² and V₆O₁₃.¹¹³ Of these three phases, only V₆O₁₃ exhibits full sixfold coordination of all V atoms. In contrast, only one third of V atoms in V₃O₇ are sixfold coordinated, while one half are sixfold coordinated in V₄O₉. No stoichiometry corresponding to Ta₁₂O₂₅ has been found for either Group V element. This analysis highlights the importance of sixfold coordination for Ta atoms in a-TaO_x, and compounds the observation made by Revesz et al. that the short-range order in amorphous and crystalline Ta₂O₅ is similar.

An important question arises following the above comparison. How sensitive is the relative energy to the exactness of the stoichiometry? The Ta₁₂O₂₅ system (purple open circles in Figure 3.1(a)) holds just four O atoms more than TaO₂ for a system with 168 atoms (including v_{O}), yet the difference in sixfold coordination, and hence E_{rel} , is profound. The question is not answered here, since doing so would likely require at least three more series of amorphous TaO_x be calculated, in order to obtain single- v_{O} resolution between the studied stoichiometries.

3.3 Simulated XPS spectra

XPS is an important characterisation technique for compositional analysis. By measuring the photoelectric signal a sample, a researcher may compare the obtained Binding Energies (BEs) to table values to determine the constituent atoms, their oxidation states,

and the relative composition of the sample. This is especially important for characterising amorphous materials, where conventional x-ray spectroscopy offers more limited information than for crystalline samples. Conventionally, an amorphous XPS spectrum is deconvoluted into Gaussian/Lorentzian components representing different oxidation states. These oxidation states are either named directly or according to their corresponding stoichiometries; i.e. Ta^{5+} , Ta^{4+} , Ta^{3+} , Ta^{2+} , Ta^{1+} , and Ta^0 may be referred to as Ta_2O_5 , TaO_2 , Ta_2O_3 , TaO , Ta_2O , and Ta , respectively.

In this section, simulated XPS spectra are presented for the Ta 4f orbitals in a- Ta_2O_5 and a- TaO_2 and compared to experiments. Note that spin-orbit interactions split the experimental XPS peaks into two; $\text{Ta}_{7/2}$ and $\text{Ta}_{5/2}$. This is not captured in the simulated XPS analysis due to the absence of spin-orbit interactions. XPS spectra are obtained in the initial state approximation, in which the Kohn-Sham eigenvalues for the core electrons are recalculated following a self-consistent evaluation of the valence charge density.

3.3.1 Calibration of simulated XPS spectra

Before comparisons can be made, the as-calculated core level energies must be properly “calibrated”. First and foremost, a constant shift of all core level energies must be imposed in order to compare XPS energies directly. This displacement is determined as the difference between the $\text{Ta}_{7/2}^{4f}$ XPS peak location observed for crystalline Ta_2O_5 by Ho et al.,¹¹⁴ (26.2 eV) and the Ta 4f core level energy calculated for crystalline Ta_2O_5 in the λ phase (19.1 eV). The resultant BE shift is 7.1 eV, which is applied to all calculated core level energies. Such a shift is necessary in order to achieve a direct comparison between simulation and experiment.¹¹⁵

Another important difference between experimental XPS spectra and DFT calculations is the finite temperature of experiments. While XPS measurements typically take place at room temperature, DFT calculations take place at absolute zero. To overcome this difference, an MD-equilibration was performed for 2 ps using the precision of regular DFT calculations. The resultant energy spectrum was used for a Gaussian fit, whose width was subsequently used to broaden the calculated XPS spectra.

3.3.2 Comparison between simulated and experimental XPS spectra

With the above calibrations, the as-calculated XPS spectra for a- Ta_2O_5 and a- TaO_2 may be compared to experimentally observed peak locations. Specifically, the works of Benito and Palacio (BP15),¹¹⁶ Simpson et al. (S17),¹¹⁷ and Li et al. (L19)³¹ are used as the basis for the comparison. Figure 3.2(a) shows the simulated XPS spectra for a- Ta_2O_5 , along with a peak fit consisting of a single Gaussian. The Gaussian offers a near-perfect fit, signifying that the simulated XPS spectrum has the same character as an experimental spectrum. The peak is located at 27.2 eV, which is 0.1 eV to 0.3 eV higher than the values of 26.9 eV,¹¹⁶ 27.0 eV,¹¹⁷ and 27.1 eV³¹ observed in experiments. For TaO_2 , the Gaussian decomposition into two individual peaks provides a good fit to the as-calculated curve. By comparison to the peak values observed in the cited works, it is seen that the Gaussian components correspond well to the Ta^{5+} and Ta^{4+} peaks, respectively. The Ta^{5+} component has its peak at 27.3 eV, which is 0.2 eV to 0.4 eV above the experimentally obtained peaks, while the Ta^{4+} peak location is at 25.9 eV, which lies within a distance of -0.2 eV to 0.4 eV from the corresponding experimental peaks. The distance between the two simulated peaks is 1.4 eV, while the experimental distances are 0.8 eV (BP15), 1.3 eV (S17), and 1.6 eV (L19). The wide variance in the 5+ and 4+ peak distances complicates any direct comparison, but

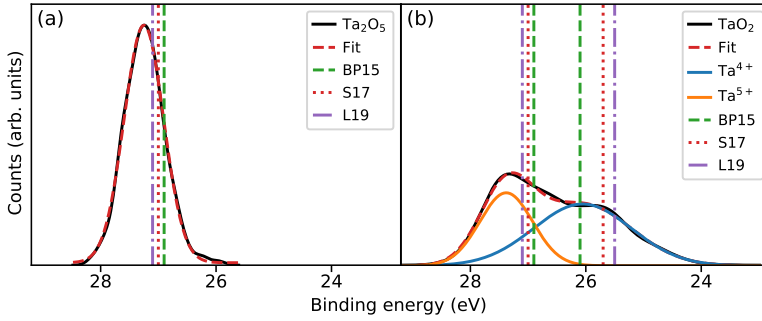


Figure 3.2: (a): Simulated XPS spectrum (black full line) and Gaussian fit (red dashed line) of α - Ta_2O_5 . (b): Same analysis for α - TaO_2 . Also shown are Gaussian components corresponding to Ta^{5+} and Ta^{4+} . Vertical dashed lines show peak locations of references 116, 117, and 31 (see legend).

the simulated Ta^{5+} - Ta^{4+} distance lies in the middle of the interval provided by experiment. To conclude the above comparison, the simulated XPS results indeed correspond to the XPS peaks obtained experimentally for Ta^{5+} and Ta^{4+} .

The simulated XPS spectrum of Figure 3.2(b) contains two particularly important results. First, the TaO_2 spectrum displays a significant contribution to its XPS spectrum coming from Ta^{5+} . This result challenges the conventional 1:1 mapping between the nominal oxidation state and corresponding stoichiometry (e.g. $\text{TaO}_2 \leftrightarrow \text{Ta}^{4+}$). According to the simulated XPS spectra, a conventional compositional analysis using XPS can yield significant Ta_2O_5 content even for an amorphous sample with exact stoichiometry TaO_2 .

The second important result pertains to the component representing the Ta^{4+} peak. In experimental spectra, XPS peaks have similar widths (see e.g. reference 31). However, the simulated Ta^{4+} peak is significantly wider than experimental peaks. This suggests that the peak may be fundamentally different from what is currently believed about it. This difference is the topic of the following section.

3.4 Bader charge analysis

Since different XPS peaks are associated with different oxidation states, an analysis based on Bader charge is performed.¹¹⁸ In particular, the all-electron charge density is computed and subsequently analysed using scripts made freely available by the group of Henkelman.ⁱ The calculated Bader charges provide a qualitative description of the oxidation states of the atoms in a sample, although the numerical values differ from nominal oxidation states. The values reported here are given relative to the number of valence electrons; i.e. a Bader charge of +1 assigned to a Ta ion means it has “given up” one of its valence electrons.

Figure 3.3(a-c) plots BE versus Bader charge for the low energy stoichiometries shown in Figure 3.1; i.e. Ta_2O_5 , Ta_6O_{13} , and TaO_2 . Atoms are colour and shape coded to reflect number of nn’s according to the 2.5 Å rule described in Section 3.2. The black dashed lines are Kernel Density Estimates (KDE) of the spectra. Also shown in Figure 3.3(a) are Bader charges and BEs for crystalline tantalum oxide phases with nominal oxidation states ranging from +5 (Ta_2O_5) to 0 (Ta). For Ta_2O_5 , the XPS peak is seen to originate from a narrow range of Bader charges centered around +3. The colour coding shows that

ⁱSee <http://theory.cm.utexas.edu/henkelman/> for more information and downloads.

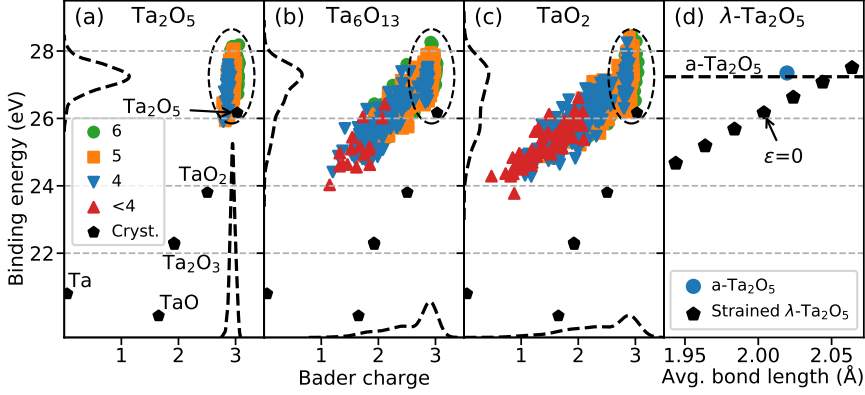


Figure 3.3: (a-c): Core level energy plotted vs. Bader charge for the low-energy stoichiometries. Colours represent Ta atoms with different numbers of nearest neighbours, as indicated in the legend. Dashed lines show KDEs for the distributions. (d) Total energy versus average bond length for λ -Ta₂O₅ for strains between -3% and $+3\%$. Dashed line shows average energy for sixfold coordinated Ta atoms in a-Ta₂O₅.

the undercoordination demonstrated in Figure 3.1 results in a small, but visible tail of the Bader charge spectrum towards lower values. Similarly, there is a small tendency of undercoordinated Ta atoms to possess lower BEs.

For Ta₆O₁₃ and TaO₂ in Figure 3.3(b-c), this picture changes noticeably. There are, however, visible remnants of the Ta₂O₅ signal (highlighted by the dashed ellipses) present in both spectra. These are mirrored as “blunted” peaks in their respective Bader charge spectra, firmly establishing the connection between stoichiometry-dependant short-range order, Bader charge, and BE.

Apart from this, both the Bader charge and the XPS spectra are smeared towards lower charge and lower BE, respectively. This tail of the Bader/XPS spectra is seen to originate almost exclusively from undercoordinated atoms. Evidently, while a large portion of atoms are able to retain the preferred $+5$ oxidation state characteristic of Ta₂O₅, this bears the cost of disproportionation for all other Ta atoms. The comparison to crystalline BE/Bader charge shows that the peak calculated for TaO₂ actually includes atoms with Bader charges (and hence, oxidation states) well below the Bader charge of Ta atoms in TaO. For this reason, caution is advised for researchers using XPS to perform compositional analyses of amorphous tantalum oxide, and possibly of amorphous metal oxides in general.

3.4.1 Differences between crystalline and amorphous Ta₂O₅

The discussion of XPS spectra is now reinforced with a comment on BEs in crystalline versus amorphous Ta₂O₅. The reader is reminded that the calibration of the simulated XPS spectra was performed by benchmarking the calculated BE of λ -Ta₂O₅ against the Ta⁵⁺ peak value of 26.2 eV obtained by Ho et al.¹¹⁴ Meanwhile, the results for the corresponding value for amorphous tantalum oxide are 26.9 eV,¹¹⁶ 27.0 eV,¹¹⁷ and 27.1 eV.³¹ The calculated data points for crystalline tantalum oxide phases shown in Figure 3.3 also possess lower BEs than their amorphous counterparts. In Figure 3.3(d), this discrepancy is examined by calculating total energies for λ -Ta₂O₅ subjected to a relative strain $\eta \in [-3\%, +3\%]$. The BE for Ta 4f in the λ phase is seen to increase quasi-linearly with average Ta–O bond length in the considered region. This behaviour is expected as Coulomb repulsion between the

Ta 4f electrons and the O ligands decreases (increases) for increasing (decreasing) Ta–O distance, driving the 4f BE up (down). The average Ta–O bond length to the sixth-nearest O neighbour corresponds well to the bond length in λ -Ta₂O₅ strained to +1% relative strain, which has a higher BE. The larger BE for amorphous tantalum oxide may thus be partially explained by the greater bond lengths.

3.5 Bader charge/XPS peak fitting

The scatter plots of core level energies vs. Bader charge in Figure 3.3(a-c) show a loose linear correlation between the two. However, the prevalence of the Ta₂O₅ spectrum in the spectra of Ta₆O₁₃ and TaO₂ complicates this picture. Clearly, the narrow Bader charge spectrum of Ta₂O₅ lends itself poorly to any simple linear regression. Instead, the XPS and Bader charge spectra are decomposed into Gaussians, and the relation between peak levels is investigated. The spectra of Ta₆O₁₃ and TaO₂ achieve the best fit in terms of residual sum of squares when three Gaussians are used, while a single Gaussian is used for Ta₂O₅ due to the distinctly bell-like shape of both spectra.

Figure 3.4(a-f) presents the Gaussian fits to the as-calculated XPS (a-c) and Bader charge (d-f) spectra. Each curve is accurately represented by the Gaussian decompositions as seen by the good correspondence between the as-calculated (black) curves and the fitted (red) curves. Figure 3.4(g) plots the peak locations of the XPS spectra versus those of the Bader charge spectra, achieving a good regression with correlation coefficient $r^2 = 0.99$. This analysis emphasises the stochastic nature inherent in amorphous tantalum oxide, and is likely exemplary of other amorphous and binary metal oxides.

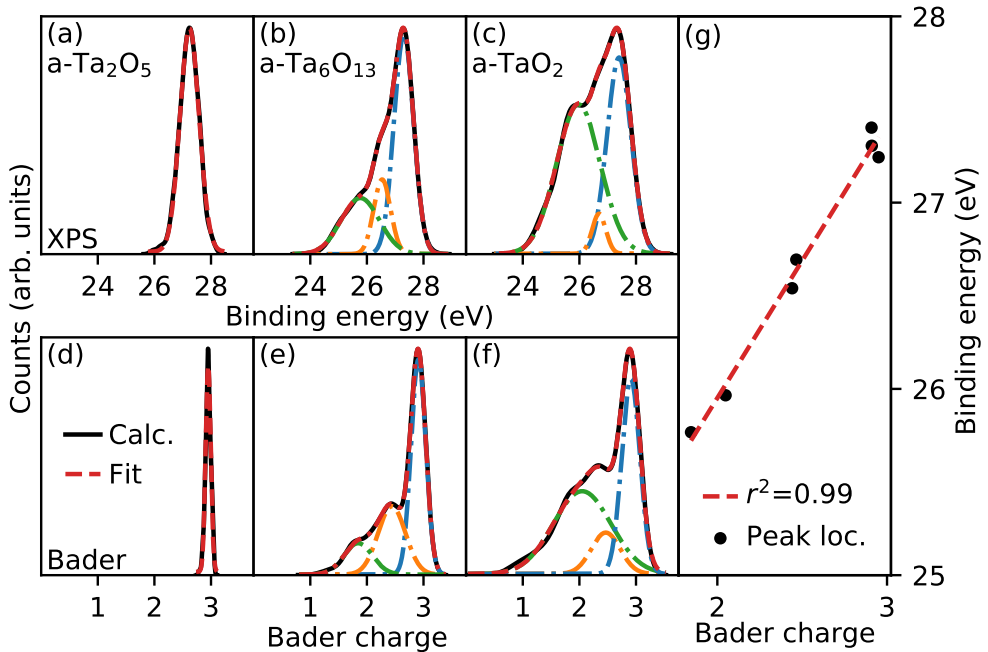


Figure 3.4: (a-c): Fitting of Gaussians to the XPS spectra of Ta₂O₅, Ta₆O₁₃, and TaO₂, respectively. (d-f): Same analysis using Bader charge spectra. (g): Linear correlation between Bader charge/XPS peak locations. Legend in (d) applies to (a-f).

3.6 Simulated XPS depth profile

The work of Li et al.¹¹⁹ presents XPS depth profiles for an as-fabricated TiN/TaO_x/W sample as well as equivalent samples annealed at 350 °C and 500 °C. Their work has one novelty of particular importance to this thesis: Ratios of O to Ta for each sample are also provided. This allows for direct stoichiometry-controlled comparison between the simulated XPS spectra of low-energy stoichiometries and experimental XPS spectra of the same stoichiometries. Such a comparison is now made to conclude this chapter. To add to the depth profile, a series of calculations has been done to simulate amorphous Ta₁₂O₂₉, which lies between Ta₂O₅ and Ta₃O₇ (open orange circles) on the stoichiometry axis in Figure 3.1. The stoichiometry Ta₁₂O₂₉ was chosen based on calculations of crystalline phases, which will be presented in the next chapter. a-Ta₁₂O₂₉ qualifies as a low-energy stoichiometry.

Figure 3.5(a) reprints the XPS depth profile obtained by Li et al. for the TaO_x layer in a TiN/TaO_x/W heterostructure after annealing at 500 °C. This particular profile was chosen over the two others because its stoichiometry changes more slowly, and contains points very similar to the simulated low-energy stoichiometries (see arrows in Figure 3.5(b)), with the exception of Ta₁₂O₂₉ which has slightly higher O content than the curve it is mapped onto. As seen from the depth profile, the sample initially shows only the Ta⁵⁺ peaks, corresponding to stoichiometric Ta₂O₅. The subsequent XPS lines gradually grow a tail towards lower BEs, signifying decreasing O content. This is compounded by the brown curve in Figure 3.5(b), which shows the O/Ta ratios for the sample in (a).

Finally, Figure 3.5(c) attempts to map the simulated XPS spectra of this dissertation onto the XPS spectra in frame (a). Black arrows point from simulated XPS spectra to their experimentally observed counterparts. The four stoichiometries will now be discussed individually.

i) The correspondence for Ta₂O₅ is good, as was found in Section 3.3, considering that the DFT calculations do not account for spin-orbit interactions. ii) For Ta₁₂O₂₉, a slight tail has developed, which is also seen in the experimental XPS line. The simulated tail does not extend to the 26 eV to 24 eV region, however, as is observed experimentally. Note also that the oxygen ratio of Ta₁₂O₂₉ is 2.42, which is greater than the corresponding point on the O/Ta curve in (b). iii) For Ta₆O₁₃, the tail has extended into the 26 eV to 24 eV region and partly captures the tail also seen in experiment. However, the experimental tail continues to ~22.0 eV. This suggests that the experimental sample contains a small amount of Ta atoms with oxidation state below 4+, which is not captured in the simulation. iv) For TaO₂, the picture is similar to that of Ta₆O₁₃. The simulation predicts a stronger Ta⁴⁺ signal than the experiment, but the further development of the tail in the region 26 eV to 24 eV region as compared to Ta₆O₁₃ is consistent with the difference between the corresponding experimental curves. This may be seen by the comparatively greater distance between curves number three and four in Figure 3.5(a) (counting from the bottom) for the specified energy interval. The overpronounced Ta⁴⁺ shoulder and subsequent missing tail at BE < 24.0 eV suggests that the DFT model presents a more idealised form of the amorphous samples than are obtained experimentally.

To conclude this analysis, the simulated XPS spectra accurately captures features found in experimental XPS spectra, in particular the peak at ~27.0 eV and subsequent tail development between 26.0 eV and 24.0 eV. However, features at lower energies are not reproduced by DFT for these stoichiometries. Modelling of XPS spectra below the stoichiometry of TaO₂ might provide more insight as to the reasons for the lack of signal below 24.0 eV.

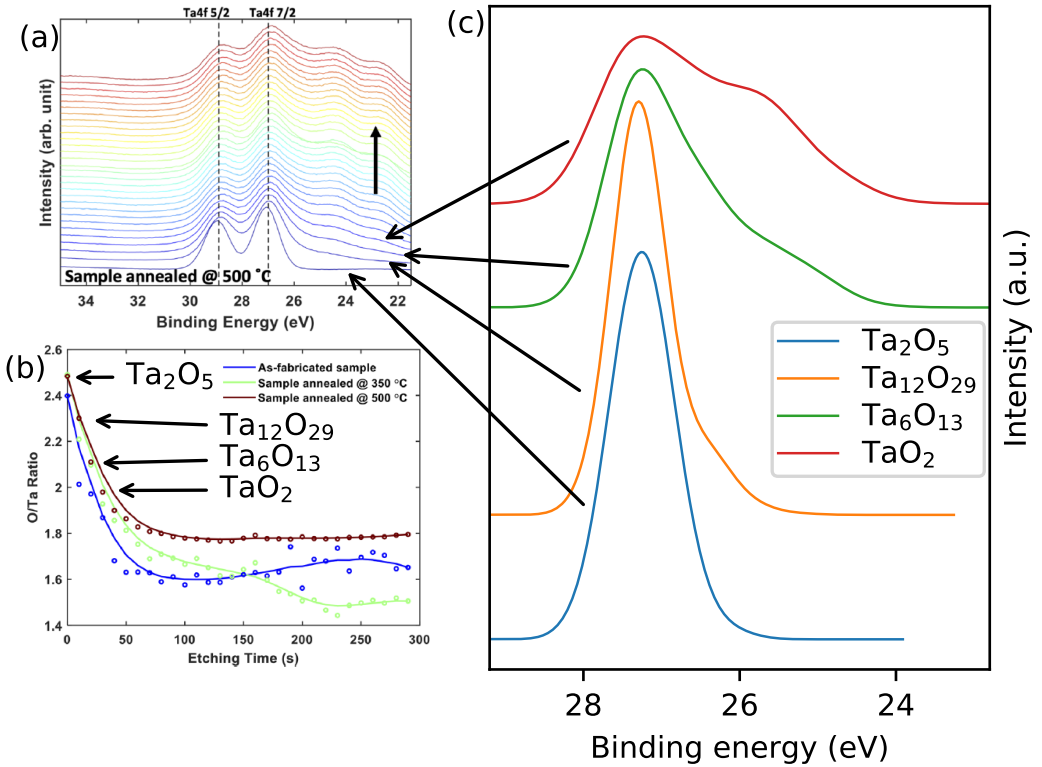


Figure 3.5: (a): Experimental XPS depth profile for TaO_x sample annealed at 500 °C. Vertical black arrow shows direction of profiling. (b): Stoichiometry as O/Ta ratio. Brown curve corresponds to the spectrum in (a). Black arrows highlight points on the brown curve. (c): Simulated XPS spectra for Ta₂O₅, Ta₁₂O₂₉, Ta₆O₁₃, and TaO₂. Arrows point to the four lowest XPS lines as indicated by the arrows. (a-b) reproduced from reference 119, with the permission of AIP Publishing. All arrows except XPS profile direction in (a) have been added for the purposes of this dissertation.

Chapter 4

Crystalline tantalum oxide

4.1 Introduction

The previous section expanded on the atomic-level knowledge of amorphous TaO_x in order to investigate stoichiometry change in ReRAM devices. However, as described in Section 2.2, even predominantly amorphous TaO_x layers may contain crystallites, either in the as-formed films²³ or as a result of switching operations.³² In addition to this, and along a different line of study, reduced $\text{Ta}_2\text{O}_{5-x}$ (or TaO_x) has been studied for use in electrocatalysis.^{120,121} Finally, and in a recent study, Korshunov et al. oxidised Ta to create TaO_x nanoparticles with O/Ta ratios between 1.7–2.2, depending on oxidation time and temperature. For these reasons, crystalline and reduced tantalum oxide is investigated in this chapter.

One important distinction should be made prior to this study; namely between *oxygen-deficient* and *oxygen vacancy-defective*. The AIMD-generation of amorphous TaO_x resulted in structures that were oxygen-deficient by design, but which had no identifiable defects. For crystalline structures, however, oxygen deficiency must either take the form of oxygen vacancies or as phase change from one crystalline phase (e.g. orthorhombic Ta_2O_5) to a reduced crystalline phase (e.g. tetragonal TaO_2). Since the most stable tantalum oxygen phase is $\lambda\text{-Ta}_2\text{O}_5$ according to Lee et al.,⁶⁰ it makes sense to focus on reduction of $\lambda\text{-Ta}_2\text{O}_5$ through creation of oxygen vacancies in large concentrations.

Such a study presents a challenge, however, in terms of its size. In order to be able to sample different v_{O} -distributions, a relatively large system size is needed. Meeting this need, in turn, drastically increases the number of possible v_{O} distributions – distributing 12 v_{O} among 120 O atoms can be done in $\sim 10^{16}$ different ways! To address and overcome this challenge, the Atomic Simulation Environment (ASE) library,¹²³ together with the Cluster Expansion for ASE (CLEASE)¹²⁴ code, are employed to accelerate the search for low-energy configurations of Ta_2O_5 reduced by v_{O} .

For the precise treatment of v_{O} , correction terms in the form of a Hubbard-like U term (see e.g. Dudarev et al.)¹²⁵ have been suggested, and applied successfully to describe defects in e.g. rutile TiO_2 .¹²⁶ This possibility has been evaluated (see Appendix A), and it was found that regular PBE provides a qualitatively more accurate description of v_{O} formation energies with respect to HSE. Briefly, the 3f ip v_{O} site is predicted to be most stable by far using both PBE and HSE, while adding a +U parameter changes this picture dramatically. To further document the validity of regular PBE for the description of v_{O} in bulk Ta_2O_5 , the

reader is referred to Appendix B, where real-space charge densities calculated using PBE and HSE are compared. Hence, the PBE+U method has not been adopted in this study.

With the aid of CLEASE, the search for low-energy structures is performed using only 186 DFT calculations. The structure search finds a new reduced tantalum oxide phase with stoichiometry Ta_4O_9 ($\text{Ta}_2\text{O}_{5-0.5}$) which is stable with respect to phase separation of Ta_2O_5 and TaO_2 . The v_{O} defects aggregate in pairs within the Ta_2O_3 planes, which further aggregate in chains in the out-of-plane direction, i.e. defect pairs occupy the same lattice positions in each successive plane. The Ta_4O_9 structure is described with a monoclinic primitive cell consisting of 26 atoms and a single defect pair. The defect pair results in two midgap bands lying 1.12 eV below the conduction band with flat dispersion. The wave functions associated with these bands are spatially localised on or around the defect center, and show a strong character of the d orbitals of neighbouring under-coordinated Ta ions. These orbitals form a bonding arrangement which raises the neighbouring Ta ions to full coordination, stabilising the pair defect at high v_{O} concentrations as compared to maximal v_{O} separation. Finally, a convex hull is presented for a structure search among crystalline phases reported in literature for predominantly Group V metal oxides. Remarkably, this search suggests that the shear structures $\text{Ta}_{11}\text{O}_{27}$ and $\text{Ta}_{12}\text{O}_{29}$ are stable, and that TaO is metastable with very low relative energy.

4.2 Convex hull of v_{O} -defective $\lambda\text{-Ta}_2\text{O}_5$

The primary results of the CLEASE-enhanced structure search are presented in this section. Figure 4.1(a) shows the convex hull of $\text{Ta}_2\text{O}_{5-x}$, $x \in [0, 1]$, with respect to phase separation into $\lambda\text{-Ta}_2\text{O}_5$ and tetragonal TaO_2 in the model of Khitrova et al., labelled “K1967”.¹¹⁰ This model for TaO_2 was chosen due to its lower total energy as compared to rutile TaO_2 , which is also shown. The hull shows a preference for a solid solution of v_{O} over a phase separation into Ta_2O_5 and TaO_2 . In particular, the stoichiometry Ta_4O_9 corresponding to $x = 0.5$ is stable, with other low-energy structures lying either close to Ta_2O_5 or to Ta_4O_9 . Also included is the relative energy of rutile TaO_2 and phase separated Ta_2O_5 and Ta, the latter of which is the most stable configuration of that particular stoichiometry.

Figure 4.1(b) shows the prediction strength of the Cluster Expansion model. The calculated total energies lie close to the $E_{\text{CE}} = E_{\text{DFT}}$ line, signifying good agreement between

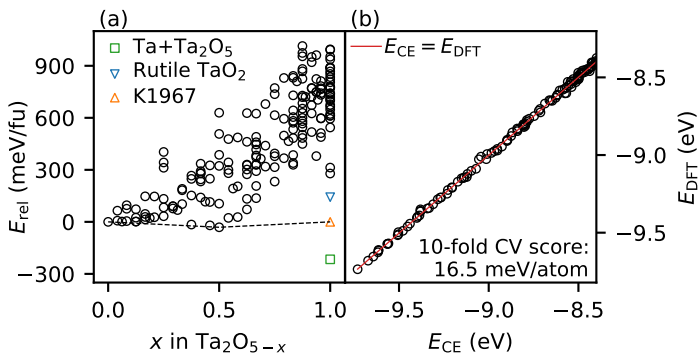


Figure 4.1: (a): Convex hull for the v_{O} -defective $\text{Ta}_2\text{O}_5\text{-TaO}_2$ system. (b): Fit quality of the CLEASE model. Black circles represent DFT-evaluated structures, while the red line represents the “perfect” model $E_{\text{CE}} = E_{\text{DFT}}$.

the prediction of the model and the actual observations from DFT. The 10-fold CV score of 16.5 meV/atom is higher than it could be. This is partly due to the lattice distortions induced by the vacancies, which amounts to noise in the model which assumes an ideal lattice. Moreover, the CV score reflects important decisions made in regards to sampling. In training the model, it was emphasised that the configuration space should be sampled with little or no bias. For instance, it would be possible to include every symmetrically inequivalent distribution of 1, 2, 3, and 4 v_{O} in a smaller Ta_8O_{20} supercell. This could technically increase the accuracy of the model due to heavy sampling of the subset of configuration space realisable with the constraints imposed by the small supercell. However, doing so would give the model a disproportionately large degree of knowledge of such configurations as are found for small cells, possibly leading to a bias towards these configurations.

Although Ta_4O_9 is unstable with respect to $\text{Ta}_2\text{O}_5 + \text{Ta}$, it is here argued that it is still possible to synthesise Ta_4O_9 . At least five separate studies have reached stoichiometric TaO_2 phases,^{48,49,64,110,127} despite this stoichiometry lying 358 meV/fu (rutile) and 216 meV/fu (K1967) above phase separation into $\text{Ta}_2\text{O}_5 + \text{Ta}$. The Ta_4O_9 phase described here is a form of v_{O} -deficient Ta_2O_5 , and may conceivably be reached by reduction of this phase.

4.2.1 Structural features of Ta_4O_9

Following the finding of the preceding section, the structural features of the metastable Ta_4O_9 phase are examined here. Figure 4.2(a-b) shows the distribution of v_{O} in the supercell for the XY and ZY planes. Two remarkable features are immediately visible, i) vacancies aggregate pair-wise on neighbouring 3f ip sites, and ii) vacancies further aggregate in chains in the out-of-plane direction, forming on the same sites in successive planes. Rather than maximising $v_{\text{O}}-v_{\text{O}}$ distance, vacancies pair together at minimal inter-vacancy distance, and instead maximise the pair-pair distance. Thus, the $v_{\text{O}}-v_{\text{O}}$ distance before relaxation is 2.50 Å within the pairs, with pair-pair distances of 7.21 Å between symmetry-inequivalent v_{O}

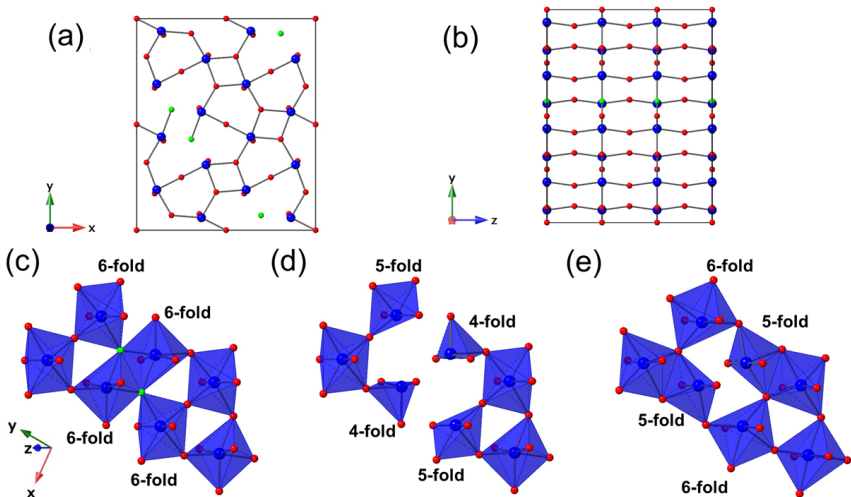


Figure 4.2: (a-b) v_{O} arrangement in Ta_4O_9 prior to relaxation; (a): XY plane view, and (b): ZY plane view. (c-e) polyhedral representation of local environment of v_{O} ; (c): before relaxation, with v_{O} , (d): before relaxation, v_{O} removed, and (e): after relaxation. Blue, red, and green balls represent Ta, O, and v_{O} , respectively.

and 9.69 Å between symmetry-equivalent v_{O} . The latter distance is the maximum possible in-plane $v_{\text{O}}-v_{\text{O}}$ distance of the supercell; i.e., it corresponds to half of the XY plane diagonal:

$$d_{v_{\text{O}}-v_{\text{O}}}^{\text{max}} = 1/2 \left[(12.50 \text{ \AA})^2 + (14.80 \text{ \AA})^2 \right]^{1/2} = 9.69 \text{ \AA}. \quad (4.1)$$

In the out-of-plane direction, the inter-planar distance increases from 3.83 Å to 3.87 Å, a difference of $\sim 1\%$. This is a relatively minor expansion given the high concentration of v_{O} , likely due to the fact that the Ta–O chains in the Z direction are intact.

Figure 4.2(c-e) examines the effect of pair-aggregation on the coordination numbers of neighbouring atoms. Figure 4.2(c) depicts fully sixfold coordinated Ta ions prior to removal of the O pair. The removal of the two neighbouring threefold coordinated O atoms leaves two Ta atoms fivefold coordinated, and another two Ta atoms only fourfold coordinated, as shown by the polyhedra in Figure 4.2(d). Finally, after structural rearrangement of the relaxation process, nearby twofold coordinated O atoms have shifted closer to the under-coordinated Ta atoms, see Figure 4.2(e). As a result, all under-coordinated atoms including the four shifted O atoms raise their coordination numbers by +1. Thus, the pair-defect leaves only two under-coordinated Ta atoms with coordination number 5. The shift of twofold coordinated O atoms due to a vacancy on a threefold coordinated O site is consistent with observations of Jiang and Stewart⁸⁰ and Lee et al.⁶⁰

4.3 Primitive cell of the Ta_4O_9 phase

The regular arrangement of v_{O} -pairs allows the 156-atom supercell ($\text{Ta}_{48}\text{O}_{120-12}$) to be reduced to a primitive cell of just 26 atoms ($\text{Ta}_8\text{O}_{20-2}$). The resultant structure is depicted in Figure 4.3, with Wyckoff positions in Table 4.1. The cell is monoclinic, with spacegroup number 10 (P2/m). The following analysis of this section refers to this cell.

4.3.1 Electronic properties of Ta_4O_9

Having established a primitive cell for Ta_4O_9 , the electronic properties of the structure are now investigated. As described in Section 2.3, PBE is known to underestimate energy

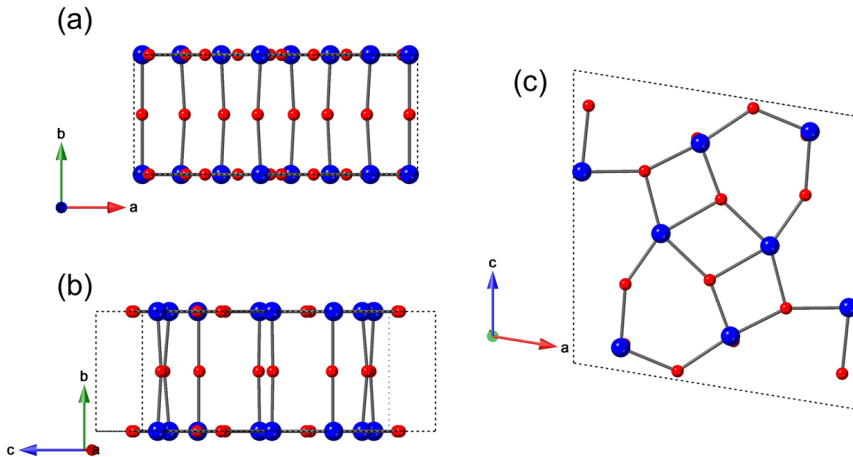


Figure 4.3: Primitive cell of the Ta_4O_9 phase.

Table 4.1: Wyckoff positions for the primitive Ta_4O_9 cell. Lattice parameters are: $|\mathbf{a}| = 9.29 \text{ \AA}$, $|\mathbf{b}| = 3.87 \text{ \AA}$, $|\mathbf{c}| = 9.47 \text{ \AA}$, with angle $\beta = 99.3^\circ$.

Element	u	v	w	Wyckoff
O	0.7493	0.0	0.3052	2m
O	0.9470	0.0	0.1133	2m
O	0.9716	0.5	0.3483	2n
O	0.5200	0.0	0.6410	2m
O	0.6825	0.5	0.5048	2n
O	0.1785	0.5	0.0920	2n
O	0.4362	0.5	0.8360	2n
O	0.3665	0.0	0.0300	2m
O	0.8173	0.0	0.7024	2m
Ta	0.9708	0.0	0.3427	2m
Ta	0.6922	0.0	0.5094	2m
Ta	0.1661	0.0	0.0784	2m
Ta	0.4469	0.0	0.8207	2m

gaps. To obtain a more quantitatively accurate description of the electronic properties, a single-point calculation using HSE has been performed. For this calculation, the k grid was reduced from $(3 \times 6 \times 3)$ to $(2 \times 5 \times 2)$ due to the computational cost of the HSE method. Figure 4.4 presents the HSE-calculated band structure and Projected Density of States (PDOS) spectrum of Ta_4O_9 with energies relative to the Valence Band Maximum (VBM) of Ta_2O_5 . The bandstructure shows that the two v_O in the cell each contribute a defect band in the center of the gap. The PDOS shows that the defect state has primarily Ta d character, secondarily O p, and tertiarily Ta s character, as shown by the inset in Figure 4.4(b). The defect state is filled, with a gap of 1.12 eV up to the conduction band. The conduction and valence band edges are seen to match those of Ta_2O_5 well, with the small discrepancy in valence band edges possibly arising from the reduced k grid employed for Ta_4O_9 .

To better understand the mid-gap states and their remarkable stability, the real-space wave function of the pair defect is calculated at the Γ point and visualised. As was shown in Figure 4.4, the defect states make up the highest-occupied valence band (HVB) and the second-highest-occupied valence band (SHVB). The wave functions associated with these bands are illustrated in Figure 4.5(a-b), while Figure 4.5(c) shows the local coordinate system of a fivefold coordinated Ta atom. The SHVB has primary character of a bonding orbital formed between the two Ta $d_{z^2-r^2}$ orbitals, and secondary character of the surrounding O p_z orbitals. A tertiary character of Ta s is seen from the hybridisation of the equatorial part of the $d_{z^2-r^2}$ orbitals. The HVB has primary character of a bonding orbital between the Ta d_{yz} orbitals, with secondary character in the form of slight hybridisation with the p_y orbitals of 2f oop O atoms. Evidently, the Ta atoms are effectively restored to full sixfold coordination by the bonding arrangement of their respective d orbitals, thus helping to stabilise the pair-defect.

The results of Figure 4.5 may be understood in the following electrostatic interpretation. The removal of the two O^{2-} ions must be compensated by four electrons, which are localised in the void between the neighbouring Ta atoms. This lowers the nominal oxidation state of the two Ta atoms from +5 to +3, and some of their d orbitals are filled as a result. If

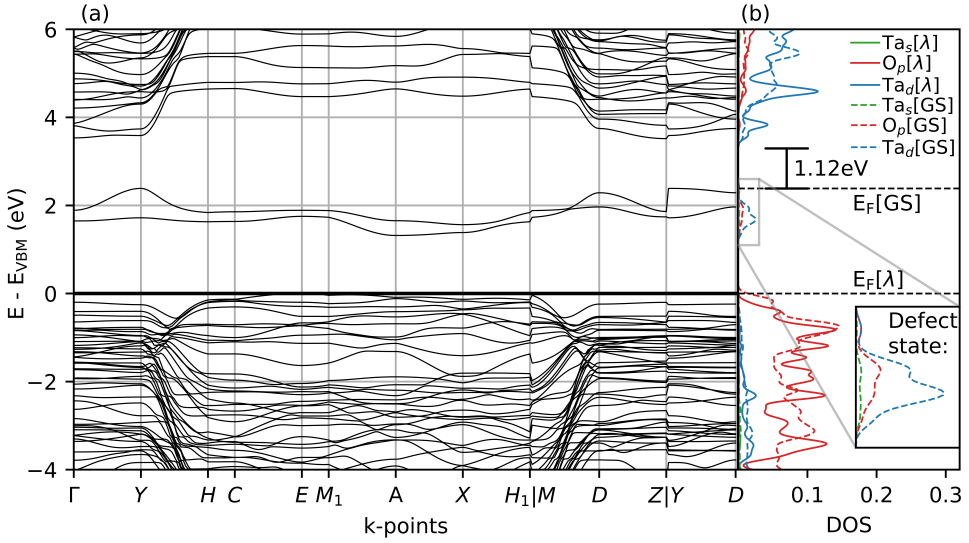


Figure 4.4: Band structure (a) and DOS spectrum (b) of the Ta_4O_9 phase. Legend in (b) refers to λ and Ground State (GS), i.e. Ta_4O_9 . Inset in (b) shows a zoomed-in view of the defect state in the middle of the gap.

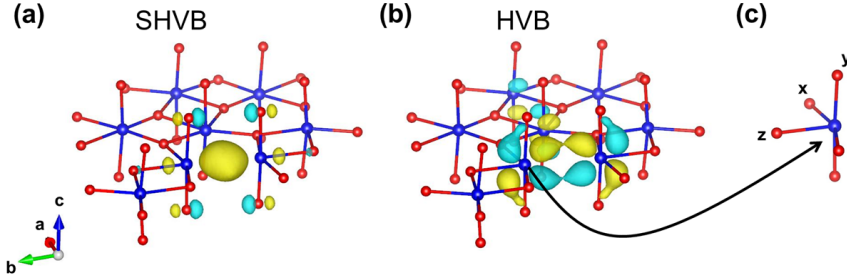


Figure 4.5: Real-space wave functions of the SHVB (a) and HVB (b) at the Γ point. Iso-surface colours refer to opposite signs. (c) depicts the local axis of a fivefold coordinated Ta atom.

the Ta atoms are close enough to one another, these d orbitals may overlap, giving rise to a bonding and antibonding orbital. The actual post-relaxation distance between the Ta^{3+} ions is only 2.94 Å, which is closer to the Ta-Ta distance in elemental BCC Ta (2.84 Å) than the original Ta-Ta distance (3.29 Å) in intrinsic $\lambda\text{-Ta}_2\text{O}_5$.

4.4 Energetics of defect aggregation

The objective of this section is to investigate the energetic favour of the pair defects and their aggregations into chains. To this end, a variety of v_{O} -distributions using different $v_{\text{O}}-v_{\text{O}}$ distances have been calculated. The analysis is limited to the threefold vacancy due to its prevalence in the structures along the hull.

Figure 4.6(c) plots the formation energy per v_{O} calculated for different $v_{\text{O}}-v_{\text{O}}$ distances as determined prior to relaxation. Both concentrations of 5% and 10% v_{O} are shown, the last of which corresponds to the Ta_4O_9 stoichiometry. Figure 4.6(a-b) show the atomic

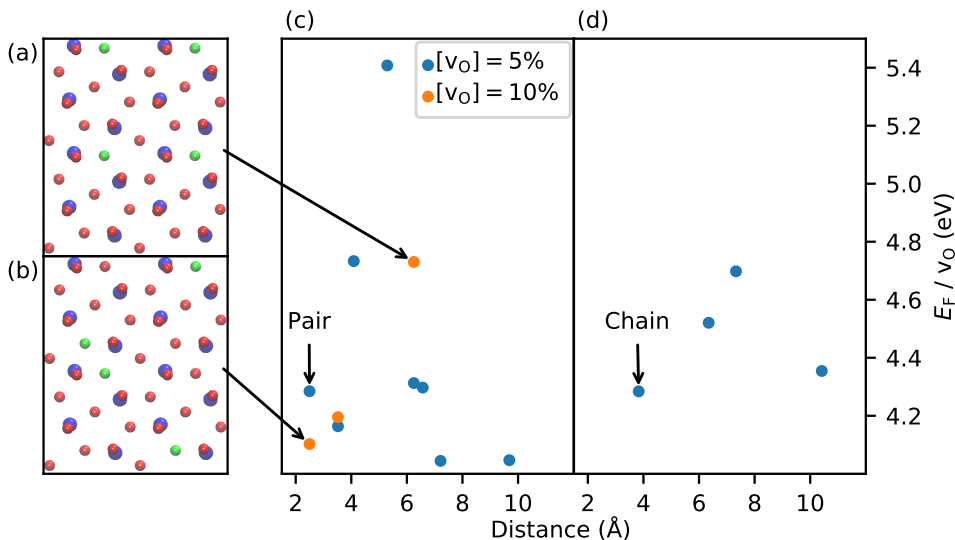


Figure 4.6: (a-b): Atomic structure of non-paired (a) and paired (b) v_{O} distributions at 10% v_{O} concentration. (c) Formation energy per v_{O} as function of $v_{\text{O}}-v_{\text{O}}$ distance for two in-plane v_{O} ($C[v_{\text{O}}] = 5\%$) and for four in-plane v_{O} ($C[v_{\text{O}}] = 10\%$). (d) Same analysis as (c) for out-of-plane v_{O} -pair aggregation performed for $[v_{\text{O}}] = 5\%$. Shortest distances correspond to pairs (c) and chains (d), respectively.

structure associated with minimum and maximum $v_{\text{O}}-v_{\text{O}}$ distances, respectively, at 10% v_{O} concentration. For $[v_{\text{O}}] = 5\%$, separation of v_{O} is clearly favoured. However, short-distance aggregation shows remarkably low energy compared to mid-distance distribution. This provides a quantitative analysis of the effect of the defect wave function, which is here shown to compete with the Coulombic energy gain associated with v_{O} separation. When $[v_{\text{O}}]$ is doubled from 5% to 10%, pair aggregation is favoured for three reasons: i) the mean E_{F} per v_{O} decreases for two pairs as compared to a single pair, ii) the maximal (separated) $v_{\text{O}}-v_{\text{O}}$ distance decreases from 9.69 Å to 6.25 Å due to the greater number of v_{O} , penalising separation, and iii) by pairing together, vacancies can maintain a minimum distance of 7.21 Å between individual pairs – nearly 1 Å greater than for separation into individual v_{O} .

In Figure 4.6(d), a similar analysis is performed for out-of-plane aggregation at $[v_{\text{O}}] = 5\%$ to evaluate the effect of chain formation. Here, the shortest distance is favoured, immediately explaining in terms of energy the chain-like aggregation. The reason may be found in the plane-and-chain atomic structure of orthorhombic Ta₂O₅. Distributing multiple v_{O} on the same lattice sites within successive Ta₂O₃ planes preserves planar equivalence, lowering the total energy in comparison to non-chained configurations.

4.5 Convex hull of crystalline phases

The preceding analysis of this chapter has focused on v_{O} -defective λ -Ta₂O₅. However, as was described in the introduction to the chapter, oxygen-deficiency might also take the form of phase change to structures with lower O content, such as rutile TaO₂. This section presents a structure search among existing metal oxide phases adapted for Ta. The analysis of Sections 3.2 and 3.2.1 suggested that one may consider metal oxide phases of the other

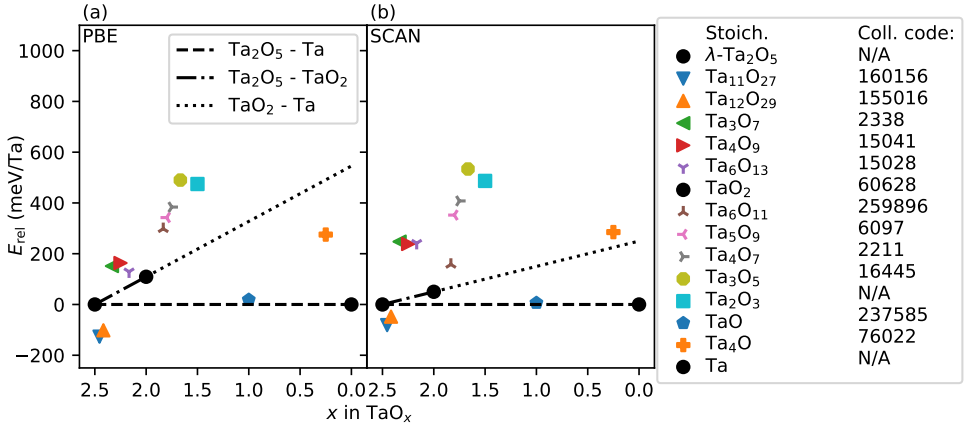


Figure 4.7: Convex hull for various theorised TaO_x phases, calculated with PBE (a) and SCAN (b). Dashed line shows the hull of Ta₂O₅-Ta, dash-dotted line of Ta₂O₅-TaO₂, and dotted line of a theoretical continuation of the Ta₂O₅-TaO₂-hull. Legend shows stoichiometry and ICSD Coll. codes of depicted structures.

Group V metal oxides, i.e. V_xO_y and Nb_xO_y, in the description of tantalum oxide phases. For this reason, the main focus of this structure search is on existing phases of vanadium oxide and niobium oxide.

The results are summarised in Figure 4.7 as calculated with PBE (a) and the SCAN functional (b). The two methods yield visibly different results, but agree on a number of surprising predictions. Remarkably, the two methods agree that the most stable structure is Ta₁₁O₂₇ (template: Nb₂₂O₅₄)¹²⁸ followed by Ta₁₂O₂₉ (template: Nb₁₂O₂₉).¹²⁹ The relative energy of these phases are -127 meV/fu and -101 meV/fu for the PBE functional, and -81 meV/fu and -48 meV/fu for the SCAN functional. In addition, the stoichiometry of TaO (template: NbO)¹³⁰ is metastable with relative energy 19 meV/fu (PBE) and 6 meV/fu (SCAN), which is significantly lower than the relative energy of e.g. rutile TaO₂ (358 meV/fu). The legend in Figure 4.7 provides ICSD Coll. Codes for each structure except Ta₂O₃.

Another feature of Figure 4.7 is that niobium oxides provide much better transferability to tantalum oxide than do vanadium oxides. I.e., the predicted stable or metastable phases (excluding Ta₂O₅ and Ta) use niobium oxide templates, while vanadium oxide templates are found to be unstable upon substitution of Ta. Even in the cases of V₆O₁₃ and V₅O₉, which both exhibit full sixfold coordination, the corresponding tantalum oxides are unstable. The hypothetical continuation of the Ta₂O₅-TaO₂ line provides no lifeline as to the possible existence of the crystalline Ta₆O₁₃ and Ta₅O₉ phases.

Both Nb₁₁O₂₇ and Nb₁₂O₂₉ have a shear structure consisting of corner-sharing “grids” of NbO₆ octahedra.¹²⁸ Further, all Nb atoms are sixfold coordinated in these structures. Cava et al. report on a series of Nb_xO_y shear structures, similar to the Magnéli series for rutile TiO₂.¹³¹ Additionally, the same study describes a reliable method of manufacturing pure Nb_xO_y samples from Nb₂O₅. It is uncertain whether the same method may be used to manufacture Ta₁₁O₂₇ or Ta₁₂O₂₉, due to the dissimilarities between the Nb₂O₅ and Ta₂O₅ structures. As for manufacturing TaO, the method employed by Muraoka et al.¹²⁷ to manufacture TaO₂ from a NbO₂ target seems at first glance to also be applicable to TaO,

since the NbO structure was used as a template for the calculation in Figure 4.7.

The corner-sharing orthorhombic structure of the $\text{Ta}_{11}\text{O}_{27}$ and $\text{Ta}_{12}\text{O}_{29}$ structures result in these phases being conducting. The conductivity is consistent between PBE, SCAN, and HSE (single-point calculation following PBE relaxation; reduced k grid). This compounds the analogy between these shear structures and the Magnéli phases of the TiO_x system, which are also conducting. Further, Fang et al. used first-principles calculations to demonstrate weak ferromagnetism in $\text{Nb}_{12}\text{O}_{29}$.¹³² This result was not reproduced using standard-accuracy PBE calculations for neither $\text{Nb}_{12}\text{O}_{29}$ nor $\text{Ta}_{12}\text{O}_{29}$. However, the aforementioned HSE calculation did find weakly ($\sim 0.01 \mu_{\text{B}}$) magnetised Ta atoms without explicitly searching for a magnetic ground state.

As a closing comment to this chapter, the apparent stability and conductivity of $\text{Ta}_{12}\text{O}_{29}$ and $\text{Ta}_{11}\text{O}_{27}$ suggests, on a theoretical level, that phase-change resistive switching may be possible. On the same theoretical level, switching between e.g. Ta_2O_5 and $\text{Ta}_{12}\text{O}_{29}$ would offer some benefits over e.g. TiO_2 based devices. In order to switch from insulating TiO_2 to conducting Ti_4O_7 , one-eighth of O atoms must be removed. In comparison, switching from e.g. insulating $\text{Ta}_{12}\text{O}_{30}$ (i.e. Ta_2O_5) to conducting $\text{Ta}_{12}\text{O}_{29}$ would require the removal of one in thirty O atoms; a comparatively small amount. However, several significant obstacles lie between theory and practice, the greatest of which is reliably obtaining the conducting shear structure by switching from Ta_2O_5 , which does not have the same atomic structure as Nb_2O_5 .

Chapter 5

DFTB-parametrisation of Ta₂O₅

5.1 Introduction

This chapter presents ongoing work on a DFTB-parametrisation of Ta₂O₅. The reader is advised that the parametrisation procedure is not complete. However, it represents a great research effort, and these preliminary results still show great promise for the possibility of using DFTB to simulate tantalum oxide. The purpose of the parametrisation is to be able to simulate v_O-defective Ta₂O₅ on a larger scale. DFTB has been used successfully for similar purposes before,^{133,134} and has even been used to model dynamical migration of v_O in TiO₂ under an applied electric field.¹³⁵ The implementation of DFTB+ⁱ provides several useful tools for analyzing ReRAM devices,¹³⁶ including support for applied electric fields as well as transport calculations in the Non-Equilibrium Green's Function (NEGF) approach. Before discussing the parametrisation, some choices of input variables will be outlined.

5.1.1 Computational methods

The parametrisation of Ta has the valence configuration 6s²6p⁰5d³, i.e., five valence electrons and one unoccupied “virtual” orbital. Both the density and the orbitals are treated with a power compression to second order. Relativistics are treated with the Zeroth-Order Regular Approximation (ZORA).¹³⁷ The parametrisation of O was taken from the established parameter set known as “mio”,⁹⁶ and is considered static – i.e., no further work on the O parametrisation has been carried out. This project uses the same procedure for parametrisation as outlined in reference 134; briefly:

1. Vary confinement radii until a satisfactory match for the DFT-calculated band structure is reached.
2. Calculate a repulsive potential for the chosen combination of confinement radii.
3. Evaluate key quantities (e.g. lattice parameters and v_O formation energies).
4. Continue until satisfying accuracy is reached.

For the actual DFTB calculations, input parameters have been chosen to match those employed in DFT studies, as much as possible. k point grids match those employed by DFT;

ⁱAvailable from: <https://www.dftbplus.org>

meaning Γ -point for MD equilibrations of 168-atom supercells, $(2 \times 2 \times 3)$ for relaxations of the 168-atom cells, and $(4 \times 4 \times 6)$ for the λ unit cell from which lattice parameters are extracted. All k grids are shifted to the Γ point in directions of even sampling. Electronic smearing was set to 0.1 eV, and the force convergence threshold was set to $0.025 \text{ eV \AA}^{-1}$. Details on the MD structure generation procedure will be provided in the relevant paragraph.

5.2 Parametrisation

Here, the process of parametrising tantalum oxide is described in detail. Although the benchmark parameters are well defined and simple to check, the procedure is by no means trivial. For this reason, various bugs encountered and fixed during the fitting of the repulsive potential will also be presented. The treatment will begin with obtaining the confinement radii described in Section 2.4.3.

5.2.1 Generating the Slater-Koster tables

Arriving at an optimal set of cutoff radii for the valence orbitals is a process of fine-tuning. As described in Section 2.4.3, Koskinen and Mäkinen suggest working from twice the covalent radius of the element one wishes to parametrise. Another option is to use existing parameters of a similar element, if available. Neither approach was pursued in this parametrisation of Ta, except that the density cutoff was set to $9.41 a_0$, which was suggested for Au by Fihey et al.¹³⁸

With this ansatz, batches of pseudo-atom calculations were performed, iteratively varying the orbital cutoffs and the density cutoff, respectively. The best match to DFT-calculated band structure and DOS spectrum was obtained using cutoff radii of $5.00 a_0$ for the s, d, and f orbitals, and $3.80 a_0$ for the p orbitals. The density cutoff radius of $9.41 a_0$ was kept in the final parametrisation.

5.2.2 Fitting the repulsive potential

The CONFITTI code was employed to fit the repulsive potential.ⁱⁱ CONFITTI builds on a machine learning approach, and thus needs training data with which to build a statistical model. To this end, a number of λ -Ta₂O₅ cells subjected to the “rattle” function of ASE were calculated using VASP. Briefly, the atomic coordinates are slightly randomised with respect to the equilibrium, sampling different Ta–O bond lengths resulting in varying total energies which the CONFITTI code can use to reconstruct a repulsive potential. Additionally, the oxygen-deficient structures calculated for the CLEASE-assisted study in Chapter 4 as well as the amorphous structures of Chapter 3 were included. Adding elemental Ta in the BCC phase was attempted, but consistently resulted in worse fit results. Hence, this data was not included in the final model.

A fundamental requirement of the repulsive potential is that it be smooth everywhere. Throughout the course of this project, the version of CONFITTI used was still in the beta phase, and two problems arose which lead to a violation of the smoothness requirement in two different ways, shown in Figure 5.1. Frame (a) shows how small kinks in the energy curve results in huge spikes in the corresponding force curve. This was linked to a bug in the local copy of the CONFITTI code. Note, however, that such a bug can slip by unnoticed if the discontinuities exist at shorter ranges than the bond length in the parametrised material. In the present case, the bug was located during generation of amorphous structures similar

ⁱⁱCONFITTI is a work in progress; for details, contact J. Kullgren at Ångström Laboratory, Uppsala University

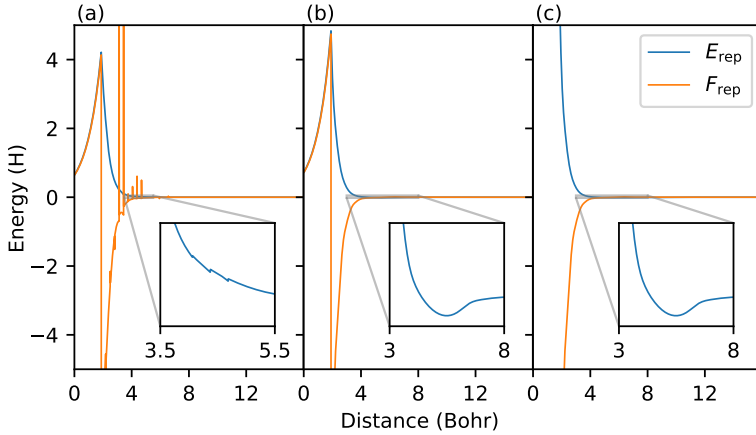


Figure 5.1: Successive iterations of repulsive spline fitting. (a): Spline shows kinks at the knot boundaries (see inset), likely due to a truncation error. (b): Kinks are fixed, but the short-range region shows a discontinuity. (c): Working repulsive potential.

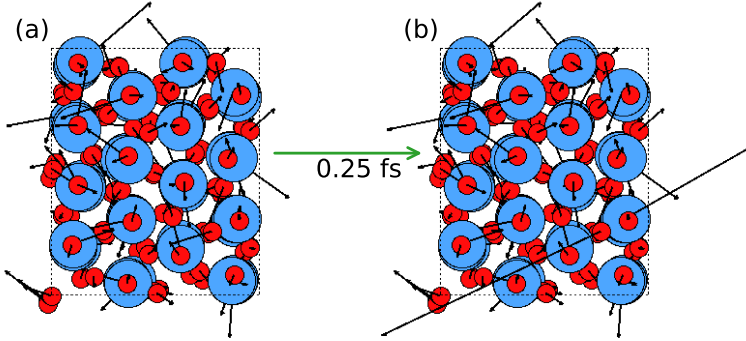


Figure 5.2: (a): Ta_2O_5 cell during NVE run at 2000 K. (b): Same cell, one timestep of 0.25 fs after (a). Black arrows show forces acting on ions.

to the procedure described in Chapter 3. During high-temperature MD runs, Ta and O atoms acquire sufficient energy to move within $\sim 1.7 \text{ \AA}$ of one another, at which distance a particularly high force spike was encountered. This led to sudden high forces between the two offending atoms, see Figure 5.2. These forces resulted in unphysical temperature increases on the order of 10^5 K in the MD simulations.

A similar issue arose for the short-range region, which is modelled with an exponential rather than a spline. In Figure 5.1(a-b), the repulsive energy decreases close to zero, where it should continue to increase. As with the previous issue, this issue was located during high-temperature MD equilibrations. In contrast, Figure 5.1(c) shows the correct spline/exponential behaviour. Since there is no reliable and documented way of obtaining repulsive potentials, users of DFTB are advised to always plot as-generated repulsive potentials to ensure they behave properly.

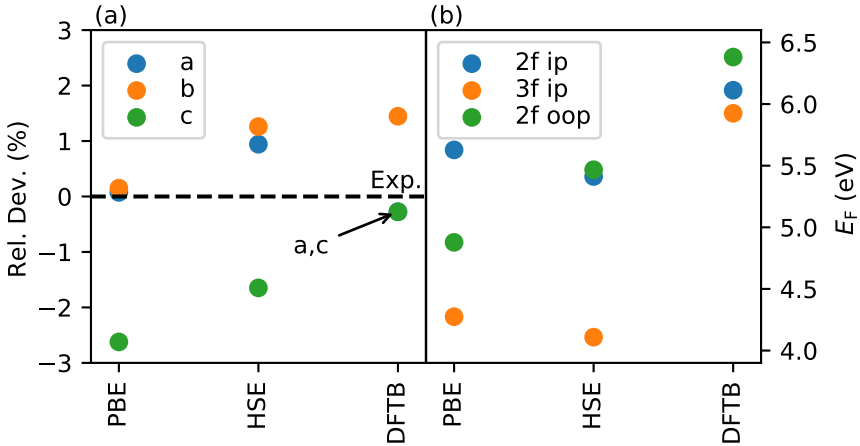


Figure 5.3: (a): Relative deviation from experimental lattice parameters for PBE, HSE, and DFTB. a and c cell parameters coincide for DFTB. (b): Same benchmarking for v_{O} formation energies.

5.3 Benchmarking

The performance of the debugged parametrisation is now evaluated by benchmarking versus PBE and HSE. In Figure 5.3(a), the lattice parameters of the $\lambda\text{-Ta}_2\text{O}_5$ unit cell depicted in Figure 2.3 are calculated using all three methods and compared to experiment. The relative deviations from the experimental lattice parameters described in Section 2.2 for the PBE-calculated cell are: $\Delta a = -0.35\%$, $\Delta b = 1.29\%$, and $\Delta c = 2.41\%$. For HSE, the deviations are $\Delta a = -1.20\%$, $\Delta b = 0.18\%$, and $\Delta c = 1.39\%$. Note that the HSE calculation uses a reduced k grid of $(2 \times 2 \times 6)$ and a cutoff energy of 500 eV instead of 520 eV. Finally, the relative deviations of the DFTB-calculated lattice parameters are $\Delta a = -0.27\%$, $\Delta b = 1.45\%$, and $\Delta c = -0.28\%$.

The comparison to v_{O} formation energies is shown in Figure 5.3(b). The single- v_{O} formation energies were calculated in the 168-atom supercell. The HSE relaxation used only the Γ point. Two notable differences between DFTB and DFT are observed: i) DFTB predicts greater formation energies for all three vacancies than both PBE and HSE, and ii) the formation energies are spaced more closely on the energy axis. However, DFTB achieves a qualitative agreement in that the 3f ip vacancy is predicted to be most stable, by a margin of 0.19 eV. Hence, the 3f ip defect will be favoured in the majority of applications, which will give a qualitative, if not quantitative, description of v_{O} formation.

5.3.1 Amorphous Ta_2O_5

Studies of amorphous TaO_x such as the one presented in Chapter 3, are valuable, but costly. Relatively large system sizes are necessary to model an amorphous system, while several structures must be generated in order to sample the configuration space with any accuracy. The speed increase offered by DFTB is highly desirable for this type of systems, because structures can be rapidly generated and easily transferred to higher accuracy DFT methods if need be. In this section, the procedure of Chapter 3 is emulated using DFTB in order to benchmark the performance of the newly developed parametrisation versus established DFT results.

A few important differences are observed: Although the smoothening of the repulsive

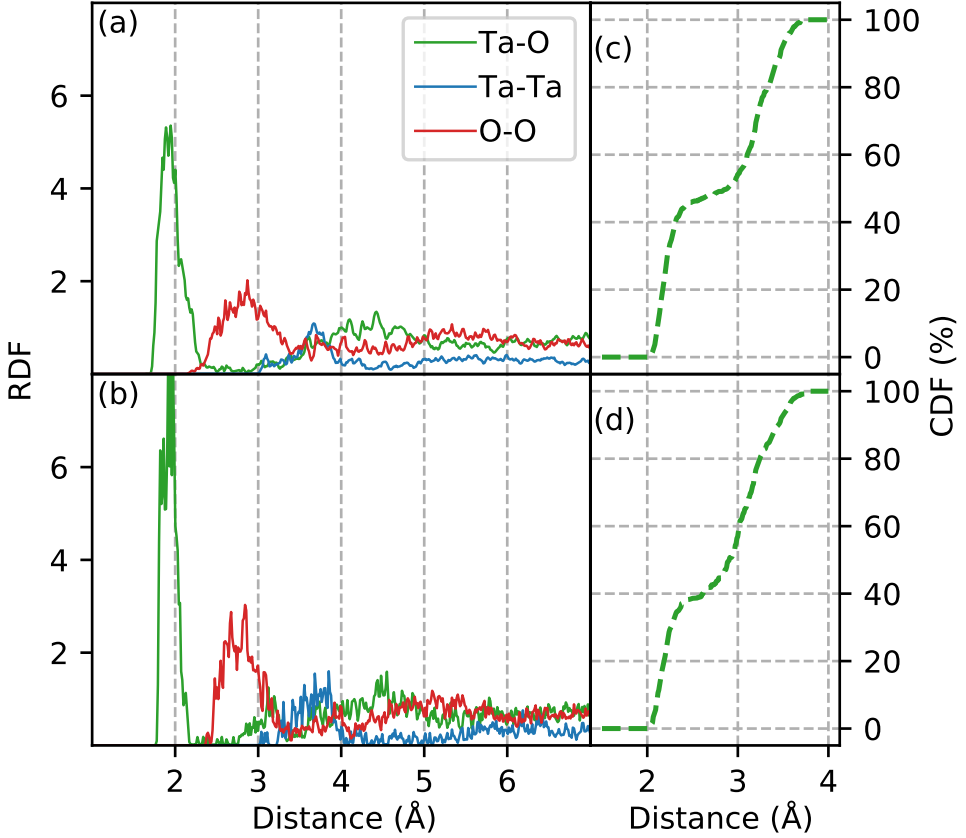


Figure 5.4: (a-b): RDF spectra for a-Ta₂O₅ calculated using DFT (a), and DFTB (b). (c-d): CDF of sixth-nearest O neighbours of Ta atoms calculated using DFT (c), and DFTB (d).

potential described in Section 5.2.2 greatly reduced issues with temperature stability during equilibration, a similar issue persisted when equilibrating at high temperatures. Equilibrations using the Berendsen thermostat¹³⁹ at 5000 K resulted in temperature instability, while the Nosé-Hoover thermostat at 4000 K to 5000 K did the same. (The coupling strength of the Nosé-Hoover thermostat was set to 852 cm s⁻¹, which was the highest calculated phonon mode for λ-Ta₂O₅.) The Berendsen thermostat allowed for stable equilibration at 4000 K; hence this setup was used. The equilibrations used the DFTB-relaxed cell vectors, which were expanded by the same factor as was used for DFT, i.e. 1.06. Since the DFTB-calculated lattice vectors differ from those obtained using DFT, the density during the DFTB MD procedure did not correspond to the amorphous density. However, the primary purpose of the expansion was to provide space for the structure to properly melt, after which a full cell relaxation would be performed. Hence, it was deemed more important to comply with the DFT methodology during MD equilibrations, and let the cell relax to its final volume afterwards.

Figure 5.4(a-b) compare RDF spectra obtained using DFT (a) and DFTB (b). Both spectra are taken from the minimum-energy structure equilibrated at 300 K for 2000 fs (1 fs time step) after relaxation. The curves are averaged over all 2000 time steps. As seen

in the Figure, the DFTB spectrum is noisier, and the primary peaks of O–O and Ta–O are sharper than is seen in the DFT spectra. The central features are in good agreement, although the DFTB equilibration yields a shallow peak in the Ta–O spectrum at $\sim 3.0 \text{ \AA}$ not seen in the DFT-calculated spectrum.

The CDF spectra are compiled using data from all fourteen snapshots and shown in Figure 5.4(c-d). There is good qualitative agreement between the DFT-calculated curve in (c) and the DFTB-calculated curve in (d). The onset of the ascent and subsequent plateau are accurately reproduced by DFTB, although the DFTB-calculated plateau has a height of 39% at 2.5 \AA , while the DFT plateau lies at 46%. This suggests that DFTB captures the same features of short-range atomic order, although not to the same degree as DFT. In conclusion, the DFTB parametrisation performs well for rapid generation of amorphous tantalum pentoxide. In the future, the parametrisation may be improved upon, specifically for improving the description of v_{O} . Further, the parametrisation allows simulating a device with a stoichiometry gradient similar to real devices, which will allow e.g. investigations of conducting nanofilaments and possibly oxygen vacancy drift under an applied electric field.

Chapter 6

Summary and outlook

The three previous chapters have presented investigations into amorphous TaO_x (Chapter 3), crystalline TaO_x (Chapter 4), and a DFTB-parametrisation of tantalum oxide (Chapter 5) for use in studies such as the first two. This chapter summarises the most important findings of this work, and discusses the questions which arise following these findings as well as how future studies may answer said questions.

6.1 Amorphous TaO_x

A large-scale investigation of amorphous TaO_x , $x \in [2.5, 2.0]$, was performed. By sampling several structures of the same stoichiometry, it was possible to meaningfully compare total energies and simulate XPS spectra as well as Bader charge distributions. The study revealed the following:

- Ta_2O_5 and TaO_2 are the most stable stoichiometries in the considered stoichiometry range. However, Ta_6O_{13} was remarkably close to the convex hull, compared to Ta_3O_7 , Ta_4O_9 , and $\text{Ta}_{12}\text{O}_{25}$. The lower total energy of Ta_2O_5 , Ta_6O_{13} , and TaO_2 was related to increased sixfold coordination of Ta atoms in these structures. This was further related to the full sixfold coordination exhibited by crystalline tantalum oxide phases (λ - Ta_2O_5 and rutile TaO_2) as well as crystalline V_6O_{13} .
- The simulated XPS spectrum of a- Ta_2O_5 consisted exclusively of the Ta^{5+} peak, and agreed well with experiment. The simulated XPS spectrum of a- TaO_2 exhibited a strong signal of the Ta^{5+} peak as well as the Ta^{4+} peak, the spacing between which also agreed with experiment.
- The Bader charge analysis of Ta atoms resulted in a sharp peak at Bader charge +3, corresponding to oxidation state +5, for Ta_2O_5 . This peak, although blunted, was also present for Ta_6O_{13} and TaO_2 . For these two stoichiometries, the peak had a smeared-out “tail”, with some Ta atoms in TaO_2 possessing Bader charges below the value calculated for rocksalt TaO .
- A decomposition of the Bader charge and XPS spectra into Gaussians revealed a linear correlation between Bader charge/XPS peak locations.

6.2 Crystalline TaO_x

Analogous to the treatment of amorphous tantalum oxide, a structure search was performed for crystalline TaO_x, also with $x \in [2.5, 2.0]$. Here, oxygen deficiency was modelled by introducing oxygen vacancies in λ -Ta₂O₅, and the minimum-energy structures were found using the machinery of Cluster Expansion. Several conclusions were drawn:

- The configuration of minimum relative energy was found to be Ta₄O₉. This structure was reduced to a monoclinic primitive cell consisting of 28 atoms, and cell parameters as well as Wyckoff positions were presented for the primitive cell.
- A structural analysis of the Ta₄O₉ phase found a unique defect aggregation. Oxygen vacancies formed in pairs on neighbouring threefold coordinated sites in the XY plane, and formed on the same sites in successive planes.
- The two Ta atoms closest to the pair defect site were found to be fully sixfold coordinated, despite initially being left with only four oxygen neighbours after creating the vacancies. Rearrangement of nearby twofold O atoms raised the Ta coordination number to five, while the Ta atoms were close enough to form bonding orbitals between the “dangling” d orbitals, restoring the atoms to full sixfold coordination.
- The pair defect induced states in the middle of the Ta₂O₅ band gap, leaving the band structure otherwise intact. The Ta₄O₉ structure was therefore found to be non-conducting.
- An energetic analysis found the pair defect to be unstable at 5% oxygen vacancy concentration, and stable at 10%, the latter corresponding to Ta₄O₉.
- The investigation of crystalline TaO_x based on Group V metal oxides shows Ta₁₁O₂₇ and Ta₁₂O₂₉ to be stable, and TaO to be metastable. All three phases used NbO_x structures as templates with Ta substituted for Nb.

6.3 Parametrisation of TaO_x for DFTB

The third and final part of this work described the ongoing work on development and testing of a parametrisation of tantalum oxide for Density Functional Tight-Binding. The performance of the parametrisation was evaluated with respect to lattice parameters and v_O formation energies after documenting and removing two bugs found during fitting of the repulsive spline.

- A parametrisation was developed for Ta, with the specific purpose of large-scale simulation of tantalum oxides.
- The parametrisation performed well for calculation of λ -Ta₂O₅ lattice parameters, compared to experiment, PBE and HSE. For v_O formation energies, it yielded qualitative, but not quantitative agreement.
- RDF and CDF spectra of DFTB-generated a-Ta₂O₅ agreed well with those obtained using DFT, though the CDF spectrum showed lower sixfold coordination as compared to the DFT-obtained spectrum.

6.4 Outlook

The above findings and their role in the body of research are discussed now. Several possibilities for future work have arisen throughout the preparation of this thesis:

- The theorised stable and metastable phases of amorphous and crystalline TaO_x calls for experimental studies to demonstrate them. Some possible methods are:
 - $\text{a-Ta}_6\text{O}_{13}$ may be reached by stoichiometry-controlled growth of a-TaO_x followed by thermal annealing.
 - Crystalline Ta_4O_9 may be synthesised either through reduction of orthorhombic Ta_2O_5 , or possibly by oxidation of elemental Ta.
 - TaO in the NbO structure may be synthesised by e.g. Pulsed-Laser Deposition working on a NbO template.
 - $\text{Ta}_{11}\text{O}_{27}$ and $\text{Ta}_{12}\text{O}_{29}$ will likely require the synthesis of Ta_2O_5 working on a Nb_2O_5 template, followed by the procedure used to generate the $\text{Nb}_{11}\text{O}_{27}$ and $\text{Nb}_{12}\text{O}_{29}$ structures from Nb_2O_5 .
- The hypothesised $\text{a-Ta}_6\text{O}_{13}$ phase, as well as the link to crystalline Group V metals, suggests that more metastable phases may exist in the a-TaO_x system. The computational method employed in this thesis can be extended to lower oxygen contents to search for these.
- The finding that the degree of sixfold coordination in crystalline phases is reproduced in amorphous phases of equivalent stoichiometry is worth studying in terms of generality; both for a-TaO_x and for other metal oxides. The method developed here can be readily extended to other materials to document preference for stoichiometricity.
- The simulated XPS spectra of a-TaO_x suggest that the conventional mapping of oxidation states to stoichiometries may be imprecise. Interpretation of XPS spectra of amorphous materials should be done with care.
- The pair defect which characterises the Ta_4O_9 phase may exist in reduced crystalline TaO_x , such as crystallites in ReRAM device layers and TaO_x -electrocatalysts. In both cases, the effects on device function should be investigated.
- If conducting phases of $\text{Ta}_{11}\text{O}_{27}$ and $\text{Ta}_{12}\text{O}_{29}$ can be demonstrated experimentally, their synthesis could pave the way for resistive switching devices with an absolute minimal requirement of oxygen vacancy formation. If they cannot be synthesised, it seems important to study the reason for their alleged stability in order to understand the discrepancy.
- The generation of Slater-Koster tables and repulsive potentials for Ta–Ta and Ta–O allows for greater efficiency and system sizes in studies of tantalum oxide. In particular, devices of realistic size may be simulated incorporating the stoichiometry gradient characteristic of real TaO_x devices.

Bibliography

- [1] F. Masuoka, M. Momodomi, Y. Iwata, and R. Shirota. New ultra high density EPROM and flash EEPROM with NAND structure cell. In *1987 International Electron Devices Meeting*, pages 552–555. IEEE, 1987.
- [2] S. S. P. Parkin, M. Hayashi, and L. Thomas. Magnetic domain-wall racetrack memory. *Science*, 320(5873):190–194, 2008. doi: 10.1126/science.1145799.
- [3] A. Pohm, C. Sie, R. Uttecht, V. Kao, and O. Agrawal. Chalcogenide glass bistable resistivity (ovonic) memories. *IEEE Transactions on Magnetics*, 6(3):592–592, 1970.
- [4] P. J. Wessely and U. Schwalke. Transfer-free grown bilayer graphene memory devices. In *2013 8th International Conference on Design Technology of Integrated Systems in Nanoscale Era (DTIS)*, pages 12–15. IEEE Computer Society, 2013.
- [5] W. W. Zhuang, W. Pan, B. D. Ulrich, J. J. Lee, L. Stecker, A. Burmaster, D. R. Evans, S. T. Hsu, M. Tajiri, A. Shimaoka, K. Inoue, T. Naka, N. Awaya, A. Sakiyama, Y. Wang, S. Q. Liu, N. J. Wu, and A. Ignatiev. Novel colossal magnetoresistive thin film nonvolatile resistance random access memory (RRAM). In *Digest. International Electron Devices Meeting*, pages 193–196. IEEE, 2002. doi: 10.1109/IEDM.2002.1175811.
- [6] T. W. Hickmott. Low-frequency negative resistance in thin anodic oxide films. *Journal of Applied Physics*, 33(9):2669, 1962. doi: 10.1063/1.1702530.
- [7] N. M. Bashara and P. H. Nielsen. Memory effects in thin film negative resistance structures. In *Annual Report 1963 Conference on Electrical Insulation*, pages 29–32. Institute of Electrical and Electronics Engineers Inc, 1963. doi: 10.1109/EIC.1963.7466544.
- [8] M. N. Kozicki, M. Yun, L. Hilt, and A. Singh. Applications of programmable resistance changes in metal-doped chalcogenides. In *Solid-state Ionic Devices*, volume 99, pages 298–309. The Electrochemical Society, 1998.
- [9] A. Beck, J. G. Bednorz, Ch. Gerber, C. Rossel, and D. Widmer. Reproducible switching effect in thin oxide films for memory applications. *Applied Physics Letters*, 77(1): 139–141, 2000. doi: 10.1063/1.126902.
- [10] Y. Watanabe, J. G. Bednorz, A. Bietsch, Ch. Gerber, D. Widmer, A. Beck, and S. J. Wind. Current-driven insulator–conductor transition and nonvolatile memory in chromium-doped SrTiO₃ single crystals. *Applied Physics Letters*, 78(23):3738–3740, 2001. doi: 10.1063/1.1377617.

- [11] I. G. Baek, M. S. Lee, S. Seo, M. J. Lee, D. H. Seo, D.-S. Suh, J. C. Park, S. O. Park, H. S. Kim, I. K. Yoo, U-I. Chung, and J. T. Moon. Highly scalable nonvolatile resistive memory using simple binary oxide driven by asymmetric unipolar voltage pulses. In *IEDM Technical Digest. IEEE International Electron Devices Meeting, 2004.*, pages 587–590. IEEE, 2004.
- [12] J. J. Yang, D. B. Strukov, and D. R. Stewart. Memristive devices for computing. *Nature Nanotechnology*, 8(1):13–24, 2012. doi: 10.1038/nnano.2012.240.
- [13] A. Chen, S. Haddad, Y.-C. Wu, T.-N. Fang, Z. Lan, S. Avanzino, S. Pangrle, M. Buynoski, M. Rathor, W. Cai, N. Tripsas, C. Bill, M. Van Buskirk, and M. Taguchi. Non-volatile resistive switching for advanced memory applications. In *IEEE International Electron Devices Meeting, 2005. IEDM Technical Digest.*, pages 746–749. IEEE, 2005.
- [14] H. Sim, D. Choi, D. Lee, M. Hasan, C. B. Samantaray, and H. Hwang. Reproducible resistance switching characteristics of pulsed laser-deposited polycrystalline Nb₂O₅. *Microelectronic Engineering*, 80:260–263, 2005. doi: 10.1016/j.mee.2005.04.012. 14th biennial Conference on Insulating Films on Semiconductors.
- [15] S. Muraoka, K. Osano, Y. Kanzawa, S. Mitani, S. Fujii, K. Katayama, Y. Katoh, Z. Wei, T. Mikawa, K. Arita, Y. Kawashima, R. Azuma, K. Kawai, K. Shimakawa, A. Odagawa, and T. Takagi. Fast switching and long retention Fe–O ReRAM and its switching mechanism. In *2007 IEEE International Electron Devices Meeting*, pages 779–782. IEEE, 2007. doi: 10.1109/IEDM.2007.4419063.
- [16] H. Shima, F. Takano, H. Muramatsu, H. Akinaga, Y. Tamai, I. H. Inque, and H. Takagi. Voltage polarity dependent low-power and high-speed resistance switching in CoO resistance random access memory with Ta electrode. *Applied Physics Letters*, 93(11):113504, 2008. doi: 10.1063/1.2982426.
- [17] Z. Wei, Y. Kanzawa, K. Arita, Y. Katoh, K. Kawai, S. Muraoka, S. Mitani, S. Fujii, K. Katayama, M. Iijima, T. Mikawa, T. Ninomiya, R. Miyanaga, Y. Kawashima, K. Tsuji, A. Himeno, T. Okada, R. Azuma, K. Shimakawa, H. Sugaya, T. Takagi, R. Yasuhara, K. Horiba, H. Kumigashira, and M. Oshima. Highly reliable TaO_x ReRAM and direct evidence of redox reaction mechanism. In *2008 IEEE International Electron Devices Meeting*, pages 1–4. IEEE, 2008.
- [18] H. Y. Lee, P. S. Chen, T. Y. Wu, Y. S. Chen, C. C. Wang, P. J. Tzeng, C. H. Lin, F. Chen, C. H. Lien, and M.-J. Tsai. Low power and high speed bipolar switching with a thin reactive Ti buffer layer in robust HfO₂ based RRAM. In *2008 IEEE International Electron Devices Meeting*, pages 1–4. IEEE, 2008.
- [19] D. B. Strukov, G. S. Snider, D. R. Stewart, and R. S. Williams. The missing memristor found. *Nature*, 453(7191):80–83, 2008. doi: 10.1038/nature06932.
- [20] J. P. Strachan, A. C. Torrezan, F. Miao, M. D. Pickett, J. J. Yang, W. Yi, G. Medeiros Ribeiro, and R. S. Williams. State dynamics and modeling of tantalum oxide memristors. *IEEE Transactions on Electron Devices*, 60(7):2194–2202, 2013.

- [21] P. W. C. Ho, F. O. Hatem, H. A. F. Almurib, and T. N. Kumar. Comparison on TiO_2 and TaO_2 based bipolar resistive switching devices. In *2014 2nd International Conference on Electronic Design*, pages 249–254. IEEE, 2014.
- [22] J. H. Hur, M.-J. Lee, C. B. Lee, Y.-B. Kim, and C.-J. Kim. Modeling for bipolar resistive memory switching in transition-metal oxides. *Physical Review B*, 82:155321, Oct 2010. doi: 10.1103/PhysRevB.82.155321.
- [23] J. J. Yang, M. X. Zhang, J. P. Strachan, F. Miao, M. D. Pickett, R. D. Kelley, G. Medeiros Ribeiro, and R. S. Williams. High switching endurance in TaO_x memristive devices. *Applied Physics Letters*, 97(23):6–9, 2010. doi: 10.1063/1.3524521.
- [24] L. Zhang, R. Huang, M. Zhu, S. Qin, Y. Kuang, D. Gao, C. Shi, and Y. Wang. Unipolar TaO_x -based resistive change memory realized with electrode engineering. *IEEE Electron Device Letters*, 31(9):966–968, 2010. doi: 10.1109/LED.2010.2052091.
- [25] M.-J. Lee, C. B. Lee, D. Lee, R. L. Seung, M. Chang, J. H. Hur, Y.-B. Kim, C.-J. Kim, D. H. Seo, S. Seo, U-I. Chung, I.-K. Yoo, and K. Kim. A fast, high-endurance and scalable non-volatile memory device made from asymmetric $\text{Ta}_2\text{O}_{5-x}/\text{TaO}_{2-x}$ bilayer structures. *Nature materials*, 10:625–630, 2011. doi: 10.1038/nmat3070.
- [26] H. K. Yoo, S. B. Lee, J. S. Lee, S. H. Chang, M. J. Yoon, Y. S. Kim, B. S. Kang, M.-J. Lee, C. J. Kim, B. Kahng, and T. W. Noh. Conversion from unipolar to bipolar resistance switching by inserting Ta_2O_5 layer in Pt/ TaO_x /Pt cells. *Applied Physics Letters*, 98(18):183507, 2011. doi: 10.1063/1.3587809.
- [27] S. R. Lee, Y. Kim, M. Chang, K. M. Kim, C. B. Lee, J. H. Hur, G. Park, D. Lee, M. Lee, C. J. Kim, U-I. Chung, I. Yoo, and K. Kim. Multi-level switching of triple-layered TaO_x RRAM with excellent reliability for storage class memory. In *2012 Symposium on VLSI Technology (VLSIT)*, pages 71–72. IEEE, 2012. doi: 10.1109/VLSIT.2012.6242466.
- [28] F. Miao, W. Yi, I. Goldfarb, J. J. Yang, M.-X. Zhang, M. D. Pickett, J. P. Strachan, G. Medeiros Ribeiro, and R. S. Williams. Continuous electrical tuning of the chemical composition of TaO_x -based memristors. *ACS Nano*, 6(3):2312–2318, 2012. doi: 10.1021/nn2044577.
- [29] Y. Yang, S. Choi, and W. Lu. Oxide heterostructure resistive memory. *Nano Letters*, 13(6):2908–2915, 2013. doi: 10.1021/nl401287w. PMID: 23724783.
- [30] C. Joseph, P. Bourson, and M. D. Fontana. Amorphous to crystalline transformation in Ta_2O_5 studied by raman spectroscopy. *Journal of Raman Spectroscopy*, 43(8):1146–1150, 2012. doi: 10.1002/jrs.3142.
- [31] Y. Li, S. Sanna, K. Norrman, D. V. Christensen, C. S. Pedersen, J. M. García Lastra, M. L. Traulsen, V. Esposito, and N. Pryds. Tuning the stoichiometry and electrical properties of tantalum oxide thin films. *Applied Surface Science*, 470:1071–1074, 2019. doi: 10.1016/j.apsusc.2018.11.153.
- [32] Y. Ma, J. M. Goodwill, D. Li, D. A. Cullen, J. D. Poplawsky, K. L. More, J. A. Bain, and M. Skowronski. Stable metallic enrichment in conductive filaments in TaO_x -based resistive switches arising from competing diffusive fluxes. *Advanced Electronic Materials*, 5(7):1–8, 2019. doi: 10.1002/aelm.201800954.

- [33] L. Chua. Memristor – the missing circuit element. *IEEE Transactions on Circuit Theory*, 18(5):507–519, Sep. 1971. doi: 10.1109/TCT.1971.1083337.
- [34] R. Waser, R. Dittmann, C. Staikov, and K. Szot. Redox-based resistive switching memories nanoionic mechanisms, prospects, and challenges. *Advanced Materials*, 21(25-26):2632–2663, 2009. doi: 10.1002/adma.200900375.
- [35] Y. Dong, G. Yu, M. C. McAlpine, W. Lu, and C. M. Lieber. Si/a-Si core/shell nanowires as nonvolatile crossbar switches. *Nano Letters*, 8(2):386–391, 2008. doi: 10.1021/nl073224p.
- [36] C. Yoshida, K. Kinoshita, T. Yamasaki, and Y. Sugiyama. Direct observation of oxygen movement during resistance switching in NiO/Pt film. *Applied Physics Letters*, 93(4):042106, 2008. doi: 10.1063/1.2966141.
- [37] D.-H. Kwon, K. M. Kim, J. H. Jang, J. M. Jeon, M. H. Lee, G. H. Kim, X.-S. Li, G.-S. Park, B. Lee, S. Han, M. Kim, and C. S. Hwang. Atomic structure of conducting nanofilaments in TiO₂ resistive switching memory. *Nature nanotechnology*, 5(2):148–153, 2010. doi: 10.1038/nnano.2009.456.
- [38] G.-S. Park, Y. B. Kim, S. Y. Park, X. S. Li, S. Heo, M.-J. Lee, M. Chang, J. H. Kwon, M. Kim, U.-I. Chung, R. Dittmann, R. Waser, and K. Kim. In situ observation of filamentary conducting channels in an asymmetric Ta₂O_{5-x}/TaO_{2-x} bilayer structure. *Nature Communications*, 4:1–9, 2013. doi: 10.1038/ncomms3382.
- [39] G. Bersuker, D. C. Gilmer, D. Veksler, J. Yum, H. Park, S. Lian, L. Vandelli, A. Padovani, L. Larcher, K. McKenna, A. Shluger, V. Iglesias, M. Porti, M. Nafría, W. Taylor, P. D. Kirsch, and R. Jammy. Metal oxide RRAM switching mechanism based on conductive filament microscopic properties. In *2010 International Electron Devices Meeting*, pages 19.6.1–19.6.4. IEEE, 2010. doi: 10.1109/IEDM.2010.5703394.
- [40] J. P. Strachan, J. J. Yang, R. Münstermann, A. Scholl, G. Medeiros Ribeiro, D. R. Stewart, and R. S. Williams. Structural and chemical characterization of TiO₂ memristive devices by spatially-resolved NEXAFS. *Nanotechnology*, 20(48), 2009. doi: 10.1088/0957-4484/20/48/485701.
- [41] J. P. Strachan, M. D. Pickett, J. J. Yang, S. Aloni, A. L. D. Kilcoyne, G. Medeiros Ribeiro, and R. S. Williams. Direct identification of the conducting channels in a functioning memristive device. *Advanced Materials*, 22(32):3573–3577, 2010. doi: 10.1002/adma.201000186.
- [42] J. P. Strachan, D. B. Strukov, J. Borghetti, J. J. Yang, G. Medeiros Ribeiro, and R. S. Williams. The switching location of a bipolar memristor: chemical, thermal and structural mapping. *Nanotechnology*, 22(25):254015, May 2011. doi: 10.1088/0957-4484/22/25/254015.
- [43] S. H. Chang, S. C. Chae, S. B. Lee, C. Liu, T. W. Noh, J. S. Lee, B. Kahng, J. H. Jang, M. Y. Kim, D.-W. Kim, and C. U. Jung. Effects of heat dissipation on unipolar resistance switching in Pt/NiO/Pt capacitors. *Applied Physics Letters*, 92(18):183507, 2008. doi: 10.1063/1.2924304.

- [44] W. Jiang, R. J. Kamaladasa, Y. M. Lu, A. Vicari, R. Berechman, P. A. Salvador, J. A. Bain, Y. N. Picard, and M. Skowronski. Local heating-induced plastic deformation in resistive switching devices. *Journal of Applied Physics*, 110(5):054514, 2011. doi: 10.1063/1.3633271.
- [45] S. Clima, Y. Y. Chen, A. Fantini, L. Goux, R. Degraeve, B. Govoreanu, G. Pourtois, and M. Jurczak. Intrinsic tailing of resistive states distributions in amorphous HfO_x and TaO_x based resistive random access memories. *IEEE Electron Device Letters*, 36(8):769–771, 2015.
- [46] U. Chand, K. Huang, C. Huang, and T. Tseng. Mechanism of nonlinear switching in HfO_2 -based crossbar RRAM with inserting large bandgap tunneling barrier layer. *IEEE Transactions on Electron Devices*, 62(11):3665–3670, 2015.
- [47] R. Hermann. Untersuchungen über die Verbindungen des Tantals. *Journal für Praktische Chemie*, 5(1):66–93, 1872. doi: 10.1002/prac.18720050107.
- [48] J. Niebuhr. Die niederen Oxide des Tantals. *Journal of the Less-Common Metals*, 10: 312–322, 1966. doi: 10.1016/0022-5088(66)90131-7.
- [49] N. Terao. Structure des oxides de tantale. *Japanese Journal of Applied Physics*, 6(1): 21–34, Jan 1967. doi: 10.1143/jjap.6.21.
- [50] A. G. Revesz, J. H. Reynolds, and J. F. Allison. Optical properties of tantalum oxide films on silicon. *Journal of The Electrochemical Society*, 123(6):889–894, dec 1976. doi: 10.1149/1.2132963.
- [51] P. A. Murawala, M. Sawai, T. Tatsuta, O. Tsuji, S. Fujita, and S. Fujita. Structural and electrical properties of Ta_2O_5 grown by the plasma-enhanced liquid source CVD using penta ethoxy tantalum source. *Japanese Journal of Applied Physics*, 32(Part 1, No. 1B):368–375, jan 1993. doi: 10.1143/jjap.32.368.
- [52] S. Uthanna, S. V. J. Chandra, G. M. Rao, and J. F. Pierson. Influence of substrate temperature on the structural, dielectric and optical properties of RF magnetron sputtered Ta_2O_5 films. In *IOP Conference Series: Materials Science and Engineering*, volume 8, page 012025. IOP Publishing, Feb 2010. doi: 10.1088/1757-899x/8/1/012025.
- [53] W. H. Knausenberger and R. N. Tauber. Selected properties of pyrolytic Ta_2O_5 films. *Journal of The Electrochemical Society*, 120(7):927, 1973. doi: 10.1149/1.2403602.
- [54] K. Lehovc. Lattice structure of $\beta\text{-Ta}_2\text{O}_5$. *Journal of the Less Common Metals*, 7(6): 397–410, 1964. doi: 10.1016/0022-5088(64)90036-0.
- [55] P.-H. Chang and H.-Y. Liu. Structures of tantalum pentoxide thin films formed by reactive sputtering of Ta metal. *Thin Solid Films*, 258:56–63, 1995. doi: 10.1016/0040-6090(94)06402-4.
- [56] D. A. Neamen. *Semiconductor Physics and Devices*. McGraw-Hill, 4th edition, 2012.
- [57] J. H. Thomas. Photoconductivity in anodic Ta_2O_5 formed on nitrogen-doped tantalum films. *Journal of Applied Physics*, 45(12):5349–5355, 1974. doi: 10.1063/1.1663241.

- [58] R. M. Fleming, D. V. Lang, C. D.W. Jones, M. L. Steigerwald, D. W. Murphy, G. B. Alers, Y. H. Wong, R. B. Van Dover, J. R. Kwo, and A. M. Sergent. Defect dominated charge transport in amorphous Ta₂O₅ thin films. *Journal of Applied Physics*, 88(2): 850–862, 2000. doi: 10.1063/1.373747.
- [59] G. A. N. Connell. *Amorphous Semiconductors*, chapter 4, pages 71–111. Springer, 1979.
- [60] S.-H. Lee, J. Kim, S.-J. Kim, S. Kim, and G.-S. Park. Hidden structural order in orthorhombic Ta₂O₅. *Physical Review Letters*, 110:235502, 06 2013. doi: 10.1103/PhysRevLett.110.235502.
- [61] Y. Guo and J. Robertson. Comparison of oxygen vacancy defects in crystalline and amorphous Ta₂O₅. *Microelectronic Engineering*, 147:254–259, 2015. doi: 10.1016/j.mee.2015.04.065.
- [62] W. G. Burgers, A. Claassen, and J. Zernike. Über die chemische Natur der Oxydschichten, welche sich bei anodischer Polarisation auf den Metallen Aluminium, Zirkon, Titan und Tantal bilden. *Zeitschrift für Physik*, 74:593–603, 1932. doi: 10.1007/BF01342100.
- [63] S. Lagergren and A Magnéli. On the tantalum–oxygen system. *Acta Chemica Scandinavica*, 6:444–446, 1952. doi: 10.3891/acta.chem.scand.06-0444.
- [64] N. Schönberg. An x-ray investigation of the tantalum-oxygen system. *Acta Chemica Scandinavica*, 8:240–245, 1954. doi: 10.3891/acta.chem.scand.08-0240.
- [65] W. T. Holser. Compounds with the α -U₃O₈-type structure. *Acta Crystallographica*, 9(2):196, Feb 1956. doi: 10.1107/S0365110X56000486.
- [66] P. Kofstad. Studies of the oxidation of tantalum at 1000°–1300 °C. *Journal of the Less Common Metals*, 5(2):158–170, 1963. doi: 10.1016/0022-5088(63)90009-2.
- [67] J. Spyridelis, P. Delavignette, and S. Amelinckx. On the superstructures of Ta₂O₅ and Nb₂O₅. *Physica Status Solidi (b)*, 19(2):683–704, 1967. doi: 10.1002/pssb.19670190220.
- [68] R. B. Hahn. Phosphates of niobium and tantalum. *Journal of the American Chemical Society*, 73(11):5091–5093, 1951. doi: 10.1021/ja01155a022.
- [69] D. A. Vermilyea. The kinetics of formation and structure of anodic oxide films on tantalum. *Acta Metallurgica*, 1(3):282–294, 1953. doi: 10.1016/0001-6160(53)90101-1.
- [70] L. K. Frevel and H. W. Rinn. Powder diffraction standards for niobium pentoxide and tantalum pentoxide. *Analytical Chemistry*, 27(8):1329–1330, 1955. doi: 10.1021/ac60104a035.
- [71] B. King, J. Schultz, E. Durbin, and W. Duckworth. Some properties of tantalum systems. *Report BMI-1106*, 01 1956.
- [72] J. Harvey and H. Wilman. The crystallisation of thin amorphous tantalum oxide films heated in air or vacuo, and the structure of the crystalline oxide. *Acta Crystallographica*, 14(12):1278–1281, Dec 1961. doi: 10.1107/S0365110X61003703.

- [73] L. D. Calvert and P. H. G. Draper. A proposed structure for annealed anodic oxide films of tantalum. *Canadian Journal of Chemistry*, 40(10):1943–1950, 1962. doi: 10.1139/v62-298.
- [74] N. C. Stephenson and R. S. Roth. Structural systematics in the binary system $\text{Ta}_2\text{O}_5\text{--}\text{WO}_3$. V. the structure of the low-temperature form of tantalum oxide L- Ta_2O_5 . *Acta Crystallographica Section B*, 27(5):1037–1044, 1971. doi: 10.1107/S056774087100342X.
- [75] L. A. Aleshina and S. V. Loginova. Rietveld analysis of x-ray diffraction pattern from $\beta\text{-Ta}_2\text{O}_5$ oxide. *Crystallography Reports*, 47(3):415–419, 2002. doi: 10.1134/1.1481927.
- [76] I. E. Grey, W. G. Mumme, and R. S. Roth. The crystal chemistry of L- Ta_2O_5 and related structures. *Journal of Solid State Chemistry*, 178(11):3308–3314, 2005. doi: 10.1016/j.jssc.2005.08.011.
- [77] R. Elson, S. Fried, P. Sellers, and W. H. Zachariasen. The tetravalent and pentavalent states of protactinium. *Journal of the American Chemical Society*, 72(12):5791–5791, 1950. doi: 10.1021/ja01168a547.
- [78] W. Andreoni and C. A. Pignedoli. Ta_2O_5 polymorphs: Structural motifs and dielectric constant from first principles. *Applied Physics Letters*, 96(6):062901, 2010. doi: 10.1063/1.3308475.
- [79] A. S. Pavlovic. Some dielectric properties of tantalum pentoxide. *The Journal of Chemical Physics*, 40(4):951–956, 1964. doi: 10.1063/1.1725287.
- [80] H. Jiang and D. A. Stewart. Enhanced oxygen vacancy diffusion in Ta_2O_5 resistive memory devices due to infinitely adaptive crystal structure. *Journal of Applied Physics*, 119(13):2–7, 2016. doi: 10.1063/1.4945579.
- [81] P. Kofstad. On the defect structure of Ta_2O_5 . *Journal of The Electrochemical Society*, 109(9):776, 1962. doi: 10.1149/1.2425554.
- [82] A. Reisman, F. Holtzberg, M. Berkenblit, and M. Berry. Reactions of the group VB pentoxides with alkali oxides and carbonates. III. Thermal and x-ray phase diagrams of the system K_2O or K_2CO_3 with Ta_2O_5 . *Journal of the American Chemical Society*, 78(18):4514–4520, 1956. doi: 10.1021/ja01599a003.
- [83] J. Kohanoff. *Electronic structure calculations for solids and molecules*. Cambridge University Press, 1st edition, 2006.
- [84] P. Hohenberg and W. Kohn. Inhomogeneous electron gas. *Physical Review*, 136: B864–B871, Nov 1964. doi: 10.1103/PhysRev.136.B864.
- [85] W. Kohn and L. J. Sham. Self-consistent equations including exchange and correlation effects. *Physical Review*, 140:A1133–A1138, Nov 1965. doi: 10.1103/PhysRev.140.A1133.
- [86] J. P. Perdew, K. Burke, and M. Ernzerhof. Generalized gradient approximation made simple. *Physical Review Letters*, 77(18):3865–3868, Oct 1996. doi: 10.1103/PhysRevLett.77.3865.

- [87] M. Kuisma, J. Ojanen, J. Enkovaara, and T. T. Rantala. Kohn-sham potential with discontinuity for band gap materials. *Physical Review B*, 82:115106, Sep 2010. doi: 10.1103/PhysRevB.82.115106.
- [88] J. Heyd, G. E. Scuseria, and M. Ernzerhof. Hybrid functionals based on a screened coulomb potential. *The Journal of Chemical Physics*, 118(18):8207–8215, 2003. doi: 10.1063/1.1564060.
- [89] F. Bloch. Über die Quantenmechanik der Elektronen in Kristallgittern. *Zeitschrift für Physik*, 52:555–600, 1929. doi: 10.1007/BF01339455.
- [90] H. Hellmann. A new approximation method in the problem of many electrons. *The Journal of Chemical Physics*, 3(1):61–61, 1935. doi: 10.1063/1.1749559.
- [91] J. C. Slater. Wave functions in a periodic potential. *Physical Review*, 51:846–851, May 1937. doi: 10.1103/PhysRev.51.846.
- [92] P. E. Blöchl. Projector-augmented wave method. *Physical Review B*, 50:17953–17979, Dec 1994. doi: 10.1103/PhysRevB.50.17953.
- [93] H. J. Monkhorst and J. D. Pack. Special points for brillouin-zone integrations. *Physical Review B*, 13:5188–5192, Jun 1976. doi: 10.1103/PhysRevB.13.5188.
- [94] W. Setyawan and S. Curtarolo. High-throughput electronic band structure calculations: Challenges and tools. *Computational Materials Science*, 49(2):299–312, 2010. doi: 10.1016/j.commatsci.2010.05.010.
- [95] D. Porezag, Th. Frauenheim, T. Köhler, G. Seifert, and R. Kaschner. Construction of tight-binding-like potentials on the basis of density-functional theory: Application to carbon. *Physical Review B*, 51:12947–12957, May 1995. doi: 10.1103/PhysRevB.51.12947.
- [96] M. Elstner, D. Porezag, G. Jungnickel, J. Elsner, M. Haugk, Th. Frauenheim, S. Suhai, and G. Seifert. Self-consistent-charge density-functional tight-binding method for simulations of complex materials properties. *Physical Review B*, 58:7260–7268, Sep 1998. doi: 10.1103/PhysRevB.58.7260.
- [97] C. Köhler, G. Seifert, and Th. Frauenheim. Density functional based calculations for Fe_n ($n \leq 32$). *Chemical Physics*, 309(1):23–31, 2005. doi: 10.1016/j.chemphys.2004.03.034.
- [98] P. Koskinen and V. Mäkinen. Density-functional tight-binding for beginners. *Computational Materials Science*, 47(1):237–253, 2009. doi: 10.1016/j.commatsci.2009.07.013.
- [99] R. S. Mulliken. Electronic population analysis on LCAO–MO molecular wave functions. I. *The Journal of Chemical Physics*, 23(10):1833–1840, 1955. doi: 10.1063/1.1740588.
- [100] G. Kresse and J. Hafner. Ab initio molecular dynamics for liquid metals. *Physical Review B*, 47:558–561, Jan 1993. doi: 10.1103/PhysRevB.47.558.
- [101] G. Kresse and J. Hafner. Ab initio molecular-dynamics simulation of the liquid-metal–amorphous-semiconductor transition in germanium. *Physical Review B*, 49:14251–14269, 1994. doi: 10.1103/PhysRevB.49.14251.

- [102] G. Kresse and J. Furthmüller. Efficiency of ab-initio total energy calculations for metals and semiconductors using a plane-wave basis set. *Computational Materials Science*, 6(1):15–50, 1996. doi: 10.1016/0927-0256(96)00008-0.
- [103] G. Kresse and J. Furthmüller. Efficient iterative schemes for ab initio total-energy calculations using a plane-wave basis set. *Physical Review B*, 54:11169–11186, 1996. doi: 10.1103/PhysRevB.54.11169.
- [104] S. Nosé. A unified formulation of the constant temperature molecular dynamics methods. *The Journal of Chemical Physics*, 81(1):511–519, 1984. doi: 10.1063/1.447334.
- [105] W. G. Hoover. Canonical dynamics: Equilibrium phase-space distributions. *Physical Review A*, 31:1695–1697, Mar 1985. doi: 10.1103/PhysRevA.31.1695.
- [106] R. J. Bondi, M. P. Desjarlais, A. P. Thompson, G. L. Brennecke, and M. J. Marinella. Electrical conductivity in oxygen-deficient phases of tantalum pentoxide from first-principles calculations. *Journal of Applied Physics*, 114(20):203701, 2013. doi: 10.1063/1.4829900.
- [107] R. J. Bondi and M. J. Marinella. Oxidation state and interfacial effects on oxygen vacancies in tantalum pentoxide. *Journal of Applied Physics*, 117(8):085308, 2015. doi: 10.1063/1.4913206.
- [108] R. J. Bondi, B. P. Fox, and M. J. Marinella. Role of atomistic structure in the stochastic nature of conductivity in substoichiometric tantalum pentoxide. *Journal of Applied Physics*, 119(12):124101, 2016. doi: 10.1063/1.4943163.
- [109] B. Xiao and S. Watanabe. Oxygen vacancy effects on an amorphous-TaO_x-based resistance switch: a first principles study. *Nanoscale*, 6:10169–10178, 2014. doi: 10.1039/C4NR02173H.
- [110] A. N. Khitrova, V. V. Klechkovskaya, and J. Pinsker. Electron diffraction investigation of tantalum dioxide in thin films. *Kristallografiya*, 12:1044–1050, 1967.
- [111] K. Waltersson, B. Forslund, K.-A. Wilhelmi, S. Andersson, and J. Galy. The crystal structure of V₃O₇. *Acta Crystallographica Section B*, 30(11):2644–2652, 1974. doi: 10.1107/S0567740874007722.
- [112] K.-A. Wilhelmi and K. Waltersson. On the crystal structure of a new vanadium oxide, V₄O₉. *Acta Chemica Scandinavica*, 24:3409–3411, 1970. doi: 10.3891/acta.chem.scand.24-3406.
- [113] K.-A. Wilhelmi, K. Waltersson, and L. Kihlberg. A refinement of the crystal structure of V₆O₁₃. *Acta Chemica Scandinavica*, 25:2675–2687, 1971. doi: 10.3891/acta.chem.scand.25-2675.
- [114] S. F. Ho, S. Contarini, and J. W. Rabalais. Ion-beam-induced chemical changes in the oxyanions (Mo_yⁿ⁻) and oxides (Mo_x) where m = chromium, molybdenum, tungsten, vanadium, niobium and tantalum. *The Journal of Physical Chemistry*, 91(18):4779–4788, 1987. doi: 10.1021/j100302a027.

- [115] J. M. García Lastra, P. L. Cook, F. J. Himpsel, and A. Rubio. Communication: Systematic shifts of the lowest unoccupied molecular orbital peak in x-ray absorption for a series of 3d metal porphyrins. *The Journal of Chemical Physics*, 133(15):151103, 2010. doi: 10.1063/1.3497188.
- [116] N. Benito and C. Palacio. Nanostructuring of Ta₂O₅ surfaces by low energy Ar⁺ bombardment. *Applied Surface Science*, 351:753–759, 2015. doi: 10.1016/j.apsusc.2015.05.143.
- [117] R. Simpson, R. G. White, J. F. Watts, and M. A. Baker. XPS investigation of monatomic and cluster argon ion sputtering of tantalum pentoxide. *Applied Surface Science*, 405:79–87, 2017. doi: 10.1016/j.apsusc.2017.02.006.
- [118] R. F. W. Bader. *Atoms in Molecules: A Quantum Theory*. Oxford University Press, 1st edition, 1994.
- [119] Y. Li, Y. E. Suyolcu, S. Sanna, D. V. Christensen, M. L. Traulsen, E. Stamate, C. S. Pedersen, P. A. van Aken, J. M. García Lastra, V. Esposito, and N. Pryds. Tuning the resistive switching in tantalum oxide-based memristors by annealing. *AIP Advances*, 10(6):065112, 2020. doi: 10.1063/5.0004722.
- [120] J. Seo, D. Cha, Kazuhiro T., Jun K., and Kazunari D. Electrodeposited ultrafine NbO_x, ZrO_x, and TaO_x nanoparticles on carbon black supports for oxygen reduction electrocatalysts in acidic media. *ACS Catalysis*, 3(9):2181–2189, 2013. doi: 10.1021/cs400525u.
- [121] Z. Awaludin, T. Okajima, and T. Ohsaka. Preparation of reduced tantalum pentoxide by electrochemical technique for oxygen reduction reaction. *Journal of Power Sources*, 268:728–732, 2014. doi: 10.1016/j.jpowsour.2014.06.102.
- [122] A. V. Korshunov, A. V. Pustovalov, T. P. Morozova, and D. O. Perevezentseva. Oxidation of fine tantalum particles: Metastable intermediates and multistep kinetics. *Oxidation of metals*, 93:301–328, 2020. doi: 10.1007/s11085-020-09957-8.
- [123] A. H. Larsen, J. J. Mortensen, J. Blomqvist, I. E. Castelli, R. Christensen, M. Dułak, J. Friis, M. N. Groves, B. Hammer, C. Hargus, E. D. Hermes, P. C. Jennings, P. B. Jensen, J. Kermode, J. R. Kitchin, E. L. Kolsbjerg, J. Kubal, K. Kaasbjerg, S. Lysgaard, J. B. Maronsson, T. Maxson, T. Olsen, L. Pastewka, A. Peterson, C. Rostgaard, J. Schiøtz, O. Schütt, M. Strange, K. S. Thygesen, T. Vegge, L. Vilhelmsen, M. Walter, Z. Zeng, and K. W. Jacobsen. The atomic simulation environment—a python library for working with atoms. *Journal of Physics: Condensed Matter*, 29(27):273002, Jun 2017. doi: 10.1088/1361-648x/aa680e.
- [124] J. H. Chang, D. Kleiven, M. Melander, J. Akola, J. M. García Lastra, and T. Vegge. CLEANSE: a versatile and user-friendly implementation of cluster expansion method. *Journal of Physics: Condensed Matter*, 31(32):325901, 2019. doi: 10.1088/1361-648x/ab1bbc.
- [125] S. L. Dudarev, G. A. Botton, S. Y. Savrasov, C. J. Humphreys, and A. P. Sutton. Electron-energy-loss spectra and the structural stability of nickel oxide: An LSDA+U study. *Physical Review B*, 57:1505–1509, Jan 1998. doi: 10.1103/PhysRevB.57.1505.

- [126] J. Stausholm-Møller, H. H. Kristoffersen, B. Hinnemann, G. K. H. Madsen, and B. Hammer. DFT+U study of defects in bulk rutile TiO₂. *The Journal of Chemical Physics*, 133(14):144708, 2010. doi: 10.1063/1.3492449.
- [127] Y. Muraoka, Y. Fujimoto, M. Kameoka, Y. Matsuura, M. Sunagawa, K. Terashima, T. Wakita, and T. Yokoya. Preparation of TaO₂ thin films using NbO₂ template layers by a pulsed laser deposition technique. *Thin Solid Films*, 599:125–132, 2016. doi: 10.1016/j.tsf.2015.12.066.
- [128] T. McQueen, Q. Xu, E. N. Andersen, H. W. Zandbergen, and R. J. Cava. Structures of the reduced niobium oxides Nb₁₂O₂₉ and Nb₂₂O₅₄. *Journal of Solid State Chemistry*, 180(10):2864–2870, 2007. doi: 10.1016/j.jssc.2007.08.013.
- [129] R. Norin. The crystal structure of Nb₁₂O₂₉ (orh). *Acta Chemica Scandinavica*, 17: 1391–1404, 1963. doi: 10.3891/acta.chem.scand.17-1391.
- [130] G. Brauer. Die Oxyde des Niobs. *Zeitschrift für anorganische und allgemeine Chemie*, 248(1):1–31, 1941. doi: 10.1002/zaac.19412480101.
- [131] R. J. Cava, B. Batlogg, J. J. Krajewski, P. Gammel, H. F. Poulsen, W. F. Peck Jr., and L. W. Rupp Jr. Antiferromagnetism and metallic conductivity in Nb₁₂O₂₉. *Nature*, 350:598–600, 1991. doi: 10.1038/350598a0.
- [132] C. M. Fang, M. A. van Huis, Q. Xu, R. J. Cava, and H. W. Zandbergen. Unexpected origin of magnetism in monoclinic Nb₁₂O₂₉ from first-principles calculations. *Journal of Materials Chemistry C*, 3:651–657, 2015. doi: 10.1039/C4TC02222J.
- [133] A. Paris and S. Taioli. Multiscale investigation of oxygen vacancies in TiO₂ anatase and their role in memristor’s behavior. *The Journal of Physical Chemistry C*, 120(38): 22045–22053, 2016. doi: 10.1021/acs.jpcc.6b07196.
- [134] J. Kullgren, M. J. Wolf, K. Hermansson, C. Köhler, B. Aradi, Th. Frauenheim, and P. Broqvist. Self-consistent-charge density-functional tight-binding (SCC-DFTB) parameters for ceria in 0D to 3D. *The Journal of Physical Chemistry C*, 121(8):4593–4607, 2017. doi: 10.1021/acs.jpcc.6b10557.
- [135] J. M. Knaup, M. Wehlau, and Th. Frauenheim. Dynamic simulation of the migration of oxygen vacancy defects in rutile TiO₂. *MRS Proceedings*, 1430:mrss12–1430–e08–10, 2012. doi: 10.1557/opl.2012.936.
- [136] B. Hourahine, B. Aradi, V. Blum, F. Bonafé, A. Buccheri, C. Camacho, C. Cevallos, M. Y. Deshayé, T. Dumitrică, A. Dominguez, S. Ehlert, M. Elstner, T. van der Heide, J. Hermann, S. Irle, J. J. Kranz, C. Köhler, T. Kowalczyk, T. Kubař, I. S. Lee, V. Lutsker, R. J. Maurer, S. K. Min, I. Mitchell, C. Negre, T. A. Niehaus, A. M. N. Niklasson, A. J. Page, A. Pecchia, G. Penazzi, M. P. Persson, J. Řezáč, C. G. Sánchez, M. Sternberg, M. Stöhr, F. Stuckenberg, A. Tkatchenko, V. W.-z. Yu, and Th. Frauenheim. DFTB+, a software package for efficient approximate density functional theory based atomistic simulations. *The Journal of Chemical Physics*, 152(12):124101, 2020. doi: 10.1063/1.5143190.
- [137] E. van Lenthe, A. Ehlers, and E.-J. Baerends. Geometry optimizations in the zero order regular approximation for relativistic effects. *The Journal of Chemical Physics*, 110(18):8943–8953, 1999. doi: 10.1063/1.478813.

- [138] A. Fihey, C. Hettich, J. Touzeau, F. Maurel, A. Perrier, C. Köhler, B. Aradi, and Th. Frauenheim. SCC-DFTB parameters for simulating hybrid gold-thiolates compounds. *Journal of Computational Chemistry*, 36(27):2075–2087, 2015. doi: 10.1002/jcc.24046.
- [139] H. J. C. Berendsen, J. P. M. Postma, W. F. van Gunsteren, A. DiNola, and J. R. Haak. Molecular dynamics with coupling to an external bath. *The Journal of Chemical Physics*, 81(8):3684–3690, 1984. doi: 10.1063/1.448118.
- [140] S. Kakio, K. Hosaka, M. Arakawa, Y. Ohashi, and J.-i. Kushibiki. Surface acoustic wave properties of amorphous Ta₂O₅ and Nb₂O₅ thin films prepared by radio frequency sputtering. *Japanese Journal of Applied Physics*, 51:07GA01, jul 2012. doi: 10.1143/jjap.51.07ga01.

Appendix A

Evaluation of DFT+U

Figure A.1 shows v_O formation energies calculated using PBE+U for $U = 0\text{ eV}$ to 5 eV compared to HSE-calculated values (represented by horizontal lines). All calculations use the 168-atom supercell to minimise interactions between periodically repeated vacancies. No value of U results in a perfect match. However, PBE+0 correctly predicts the threefold in-plane (3f ip) defect to be significantly more stable than the twofold in-plane (2f ip) and twofold out-of-plane (2f oop) defects. No finite value for U reproduces this feature. For this reason, the study of oxygen vacancy-defective $\lambda\text{-Ta}_2\text{O}_5$ used regular PBE, with the expectation that the (stable) defect structure will be dominated by the 3f ip defect.

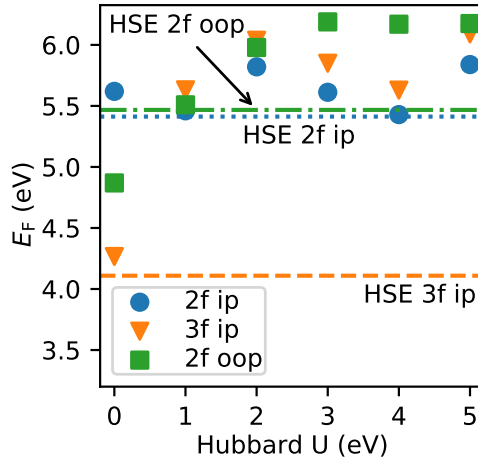


Figure A.1: v_O formation energies calculated with PBE+U for $U=0\text{ eV}$ to 5 eV . Horizontal lines show HSE-calculated energies. Labels refer to twofold in-plane (2f ip), threefold in-plane (3f ip), and twofold out-of-plane (2f oop) vacancy sites.

Appendix B

Comparison of single- v_{O} charge densities

The real-space charge densities associated with the three different v_{O} are shown in Figure B.1. Frames (a-c) are relaxed using PBE, while (d-f) are relaxed using Γ -point HSE. The comparison is qualitative only, as differing isovalues were used. For each vacancy, standard PBE arrives at the correct description; i.e. localised vs. non-localised. The greatest discrepancy is found for the 3f oop vacancy, which was observed in Chapter A to be more stable within PBE than HSE.

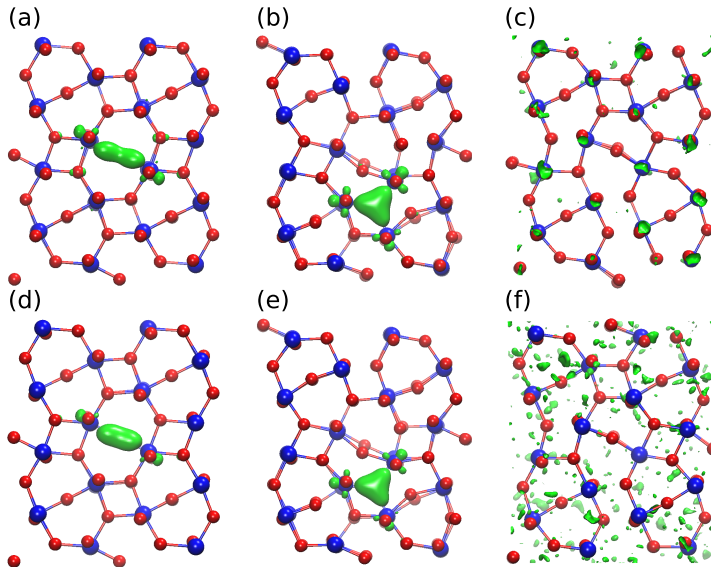


Figure B.1: Charge densities (green) for singular v_{O} calculated using PBE (a-c) and Γ -point HSE (d-f). (a+d): Twofold coordinated in-plane; (b+e): Threefold coordinated in-plane; (c+f): Twofold coordinated out-of-plane.

Appendix C

Density of amorphous TaO_x

Figure C.1 shows a series of boxplots of the calculated mass densities of the amorphous structures created and investigated in Chapter 3. The experimental density of a- Ta_2O_5 as determined in reference 140 is highlighted in red, and corresponds well to the mean density found for this stoichiometry. The fit to mean densities shows a linearly increasing trend. No clear tendency for the location of the minimum-energy image with respect to the mean is observed. Low-energy stoichiometries ($x = \{0.0, 0.67, 1.00\}$) exhibit higher spread as well as higher mean density with respect to the fit than high-energy stoichiometries ($x = \{0.33, 0.50, 0.80\}$).

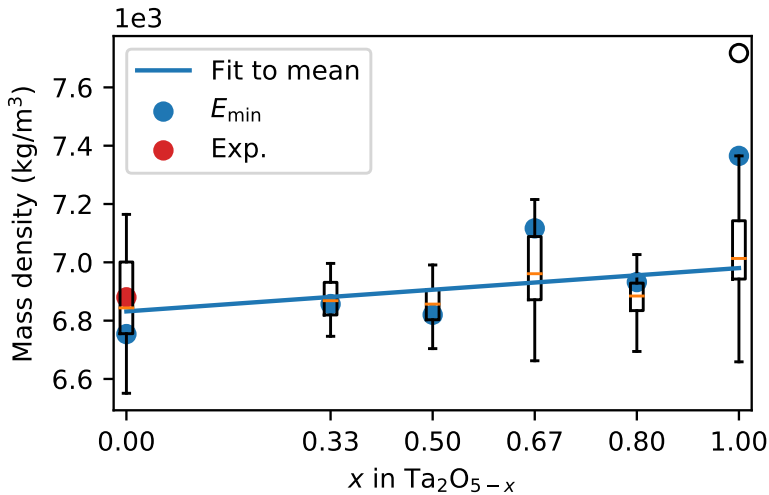


Figure C.1: Calculated mass densities of a- TaO_x . Orange lines show mean densities. Blue line represents a linear fit to the mean values. Blue circles show the densities of the minimum-energy structure for each stoichiometry.

Publications

Publication 1

Phase separation in amorphous tantalum oxide from first principles

C. S. Pedersen, J. H. Chang, Y. Li, N. Pryds, J. M. García Lastra

APL Mater. **8**, 071108 (2020)

Reproduced with the permission of AIP Publishing.

Phase separation in amorphous tantalum oxide from first principles

Cite as: APL Mater. **8**, 071108 (2020); <https://doi.org/10.1063/5.0011390>
 Submitted: 20 April 2020 . Accepted: 25 June 2020 . Published Online: 13 July 2020

Christian Søndergaard Pedersen , Jin Hyun Chang , Yang Li , Nini Pryds , and Juan Maria Garcia Lastra 



View Online



Export Citation



CrossMark

ARTICLES YOU MAY BE INTERESTED IN

Scattering mechanisms and mobility enhancement in epitaxial BaSnO₃ thin films probed via electrolyte gating

APL Materials **8**, 071113 (2020); <https://doi.org/10.1063/5.0017227>

Oxygen vacancies: The (in)visible friend of oxide electronics

Applied Physics Letters **116**, 120505 (2020); <https://doi.org/10.1063/1.5143309>

Understanding the interplay of surface structure and work function in oxides: A case study on SrTiO₃

APL Materials **8**, 071110 (2020); <https://doi.org/10.1063/1.5143325>

additive manufacturing epitaxial crystal growth cerium oxide polishing powder silver nanoparticles sputtering targets III-IV semiconductors CVD precursors europium phosphors

AMERICAN ELEMENTS

THE ADVANCED MATERIALS MANUFACTURER®

deposition slugs OLED Lighting spintronics solar energy

osmium nanoribbons thin films chalcogenides AuNPs

GDC lithium battery electrolytes 99.999% ruthenium spheres

endohedral fullerenes copper nanoparticles diamond micropowder

CIGS MBE grade materials palladium catalysts flexible electronics

beta-barium borate borosilicate-glass dysprosium pellets YBCO

pyrolytic graphite 3d graphene foam indium tin oxide mesoporous silica

raman substrates sapphire windows tungsten carbide InGaAs

barium fluoride carbon nanotubes lithium niobate scandium powder

gallium lump glassy carbon nanodispersions

surface functionalized nanoparticles

organometallics quantum dots

III-V semiconductors laser crystals ultra high purity materials MOFs

rare earth metals photovoltaics refractory metals MOCVD

superconductors transparent ceramics ultra high purity silicon

American Elements opens up a world of possibilities so you can **Now Invent!**

Over 15,000 certified high purity laboratory chemicals, metals, & advanced materials and a state-of-the-art Research Center. Printable GHS-compliant Safety Data Sheets. Thousands of new products. And much more. All on a secure multi-language 'Mobile Responsive' platform.

perovskite crystals yttrium iron garnet alternative energy h-BN

gold nanocubes graphene oxide macromolecules photonics

rhodium sponge fiber optics beamsplitters infrared dyes zeolites

fused quartz metallocenes platinum ink buckyballs Ti-6Al-4V

Now Invent.™

The Next Generation of Material Science Catalogs

www.americanelements.com



Phase separation in amorphous tantalum oxide from first principles

Cite as: APL Mater. 8, 071108 (2020); doi: 10.1063/5.0011390

Submitted: 20 April 2020 • Accepted: 25 June 2020 •

Published Online: 13 July 2020



Christian Søndergaard Pedersen,¹ Jin Hyun Chang,¹ Yang Li,¹ Nini Pryds,¹ and Juan Maria Garcia Lastra¹

AFFILIATIONS

Department of Energy Conversion and Storage, Technical University of Denmark, DK-2800 Kgs. Lyngby, Denmark

¹Author to whom correspondence should be addressed: jchang@dtu.dk

¹Electronic mail: jmgla@dtu.dk

ABSTRACT

The transition between Ta₂O₅ and TaO₂ governs resistive switching in tantalum oxide-based resistive random access memory. Despite its importance, the Ta₂O₅–TaO₂ transition is scarcely described in the literature, in part because the tantalum oxide layer in devices is amorphous, which makes it difficult to characterize. In this paper, we use first-principles calculations to construct the convex hull of the amorphous Ta₂O_{5–x} system for 0 ≤ x ≤ 1 and show that oxygen deficiency in tantalum oxide leads to phase-separation into Ta₂O₅ and TaO₂. In addition, our work challenges the conventional interpretation of X-ray Photoelectron Spectroscopy (XPS) spectra of the Ta 4f orbitals. Specifically, we find that TaO₂ exhibits both the Ta⁴⁺ peak associated with TaO₂ and the Ta⁵⁺ peak normally associated with Ta₂O₅. While our simulated Ta₂O₅ peak originates from a narrow range of oxidation states, the TaO₂ peak comes from disproportionated Ta atoms with Bader charges ranging from +3 to +1, the lowest of which are well below Ta atoms in crystalline TaO. Finally, we demonstrate that the XPS blueshift of around 1 eV observed experimentally in amorphous Ta₂O₅ with respect to crystalline Ta₂O₅ comes from both the presence of under-coordinated Ta atoms and longer Ta–O bond distances in the amorphous system. Our simulated XPS analysis shows that amorphous XPS spectra may be more complex than previously thought, and hence, caution should be applied when assigning XPS peaks to oxidation states.

© 2020 Author(s). All article content, except where otherwise noted, is licensed under a Creative Commons Attribution (CC BY) license (<http://creativecommons.org/licenses/by/4.0/>). <https://doi.org/10.1063/5.0011390>

I. INTRODUCTION

Resistive switching devices constitute an important research topic within the general area of random access memory (RAM) technology.^{1,2} Since Chua proposed the “memristor”—memory resistor—in 1971,³ researchers have demonstrated memory resistive properties in metal/metal-oxide/metal devices^{4,5} using semi-conducting and insulating transition metal oxides such as TiO₂,⁴ HfO₂,^{6,7} and Ta₂O₅.⁸ as the active layer. The switching mechanism in these layers is initiated by applying a large electric field across the device. This leads to the creation and subsequent migration of oxygen vacancy (v_O) defects and eventually to the growth of nanoscale filaments of oxygen-deficient and conductive regions through the device.^{9–11}

Tantalum pentoxide (Ta₂O₅) is one of the key candidate materials for the switching layer of memristive switching devices. In a direct comparison to TiO₂, which was the first material to be linked to memristive switching,⁴ Ta₂O₅ shows five times greater

ionic mobility^{4,12} and, by extension, may yield greater switching speed and lower power consumption.¹³ Additionally, a switching endurance exceeding 10¹² cycles has been demonstrated without device breakdown.¹⁴

Structurally, Ta₂O₅ thin films fabricated at low to room temperature are amorphous,^{15–17} which makes them difficult to study on a theoretical level. Nevertheless, previous *ab initio* Molecular Dynamics (AIMD) studies based on Density Functional Theory (DFT) have provided in-depth investigations of amorphous tantalum oxide. Utilizing the atomic-level information offered by DFT, researchers have described atomic arrangements surrounding singular v_O's,¹⁸ density-of-states spectra of several TaO_x stoichiometries,¹⁹ electrical conductivity of TaO_x,²⁰ and formation energies of v_O's in Ta₂O₅ close to a Ta–Ta₂O₅ interface.²¹ To our knowledge, however, neither experiment nor simulation has thus far attempted to map the Ta₂O₅–TaO₂ transition, which governs resistive switching in TaO_x devices.

One reason for this is that determining the exact composition of amorphous materials is a non-trivial task, which is highly dependent on fabrication parameters.¹⁷ Several studies have applied X-ray Photoelectron Spectroscopy (XPS) to obtain binding energies (BEs) especially for the Ta 4f orbitals.^{17,22–27} Usually, the resultant spectra are deconvoluted using Gaussian/Lorentzian functions^{17,24,26,27} assigned either to different oxidation states of Ta or to different stoichiometries. The two assignments can be used interchangeably since the stoichiometries Ta₂O₅, TaO₂, Ta₂O₃, TaO, Ta₂O, and Ta correspond to the oxidation states +5, +4, +3, +2, +1, and 0, respectively. A compositional analysis can be performed based on the relative areas underneath the fitting functions. However, the XPS spectra of amorphous materials are more complex compared to crystalline materials, which exhibit well-defined patterns.

In this study, we zoom in on the transition between Ta₂O₅ and TaO₂, which is the range of compositions where resistive switching takes place. We use DFT to investigate amorphous Ta₂O_{5–x} (a-Ta₂O_{5–x}), sampling 14 different snapshots for each of six different compositions with $0 \leq x \leq 1$. We draw the convex hull for the Ta₂O₅–TaO₂ transition and confirm that the hull consists of these two stoichiometries, with Ta₆O₁₃ being another possible meta-stable intermediate phase. Furthermore, we simulate XPS spectra for each stoichiometry and show that the XPS spectrum of TaO₂ shows both Ta⁵⁺ and Ta⁴⁺ peaks, the latter of which comes from disproportionated atoms with a wide range of oxidation states. Finally, by fitting Gaussian components to our oxidation state spectra and our XPS spectra, we establish a linear correlation between the Gaussian peak locations. These conclusions aid the understanding of XPS results of a-Ta₂O₅ and amorphous materials in general.

II. METHODS

All calculations employed DFT as implemented in the Vienna *Ab initio* Simulation Package (VASP).^{28–31} Ta and O atoms used Projector Augmented Wave (PAW) pseudopotentials³² with valence electron configurations of 5p⁶5d³6s² and 2s²2p⁴, respectively. Calculations used the Perdew–Burke–Ernzerhof (PBE) Generalized Gradient Approximation (GGA)³³ to describe the exchange–correlation functional, except where noted otherwise. The convergence threshold of the electronic structure iterations was set to 10^{–5} eV.

Amorphous systems of Ta₂O_{5–x}, $x \in \{0.00, 0.33, 0.50, 0.67, 0.80, 1.00\}$, were generated using AIMD. Beginning with the primitive cell of λ -Ta₂O₅ suggested by Lee *et al.*,³⁴ we created a 2 × 2 × 3 orthogonal supercell containing 48 Ta atoms and 120 O atoms, the same size as those used by Bondi *et al.*^{18,20} and Guo and Robertson.³⁵ Oxygen atoms were subsequently deleted randomly to obtain 8, 12, 16, 20, and 24 vacancies. We expanded each lattice vector by a factor of 1.06, which was chosen to match the experimental density for a-Ta₂O₅ of 6.88 × 10³ kg/m³.³⁶ The expanded cell vectors were kept fixed throughout the duration of the MD simulations.

The amorphous structure generation used the following melt-and-quench procedure: (1) equilibration at 5000 K for 10 ps, (2) further equilibration and extraction of in total 14 structure snapshots per stoichiometry in intervals of 2 ps following the initial equilibration, (3) quenching of each snapshot from 5000 K to 300 K, and (4) equilibration for 2 ps at 300 K. The MD simulations used a low-accuracy/high-speed setup with a cutoff energy of 300 eV and

sampling only the Γ point. The time step was 1 fs for equilibrations and 2 fs for quenching.

Following the AIMD procedure, we increased the cutoff energy to 520 eV and k point sampling to (2 × 2 × 2) and performed full DFT relaxations of ionic positions and lattice vectors. Despite the relaxation of the lattice vectors, the average density of the final Ta₂O₅ geometry was still similar to the experimental density (see Fig. S1 of the supplementary material). Atomic forces were converged to within 0.025 eV/Å, which resulted in little change to the cell volume and thus density. We performed a high-precision calculation of the optimized structures using the hybrid functional of Heyd–Ernzerhof–Scuseria (HSE06).^{37–39} Due to their high computational demands, these calculations sampled only the Γ point. Following these calculations, the BEs of the Ta 4f orbitals were computed using the initial state approximation, which involves recalculating the Kohn–Sham eigenvalues of the core states after a self-consistent calculation of the valence charge density. The HSE06-calculated wave functions served as the basis for a Bader charge analysis⁴⁰ using the program developed by Henkelmann *et al.*⁴¹

In addition to our amorphous systems, we performed PBE relaxation followed by HSE06 calculations of the following crystalline structures: λ -Ta₂O₅, rutile TaO₂, corundum Ta₂O₃, rocksalt TaO, and BCC Ta. These calculations used the same setup as the DFT calculations of the amorphous systems with a k point sampling density of at least 3.60 k points per Å^{–1}.

III. RESULTS AND DISCUSSION

A. Energetic stability and structural analysis

We first examine the phase change between Ta₂O₅ and TaO₂ as well as differences in the Ta–O bonding. Figure 1 presents the convex hull, cumulative distribution function (CDF) for Ta–O bonds limited to the sixth nearest neighbor, and a histogram of Ta coordination numbers for all simulated systems (radial distribution functions can be found in Fig. S2 of the supplementary material). The total energies making up the hull are extracted from the HSE06 calculations and subsequently normalized to 24 formula units (f.u.). Our high sampling of 14 structures per stoichiometry allows us to visualize the energy variance, providing reassurance that our convex hull is accurate.

The convex hull in Fig. 1(a) shows a preference for phase separation into Ta₂O₅ and TaO₂. However, while Ta₃O₇ ($x = 0.33$), Ta₄O₉ ($x = 0.50$), and Ta₁₂O₂₅ ($x = 0.80$) lie on average more than 0.6 eV above the hull, Ta₆O₁₃ ($x = 0.67$) is considerably lower at only 0.11 eV above the hull. Our calculations show a clear division into high-energy and low-energy stoichiometries, and we expect some degree of similarity between the three low-energy stoichiometries.

To investigate what the three low-energy stoichiometries (Ta₂O₅, Ta₆O₁₃, and TaO₂) have in common, we consider the CDF for the Ta–O bonds in the atomic structures of Fig. 1(a). Since Ta is sixfold coordinated in most, if not all, stable and metastable crystalline TaO_x phases, we limit our investigation to exactly the sixth-nearest neighbor. The resultant spectra are shown in Fig. 1(b). All systems are characterized by an ascent beginning at ~2.0 Å and ending at ~2.5 Å. Therefore, we use 2.5 Å as the cutoff radius when an O atom counts toward the coordination number of a Ta atom. The height of the initial ascent thus describes the ratio of fully sixfold

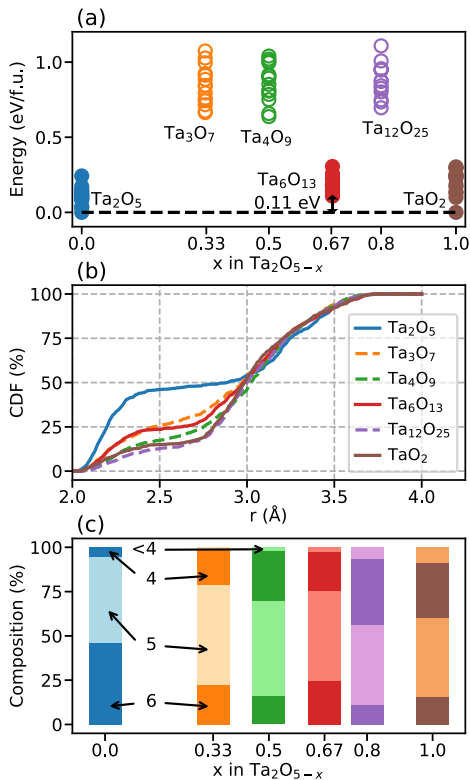


FIG. 1. (a) Convex hull for the a-Ta₂O₅–TaO₂ system. (b) CDF for sixth-nearest O neighbors of Ta atoms. (c) Histogram of the coordination number of Ta atoms in each stoichiometry. Color coding is consistent throughout.

coordinated Ta atoms, and the low-energy systems are characterized by relatively larger quantities of fully coordinated Ta atoms than are seen for the high-energy systems. Within this picture, it is also clear that over 50% of Ta atoms are under-coordinated in all stoichiometries, including a-Ta₂O₅. We further illustrate the trends in coordination numbers in Fig. 1(c) by plotting coordination numbers 6, 5, 4, and <4 in a cumulative histogram. In particular, Ta₆O₁₃ and TaO₂ show higher sixfold coordination and lower fourfold coordination than stoichiometries with slightly greater oxygen content.

It is worth mentioning that two of the three low-energy stoichiometries, TaO₂ and Ta₂O₅, exist in crystalline form.⁴² The crystalline form of the other low-energy stoichiometry, Ta₆O₁₃, has not been reported in the literature. However, tantalum shares periodic table Group 5 with vanadium, and V₆O₁₃ has been found in a crystalline form where vanadium is also sixfold coordinated.⁴³ In contrast, the high-energy stoichiometries indicated in Fig. 1 either have no corresponding crystalline Group 5 metal-oxide phase (Ta₁₂O₂₅),⁴⁶ or have corresponding crystalline phases with lower

cation coordination numbers (Ta₃O₇ and Ta₄O₉).^{47,48} This analogy with crystalline phases underlines the importance of conserving the Ta sixfold coordination to keep the system stable. This explains why amorphous Ta₂O₅, Ta₆O₁₃, and TaO₂ exhibit a relatively high degree of Ta sixfold coordination and are thus particularly stable, while Ta₃O₇, Ta₄O₉ and Ta₁₂O₂₅ do not.

B. XPS spectra

In this section, we present simulated XPS spectra for our systems and compare them to the experimental XPS spectra reported by Benito and Palacio,²⁶ Simpson *et al.*,²⁷ and Li *et al.*¹⁷ To this end, we calculate the energies of the core electrons of the Ta 4f orbital, which correspond to measuring their BEs, thus simulating an XPS spectrum.

We “calibrated” our XPS results in two ways prior to making any comparisons. We benchmarked our 4f binding energy spectra for the crystalline λ phase⁴⁴ of Ta₂O₅ (19.1 eV) against the Ta_{7/2}⁵⁺ peak reported by Ho, Contarini, and Rabalais²⁴ for crystalline Ta₂O₅. The reported XPS peak value is 26.2 eV; hence, we shifted all our XPS spectra uniformly by 26.2 eV – 19.1 eV = 7.1 eV. Such a shift is customary, and even necessary, in order to compare DFT-calculated XPS results to experiment.⁴⁴ Additionally, we remark that realistic XPS spectra are usually obtained at room temperature, whereas DFT calculations are performed at 0 K. We applied Gaussian broadening to our data to overcome this difference using a broadening width obtained from the energy spectrum of 2000 AIMD iterations at 300 K using a 520 eV cutoff energy and (2 × 2 × 2) *k* point grid. With these two alterations, we proceed to discuss our XPS spectra and compare them to the aforementioned experimental results.

Figure 2(a) presents our calculated XPS spectrum for a-Ta₂O₅ with a single Gaussian function fitted to it. The fit is near perfect, signifying that the XPS spectrum comes from atoms with uniform oxidation states. The spectrum of a-TaO₂ in Fig. 2(b), by contrast, shows two peaks and has been deconvoluted using two Gaussian functions. We find that our calculated peaks’ positions lie slightly above those reported by Benito and Palacio, Simpson *et al.*, and Li *et al.* The calculated highest energy peak (i.e., the one usually assigned to Ta⁵⁺ in the literature) and the second-highest energy peak (i.e., the one usually assigned to Ta⁴⁺ in the literature) are blueshifted 0.22–0.32 eV and 0.22–0.42 eV relative to the experimental values, respectively. The calculated spacing between peaks is 1.4 eV, which corresponds well with the spacing reported by Simpson *et al.* (1.3 eV) and Li *et al.* (1.6 eV). The slight blueshift of our results compared to the experimental values could arise from using the initial state approximation to calculate the core-level energies. Overall, we believe that our peak locations and spacing are in good agreement with experiment.

Apart from matching experiments, we highlight the XPS spectrum of TaO₂ as a particularly important result. Even in a sample with a nominal Ta oxidation state of +4, the Ta⁵⁺ peak is visibly present. Additionally, the Ta⁴⁺ curve is significantly wider than the Ta⁵⁺ curve, which contradicts the deconvolutions performed in the previous experimental studies.^{17,26,27} For this reason, we recommend caution when using deconvoluted XPS spectra to perform compositional analyses on amorphous a-TaO_x samples and likely for other amorphous metal-oxide samples.

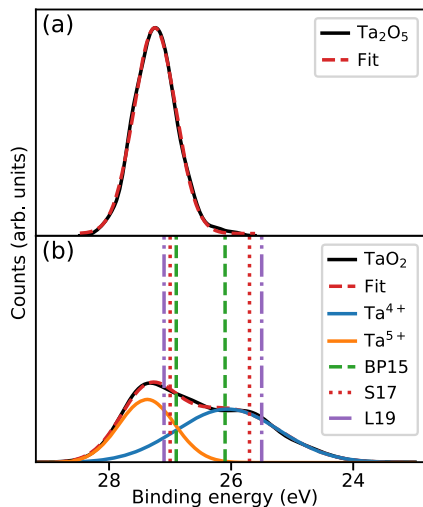


FIG. 2. As-calculated XPS spectra (black curves) and Gaussian fit (red dashed curves) for (a) $a\text{-Ta}_2\text{O}_5$ and (b) $a\text{-TaO}_2$. TaO_2 in (b) also includes deconvoluted Gaussians (orange and blue curves) and the Ta^{5+} and Ta^{4+} peak locations from the works of Benito and Palacio²⁶ (BP15), Simpson *et al.*²⁷ (S17), and Li *et al.*¹⁷ (L19), presented as vertical lines.

C. Bader analysis

Our CDF spectra showed how a significant fraction of Ta atoms in all samples are under-coordinated, i.e., less than 6 oxygen neighbors within 2.5 Å. We now examine the connection between the Ta coordination numbers, BEs, and Bader charges (which provide an

indication of the oxidation state). Figures 3(a)–3(c) shows the as-calculated Ta 4f binding energies plotted against their corresponding Bader charges for the three low-energy stoichiometries (Ta_2O_5 , Ta_6O_{13} , and TaO_2). Atoms are color- and shape-coded according to the number of oxygen neighbors within 2.5 Å. Also shown are five points corresponding to crystalline Ta–O phases and elemental Ta along with kernel density estimates of the Bader charges (horizontal axis) and BEs (vertical axis). Discussions henceforth are limited to the low-energy stoichiometries.

For stoichiometric Ta_2O_5 , the observed XPS peak comes from a narrow range of Bader charges centered at roughly +3, which is consistent with the results of Xiao and Watanabe.¹⁹ Any slight variation in Bader charge is clearly related to the coordination number of Ta, visible as discernible regions of different colors. As O deficiency increases, the Bader charge spectrum becomes smeared out in direction toward lower positive charge, i.e., Ta atoms retain more of their valence electrons. However, a significant part of the Ta_2O_5 spectrum—highlighted by the dashed ellipsis—remains even for TaO_2 . Evidently, for $x > 0$, $a\text{-Ta}_2\text{O}_{5-x}$ becomes disproportionated, which is the origin of the dual peak spectrum we observe for TaO_2 .

In comparison with crystalline phases, the Ta atoms of the amorphous structures exhibit much higher BEs even at lower oxidation states. For Ta_2O_5 , the calculated difference between the BE of the Ta 4f orbitals in the crystalline phase and the center of the Gaussian peak of the amorphous phase is around 1 eV, in excellent agreement with the experimental difference (compare the results of the amorphous phase by Benito and Palacio,²⁶ Simpson *et al.*,²⁷ and Li *et al.*¹⁷ with those of the crystalline phase by Ho, Contarini, and Rabalais²⁴). For lower Ta oxidation states, the differences in BEs between amorphous samples and their crystalline counterparts become even more pronounced. This phenomenon can be understood by comparing the coordination number of Ta atoms between the crystalline and amorphous phases. While Ta is always sixfold coordinated for crystalline phases, every considered amorphous

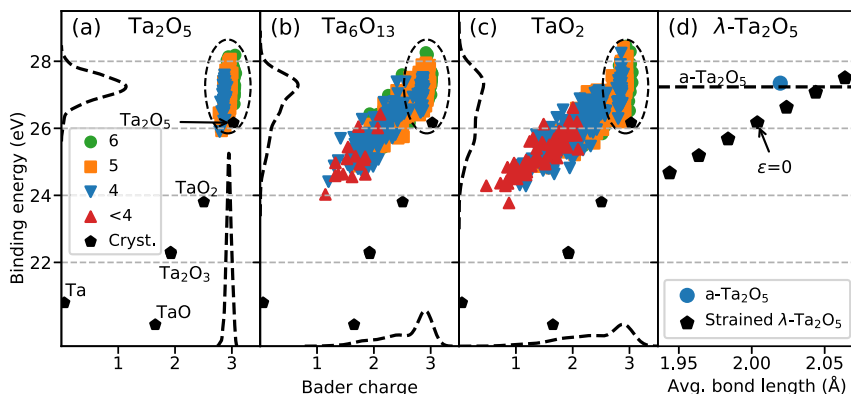


FIG. 3. Binding energy vs Bader charge for amorphous (a) Ta_2O_5 , (b) Ta_6O_{13} , and (c) TaO_2 . Green/orange/blue/red markers represent Ta atoms that are 6/5/4/<4-fold coordinated, respectively. (d) shows $\lambda\text{-Ta}_2\text{O}_5$ compressed/expanded up to 3%. The blue circle represents the average binding energy and average bond length for all sixfold coordinated Ta atoms in $a\text{-Ta}_2\text{O}_5$.

phase shows a large degree of under-coordination, especially for Ta atoms with lower oxidation states.

The change in coordination number is not the only cause of the difference in BEs between amorphous and crystalline phases. In Fig. 3(d), we show the variation of the BE peak for crystalline Ta₂O₅ when varying the lattice parameter of the crystal (which is equivalent to varying the average Ta–O distances). We scan the variation of the Ta 4f binding energy in the range from $\epsilon = -0.03$ to $\epsilon = +0.03$, where ϵ is the relative expansion factor applied to the lattice parameters. We observe a quasi-linear correlation in the investigated region between the BE of Ta 4f orbitals and average Ta–O bond length, which is consistent with the expected reduction of the Coulombic repulsion between the Ta 4f electron and the oxygen ligands when the Ta–O distance increases. We observe that the average Ta–O distances for the sixfold coordinated Ta atoms in Ta₂O₅ are ~2 pm larger than those in crystalline λ -Ta₂O₅ (at $\epsilon = 0$). Thus, we do not only attribute the blueshift in BEs in the amorphous samples to under-coordinated Ta atoms but also to the increase in the Ta–O distances for sixfold coordinated Ta atoms in amorphous samples relative to crystalline ones.

We now examine the relation between the Bader charge and BE hinted in Fig. 3 in detail. For the crystalline phases plotted in Figs. 3(a)–3(c), there appears to be a linear relation between BE and Bader charge. Hence, in Figs. 4(a) and 4(b), we present a simple linear fit between BE and Bader charge for amorphous Ta₂O₅ and TaO₂. For a-Ta₂O₅, the linear fit performs poorly, achieving a correlation coefficient r of 0.461. The correlation is greater ($r = 0.881$) in a-TaO₂ due to the smeared Bader charge spectrum. In Figs. 4(c) and 4(d), we attempt to improve the linear fit by incorporating a term describing differences in the coordination number and the Ta–O distances. We use the term suggested by Ebadi *et al.*,⁴⁵ which is expressed as

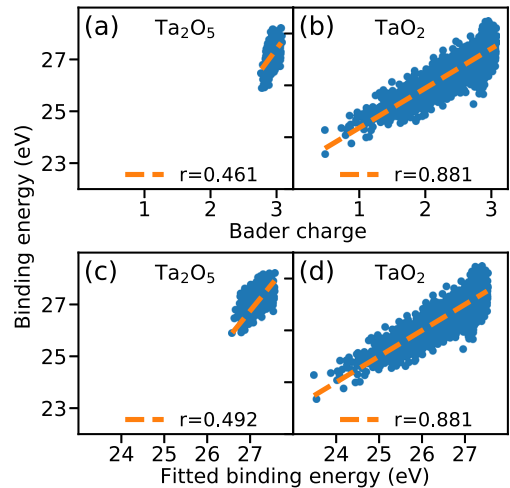


FIG. 4. [(a) and (b)] Linear fit of binding energy to Bader charge for a-Ta₂O₅ (a) and a-TaO₂ (b). [(c) and (d)] Corrected fit based on the work of Ebadi *et al.*⁴⁵ for the same data as the upper row.

$$BE_A = \beta_0 q_A + \beta_1 \sum_{i=A} \frac{q_i}{r_{iA}} + \beta_2, \quad (1)$$

where subscripts A and i represent the Ta ions and their 6 nearest O neighbors in our implementation, respectively, q is the Bader charge, r is the distance between i and A, and $\beta_{0,1,2}$ are fitting parameters to be determined. This model improves the correlation coefficient

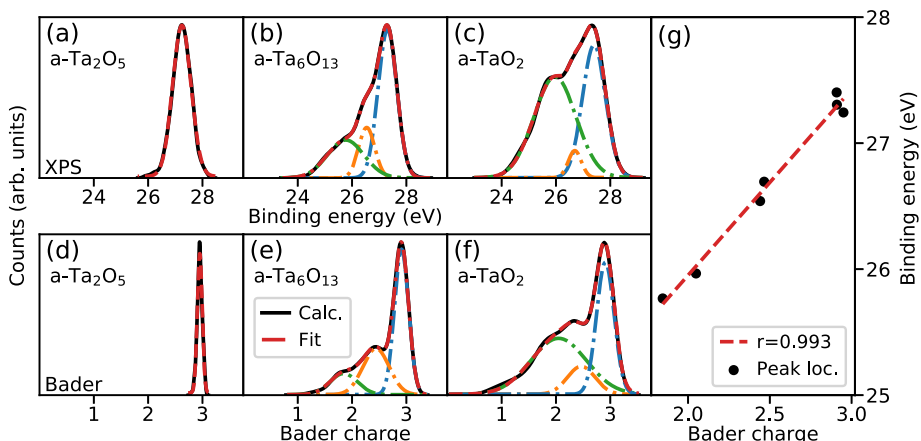


FIG. 5. [(a)–(c)] As-calculated (black), fitted (red), and deconvoluted (blue/orange/green) XPS spectra. [(d)–(f)] Same treatment for Bader charge spectra. (g) Comparison of Bader/XPS peak locations. Scales differ between y axes.

for a-Ta₂O₅ to 0.492 but has no impact on a-TaO₂ ($r = 0.881$). We conclude that the correlation between BE and Bader charge in both a-Ta₂O₅ and a-TaO₂ is more complex than can be accounted for in the above models (in contrast, the model of Ebadi *et al.*⁴⁵ performs well for the crystalline phases; see Fig. S4 of the [supplementary material](#)).

Instead, we decompose the Bader charge and XPS spectra of Fig. 3 (black dashed curves) into Gaussian components in order to compare the peak locations. We find that the best fit is achieved using a single Gaussian function for a-Ta₂O₅ and three Gaussian functions for a-Ta₆O₁₃ and a-TaO₂. We plot the decomposed BE peak values vs the Bader charge peak values in Fig. 5(g) and achieve a clear linear correlation with $r = 0.993$. We conclude that the XPS/Bader charge spectra of amorphous tantalum oxide are best understood as statistical entities, even when complete knowledge of the atomic arrangements is available.

IV. CONCLUSIONS

We have used AIMD and DFT to sample amorphous and oxygen-deficient Ta₂O₅. We have analyzed our a-Ta₂O_{5-x} systems with respect to relative formation energy, CDF, XPS, Bader charge, and coordination numbers. By drawing a convex hull over all 84 included structures, we show that oxygen-deficient a-Ta₂O₅ will preferentially separate into a-Ta₂O₅ and a-TaO₂. Additionally, the hitherto unknown stoichiometry of a-Ta₆O₁₃ showed energies significantly lower than other intermediate stoichiometries, which is linked to the existence of a vanadium-oxide phase with stoichiometry V₆O₁₃. Our CDF spectra showed that stoichiometries with a relatively low energy contain higher proportions of Ta atoms with six O neighbors within a radius of 2.5 Å.

By using Bader charges to model oxidation states explicitly, we found that Ta atoms in amorphous TaO₂ were divided into two different Bader charge spectra: one representing oxidation state +5 contributing to the Ta⁵⁺ peak and the other with a wide range of oxidation states contributing to the Ta⁴⁺ peak. Unlike the crystalline TaO₂ with a nominal Ta oxidation state +4, amorphous TaO₂ possesses disproportionated Ta atoms that make such a description less accurate. Our finding that the XPS spectrum of amorphous TaO₂ contains both Ta⁴⁺ and Ta⁵⁺ peaks challenges the conventional view of a-TaO_x spectra. Our results suggest that only the Ta₂O₅ stoichiometry may be reduced to a single oxidation state (+5). This finding is important for researchers wishing to use XPS spectra to estimate the composition of amorphous TaO_x samples and conceivably samples of other amorphous metal oxides as well. Finally, we determined the origin of the experimentally observed blueshift of the Ta 4f XPS peaks in amorphous Ta₂O₅ relative to its crystalline counterpart. The presence of under-coordinated Ta atoms and the longer Ta–O distances in amorphous TaO_x leads to lower Coulomb repulsion and hence higher binding energies.

As a final remark, we decompose our calculated XPS and Bader charge spectra in Gaussian components and find a linear correlation between peak locations. The correlation strength of this Gaussian model exceeds the strength of a linear model accounting for Coulomb interactions with the sixth nearest neighbors, suggesting that the more accurate way to analyze amorphous materials is by using statistical models. For future analysis of the Ta₆O₁₃ system, we

suggest studying the kinetic routes to reach this stoichiometry and other possible disproportionated states of the TaO_x system. To supplement this, it is also necessary to investigate the sensitivity of the sixfold Ta coordination with respect to addition and removal of oxygen, particularly for the Ta₆O₁₃ phase. Finally, while we have studied tantalum oxide exclusively, our approach can be expanded to any amorphous metal-oxide and shed light on the XPS spectra of these disordered structures.

SUPPLEMENTARY MATERIAL

See the [supplementary material](#) for more detailed information on amorphous tantalum oxides such as their densities, radial distribution function, XPS spectra of solid solution and phase separate phases, and a linear relation between binding energy and Bader charge for crystalline tantalum oxides.

ACKNOWLEDGMENTS

The authors acknowledge support from the Independent Research Fund Denmark (DRF) (Grant No. 6111-00145B). Additionally, the authors thank Henrik Høgh Kristoffersen of DTU Physics for valuable counsel.

DATA AVAILABILITY

The data that support the findings of this study are available from the corresponding author upon reasonable request.

REFERENCES

- ¹H. Akinaga and H. Shima, "Resistive random access memory (ReRAM) based on metal oxides," *Proc. IEEE* **98**, 2237–2251 (2010).
- ²I. H. Inoue and A. Sawa, "Resistive switchings in transition-metal oxides," in *Functional Metal Oxides: New Science and Novel Applications* (John Wiley & Sons, Ltd., 2013), Vol. 11, pp. 443–463.
- ³L. Chua, "Memristor—The missing circuit element," *IEEE Trans. Circuit Theory* **18**, 507–519 (1971).
- ⁴D. B. Strukov, G. S. Snider, D. R. Stewart, and R. S. Williams, *Nature* **453**, 80–83 (2008).
- ⁵H.-S. P. Wong, H.-Y. Lee, S. Yu, Y.-S. Chen, Y. Wu, P.-S. Chen, B. Lee, F. T. Chen, and M.-J. Tsai, "Metal-oxide RRAM," *Proc. IEEE* **100**, 1951–1970 (2012).
- ⁶Y. Hou, U. Celano, L. Goux, L. Liu, A. Fantini, R. Degraeve, A. Youssef, Z. Xu, Y. Cheng, J. Kang, M. Jurczak, and W. Vandervorst, "Sub-10 nm low current resistive switching behavior in hafnium oxide stack," *Appl. Phys. Lett.* **108**, 1–6 (2016).
- ⁷A. K. Singh, S. Blonkowski, and M. Kogelschatz, "Resistive switching study in HfO₂-based resistive memories by conductive atomic force microscopy in vacuum," *J. Appl. Phys.* **124**, 014501 (2018).
- ⁸M.-J. Lee, C. B. Lee, D. Lee, S. R. Lee, M. Chang, J. H. Hur, Y.-B. Kim, C.-J. Kim, D. H. Seo, S. Seo, U.-I. Chung, I.-K. Yoo, and K. Kim, "A fast, high-endurance and scalable non-volatile memory device made from asymmetric Ta₂O_{5-x}/TaO_{2-x} bilayer structures," *Nat. Mater.* **10**, 625–630 (2011).
- ⁹S. Kumar, C. E. Graves, J. P. Strachan, E. M. Grafals, A. L. D. Kilcoyne, T. Tyliczszak, J. N. Weker, Y. Nishi, and R. S. Williams, "Direct observation of localized radial oxygen migration in functioning tantalum oxide memristors," *Adv. Mater.* **28**, 2772–2776 (2016).
- ¹⁰D.-H. Kwon, K. M. Kim, J. H. Jang, J. M. Jeon, M. H. Lee, G. H. Kim, X.-S. Li, G.-S. Park, B. Lee, S. Han, M. Kim, and C. S. Hwang, "Atomic structure of conducting nanofilaments in TiO₂ resistive switching memory," *Nat. Nanotechnol.* **5**, 148–153 (2010).

- ¹¹ K.-L. Lin, T.-H. Hou, J. Shieh, J.-H. Lin, C.-T. Chou, and Y.-J. Lee, "Electrode dependence of filament formation in HfO₂ resistive-switching memory," *J. Appl. Phys.* **109**, 084104 (2011).
- ¹² M. S. Mattsson, G. A. Niklasson, K. Forsgren, and A. Hårsta, "A frequency response and transient current study of β -Ta₂O₅: Methods of estimating the dielectric constant, direct current conductivity, and ion mobility," *J. Appl. Phys.* **85**, 2185–2191 (1999).
- ¹³ P. W. C. Ho, F. O. Hatem, H. A. F. Almurib, and T. Nandha Kumar, "Comparison on TiO₂ and TaO₂ based bipolar resistive switching devices," in *IEEE International Conference on Electronic Design (IEEE, 2014)*, pp. 249–254.
- ¹⁴ C. Hsu, I. Wang, C. Lo, M. Chiang, W. Jang, C. Lin, and T. Hou, "Self-rectifying bipolar TaO_x/TiO₂ RRAM with superior endurance over 1012 cycles for 3D high-density storage-class memory," in *2013 Symposium on VLSI Technology (IEEE, 2013)*, pp. T166–T167.
- ¹⁵ C. Joseph, P. Bourson, and M. D. Fontana, "Amorphous to crystalline transformation in Ta₂O₅ studied by Raman spectroscopy," *J. Raman Spectrosc.* **43**, 1146–1150 (2012).
- ¹⁶ Y. Yang, S. Choi, and W. Lu, "Oxide heterostructure resistive memory," *Nano Lett.* **13**, 2908–2915 (2013).
- ¹⁷ Y. Li, S. Sanna, K. Norrman, D. V. Christensen, C. S. Pedersen, J. M. G. Lastra, M. L. Traulsen, V. Esposito, and N. Pryds, "Tuning the stoichiometry and electrical properties of tantalum oxide thin films," *Appl. Surf. Sci.* **470**, 1071–1074 (2019).
- ¹⁸ R. J. Bondi, B. P. Fox, and M. J. Marinella, "Role of atomistic structure in the stochastic nature of conductivity in substoichiometric tantalum pentoxide," *J. Appl. Phys.* **119**, 124101 (2016).
- ¹⁹ B. Xiao and S. Watanabe, "Oxygen vacancy effects on an amorphous-TaO_x-based resistance switch: A first principles study," *Nanoscale* **6**, 10169–10178 (2014).
- ²⁰ R. J. Bondi, M. P. Desjarlais, A. P. Thompson, G. L. Brennecke, and M. J. Marinella, "Electrical conductivity in oxygen-deficient phases of tantalum pentoxide from first-principles calculations," *J. Appl. Phys.* **114**, 203701 (2013).
- ²¹ R. J. Bondi and M. J. Marinella, "Oxidation state and interfacial effects on oxygen vacancies in tantalum pentoxide," *J. Appl. Phys.* **117**, 085308 (2015).
- ²² G. E. McGuire, G. K. Schweitzer, and T. A. Carlson, "Study of core electron binding energies in some group IIIA, VB, and VIB compounds," *Inorg. Chem.* **12**, 2450–2453 (1973).
- ²³ D. D. Sarma and C. N. R. Rao, "XPS studies of oxides of second- and third-row transition metals including rare earths," *J. Electron Spectrosc. Relat. Phenom.* **20**, 25–45 (1980).
- ²⁴ S. F. Ho, S. Contarini, and J. W. Rabalais, "Ion-beam-induced chemical changes in the oxyanions (moyⁿ⁻) and oxides (mox) where m = chromium, molybdenum, tungsten, vanadium, niobium and tantalum," *J. Phys. Chem.* **91**, 4779–4788 (1987).
- ²⁵ J. H. Thomas and L. H. Hammer, "A photoelectron spectroscopy study of CF₄/H₂ reactive ion etching residue on tantalum disilicide," *J. Electrochem. Soc.* **136**, 2004 (1989).
- ²⁶ N. Benito and C. Palacio, "Nanostructuring of Ta₂O₅ surfaces by low energy Ar⁺ bombardment," *Appl. Surf. Sci.* **351**, 753–759 (2015).
- ²⁷ R. Simpson, R. G. White, J. F. Watts, and M. A. Baker, "XPS investigation of monatomic and cluster argon ion sputtering of tantalum pentoxide," *Appl. Surf. Sci.* **405**, 79–87 (2017).
- ²⁸ G. Kresse and J. Hafner, "Ab initio molecular dynamics for liquid metals," *Phys. Rev. B* **47**, 558–561 (1993).
- ²⁹ G. Kresse and J. Hafner, "Ab initio molecular-dynamics simulation of the liquid-metal-amorphous-semiconductor transition in germanium," *Phys. Rev. B* **49**, 14251–14269 (1994).
- ³⁰ G. Kresse and J. Furthmüller, "Efficiency of ab-initio total energy calculations for metals and semiconductors using a plane-wave basis set," *Comput. Mater. Sci.* **6**, 15–50 (1996).
- ³¹ G. Kresse and J. Furthmüller, "Efficient iterative schemes for ab initio total-energy calculations using a plane-wave basis set," *Phys. Rev. B* **54**, 11169–11186 (1996).
- ³² P. E. Blöchl, "Projector-augmented wave method," *Phys. Rev. B* **50**, 17953–17979 (1994).
- ³³ J. P. Perdew, K. Burke, and M. Ernzerhof, "Generalized gradient approximation made simple," *Phys. Rev. Lett.* **77**, 3865–3868 (1996).
- ³⁴ S.-H. Lee, J. Kim, S.-J. Kim, S. Kim, and G.-S. Park, "Hidden structural order in orthorhombic Ta₂O₅," *Phys. Rev. Lett.* **110**, 235502 (2013).
- ³⁵ Y. Guo and J. Robertson, "Comparison of oxygen vacancy defects in crystalline and amorphous Ta₂O₅," *Microelectron. Eng.* **147**, 254–259 (2015).
- ³⁶ S. Kakio, K. Hosaka, M. Arakawa, Y. Ohashi, and J.-i. Kushibiki, "Surface acoustic wave properties of amorphous Ta₂O₅ and Nb₂O₅ thin films prepared by radio frequency sputtering," *Jpn. J. Appl. Phys.* **51**, 07GA01 (2012).
- ³⁷ J. Heyd, G. E. Scuseria, and M. Ernzerhof, "Hybrid functionals based on a screened Coulomb potential," *J. Chem. Phys.* **118**, 8207–8215 (2003).
- ³⁸ J. Heyd, G. E. Scuseria, and M. Ernzerhof, "Erratum: "Hybrid functionals based on a screened Coulomb potential" [J. Chem. Phys. 118, 8207 (2003)]," *J. Chem. Phys.* **124**, 219906 (2006).
- ³⁹ J. Heyd and G. E. Scuseria, "Efficient hybrid density functional calculations in solids: Assessment of the Heyd–Scuseria–Ernzerhof screened Coulomb hybrid functional," *J. Chem. Phys.* **121**, 1187–1192 (2004).
- ⁴⁰ R. F. W. Bader, *Atoms in Molecules: A Quantum Theory*, 1st ed. (Oxford University Press, 1994).
- ⁴¹ See <http://theory.cm.utexas.edu/henkelman/code/bader/> for scripts and further information.
- ⁴² N. Schönberg, W. G. Overend, A. Munthe-Kaas, and N. A. Sørensen, "An x-ray investigation of the tantalum-oxygen system," *Acta Chem. Scand.* **8**, 240–245 (1954).
- ⁴³ K.-A. Wilhelm, K. Waltersson, L. Kihlberg, G. Borch, K. Schaumburg, and L. Ehrenberg, "A refinement of the crystal structure V₆O₁₃," *Acta Chem. Scand.* **25**, 2675–2687 (1971).
- ⁴⁴ J. M. García-Lastra, P. L. Cook, F. J. Himpsel, and A. Rubio, "Communication: Systematic shifts of the lowest unoccupied molecular orbital peak in x-ray absorption for a series of 3d metal porphyrins," *J. Chem. Phys.* **133**, 151103 (2010).
- ⁴⁵ M. Ebadi, A. Nasser, M. Carboni, R. Younesi, C. F. N. Marchiori, D. Brandell, and C. M. Araujo, "Insights into the Li-metal/organic carbonate interfacial chemistry by combined first-principles theory and x-ray photoelectron spectroscopy," *J. Phys. Chem. C* **123**, 347–355 (2019).
- ⁴⁶ K.-A. Wilhelm and K. Waltersson, "On the crystal structure of a new vanadium oxide, V₄O₉," *Acta Chem. Scand.* **24**, 3409–3411 (1971).
- ⁴⁷ K. Waltersson, B. Forslund, K.-A. Wilhelm, S. Andersson, and J. Galy, "The crystal structure of V₃O₇," *Acta Crystallogr., Sect. B: Struct. Crystallogr. Cryst. Chem.* **30**, 2644–2652 (1974).
- ⁴⁸ S. Yamazaki, C. Li, K. Ohoyama, M. Nishi, M. Ichihara, H. Ueda, and Y. Ueda, "Synthesis, structure and magnetic properties of V₄O₉—A missing link in binary vanadium oxides," *J. Solid State Chem.* **183**, 1496–1503 (2010).

Publication 2

Prediction of crystalline Ta_4O_9 phase using first principles-based cluster expansion calculations

C. S. Pedersen, J. H. Chang, Y. Li, N. Pryds, J. M. García Lastra

APL Materials (Submitted)

Prediction of crystalline Ta₄O₉ phase using first principles-based cluster expansion calculations

Christian S ndergaard Pedersen, Jin Hyun Chang,^{a)} Yang Li, Nini Pryds, and Juan Maria Garcia Lastra^{b)}

Department of Energy Conversion and Storage, Technical University of Denmark, DK-2800 Kgs. Lyngby, Denmark.

(Dated: August 30, 2020)

Tantalum is the only element in periodic table Group 5 that lacks any experimental reports on the existence of reduced crystalline oxide between the pentoxide (Ta₂O₅) and dioxide (TaO₂). We computationally predict the existence of a novel tantalum oxide with Ta₄O₉ stoichiometry, which lies at the midpoint between Ta₂O₅ and TaO₂. The ground-state Ta₄O₉ structure was found through simulated annealing based on a cluster expansion model, which is trained using 186 density functional theory calculations. The newfound Ta₄O₉ material has space group number 10 (P 1 2/m 1), and it can be viewed as an oxygen-deficient λ -Ta₂O₅ structure in which oxygen vacancies aggregate pair-wise in nearest-neighbor sites. Ta_d-Ta_d bonds fill the spatial void of the oxygen vacancies, keeping the system non-magnetic and non-metallic. The synthesis of the new Ta₄O₉ crystal is deemed feasible through a controlled reduction of λ -Ta₂O₅. The reported Ta₄O₉ has the potential to open new avenues in catalysis and resistive switching device applications where the reduced tantalum oxides are broadly employed.

I. Introduction

Great attention has been focused on tantalum oxide since the turn of the millennium. Various phases of tantalum oxide have been investigated for use in photocatalysis,¹ electrocatalysis,² as coating in biomedical applications,³ and as resistive layer in Resistive Random Access Memory (ReRAM) devices.⁴ The most stable stoichiometry of the tantalum-oxide system is Ta₂O₅. Although Ta₂O₅ fabricated at room temperature is amorphous,⁵⁻⁷ samples are known to crystallize when fabricated at temperatures above $\sim 400^\circ\text{C}$.⁸ Likewise, annealing samples at temperatures between 500°C and 700°C also leads to crystallization.⁹⁻¹¹ Recently, Ta₂O₅ crystallites were observed in an electroformed nanofilament of a Resistive Random Access Memory device.¹² This finding raises a need for further investigation of crystalline tantalum oxide even in resistive switching applications where devices are usually reported as non-stoichiometric.^{4,13,14}

The atomic coordinates of low-temperature orthorhombic Ta₂O₅, or β -Ta₂O₅, were established in 2002 through Ritveld refinement of existing X-ray spectra.¹⁵ However, a density functional theory (DFT) study later revealed imaginary phonon frequencies for β -Ta₂O₅,¹⁶ which indicates a structural instability.¹⁷ Lee *et al.* instead proposed the orthorhombic λ phase and used DFT calculations to support their proposition.¹⁷ The λ phase yields a lower DFT energy than the β phase, as well as a more accurate prediction of the experimental band gap of 4.0 eV.¹⁸

Though Ta₂O₅ has received the most attention of all tantalum-oxide phases, reduced TaO_x phases constitute an important area of study as well. The work of Awaludin, Okajima, and Ohsaka,² for instance, characterized reduced Ta₂O_{5-x} for catalysis applications. The switching process in TaO_x ReRAM devices relies on the valence change mechanism,¹⁹ in which regions of the device are reduced until a conductive

filament is formed.^{4,20,21} The chemistry of reduced Ta₂O_{5-x}, though, has received far less attention than Ta₂O₅, with the exception of crystalline TaO₂. Despite being a metastable phase of the tantalum oxide system, TaO₂ has been observed both in the rutile phase²²⁻²⁵ and in a more complex tetragonal phase.²⁶

On a theoretical level, oxygen vacancies (v_O) in λ -phase Ta₂O₅ are well studied in terms of formation energy and defect orbitals²⁷ as well as migration barriers.^{28,29} However, the cited works have focused on the effects of singular v_O defects exclusively. In contrast, little is known about the behaviour of larger concentrations of v_O in crystalline Ta₂O₅, which is an important topic for ReRAM devices.¹⁹

In this letter, we report on a large-scale investigation of oxygen vacancy-defective Ta₂O₅ in the λ phase, for v_O concentrations from 0% to 25%. Using DFT calculations combined with cluster expansion (CE), we have found a new ground state of the TaO_x system with chemical formula Ta₄O₉, which is stable relative to phase separation of Ta₂O₅ and TaO₂. Exploring the atomic structure reveals that threefold coordinated oxygen vacancies aggregate in pairs at high ($\sim 10\%$) v_O -concentrations, with no decrease in coordination numbers anywhere in the system. Neighbouring Ta ions are sufficiently close that their d orbitals overlap, restoring their coordination number and stabilizing the pair defect. We believe the Ta₄O₉ phase may be synthesized through reduction of orthorhombic Ta₂O₅. Further, the discovery of the pair defect is an important contribution to ReRAM research, where Ta₂O₅ crystallites are known to form and v_O are created in large enough quantities to allow for pair-wise aggregation.

II. Computational Methods

We created in total 186 structures with v_O concentrations ranging from 0% to 25%, i.e. stoichiometric Ta₂O₅ to stoichiometric TaO₂ using the Cluster Expansion in Atomic Simulation Environment (CLEASE) software.³⁰ Working from the 14-atom unit cell of λ -Ta₂O₅ (see Lee *et al.*¹⁷) v_O distributions with various cell sizes and shapes were used to train the CE model, with the largest training structures containing 168

^{a)}Electronic mail: jchang@dtu.dk

^{b)}Electronic mail: jmgl@dtu.dk

atoms. For all distributions of v_O , we used DFT to relax the atomic forces. The correlation between the input atomic structures and the final formation energies calculated from DFT were then determined using the CLEASE code. The trained CE model was used to suggest the optimal arrangements of v_O for different concentrations, which were calculated using DFT with the same relaxation scheme.

All DFT calculations were performed using the Vienna Ab Initio Simulation Package (VASP).^{31–34} O and Ta atoms were described by PAW pseudopotentials³⁵ with valence electron configuration $5p^65d^36s^2$ and $2s^22p^4$, respectively. Unless noted otherwise, our calculations employed the Perdew-Burke-Ernzerhof (PBE) Generalized Gradient Approximation (GGA) to describe the electronic exchange and correlation.³⁶ Additional high-precision calculations were performed incorporating 25% exact exchange using the Heyd-Scuseria-Ernzerhof functional with a range-separation parameters of 0.2 (i.e., HSE06).^{37–39}

Our setup used a plane wave basis for the electronic wave functions with a cutoff energy of 520 eV. To sample the first Brillouin zone, we used Monkhorst-Pack grids⁴⁰ with a density of at least 3.5 per \AA^{-3} , shifted to the Γ point. For relaxations, the atomic coordinates were considered converged when interatomic forces were lower than $2.5 \times 10^{-2} \text{ eV \AA}^{-1}$, while for the electronic density the convergence threshold was $1.0 \times 10^{-5} \text{ eV}$.

The final CE model had a formation energy prediction accuracy of 16.5 meV/atom based on 10-fold cross-validation score. The optimal v_O arrangements were predicted using the CE model in conjunction with the simulated annealing technique. The structures with the $2 \times 2 \times 3$ supercell containing 168 atoms (vacancies were counted as atoms in this context) were used for generating the structures with the optimal v_O arrangements. The minimum-energy structure for each v_O concentration was found by gradually lowering the temperature from 5000 K to 1 K with 50000 attempted atomic swaps per temperature.

III. Results and Discussion

A. Convex hull and structural features

The results of our CE-enhanced structure search are summarized in the convex hull of Fig. 1. Each investigated structure is represented with its energy relative to phase separation of λ - Ta_2O_5 and TaO_2 . For TaO_2 , we use the 96-atom tetragonal cell of Khitrova, Klechkovskaya, and Pinsker²⁶ (labelled “K1967”). The ICSD lists two similar tetragonal structures from Khitrova, Klechkovskaya, and Pinsker’s work, with Coll. codes 60267 and 60268. We chose the latter because our calculations found it to have a slightly lower total energy per formula unit (f.u.). All of the energies reported in Fig. 1(a) are based on DFT calculations, while Fig. 1(b) shows the accuracy of the CE model used to predict the minimum-energy structure for each stoichiometry. Most remarkably, the hull shows preference for a solid solution of v_O , with a wide range of structures falling just below zero relative energy. The lowest point on the hull lies at $x = 0.5$, and has a stoichiometry of Ta_4O_9 ($\text{Ta}_2\text{O}_{5-0.5}$ in axis coordinates).

Apart from the K1967 model, Fig. 1(a) depicts two ad-

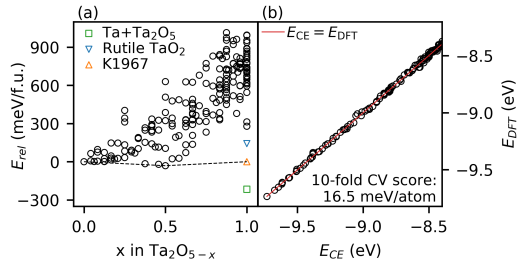


Figure 1. (a) Convex hull (dashed line) of the Ta_2O_5 - TaO_2 system. (b) Fit of the cluster expansion model performed by the CLEASE code. Black circles represent DFT-evaluated structures generated by the cluster expansion model.

ditional calculations with stoichiometries corresponding to $x = 1$ (i.e. TaO_2). The first, and overall most stable, is a phase separation into Ta and Ta_2O_5 (labelled “ $\text{Ta}+\text{Ta}_2\text{O}_5$ ”). We include this to show that TaO_2 itself is metastable with respect to decomposition into Ta and Ta_2O_5 . Second, we include the rutile TaO_2 structure documented by Schönberg *et al.*, Niebuhr and Terao^{22–24} (labelled “Rutile TaO_2 ”).

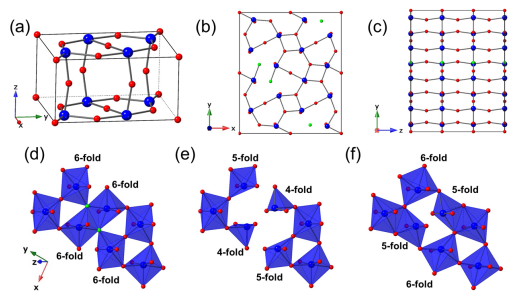


Figure 2. (a) Primitive cell of λ - Ta_2O_5 . (b-c) Vacancy distribution of the Ta_4O_9 phase prior to relaxation: (b) XY plane and (c) ZY plane. (d-f) Zoomed-in view of a v_O pair; (d) shows the v_O pair site before relaxation, (e) shows the empty v_O pair site before relaxation, and (f) shows the defect site after relaxation. Colors represent O (red), Ta (blue) and v_O (green).

The comparison to $\text{Ta}+\text{Ta}_2\text{O}_5$ shows that our newfound Ta_4O_9 phase is unstable compared with that reference. However, the two TaO_2 phases marked with triangles in Fig. 1(a) have been synthesized experimentally despite lying $\sim 358 \text{ meV/fu}$ (rutile) and $\sim 216 \text{ meV/fu}$ (Khitrova, Klechkovskaya, and Pinsker) above phase-separated $\text{Ta}+\text{Ta}_2\text{O}_5$ according to our calculations. Since the Ta_4O_9 structure reported here is stable with respect to λ - Ta_2O_5 and Khitrova, Klechkovskaya, and Pinsker’s TaO_2 -structure, it should be synthesizable. The crystalline Ta_4O_9 structure described here is a form of v_O -defective λ - Ta_2O_5 by construction. Hence, the newfound Ta_4O_9 structure can be reached by reduction of crystalline Ta_2O_5 .

Having established a new metastable state in the TaO_x system, we set to work characterizing its atomic structure. The crystal structure of $\lambda\text{-Ta}_2\text{O}_5$ is depicted in Fig. 2(a), and consists of planes of Ta_2O_3 (XY plane in Fig. 2(a)) joined in the transverse direction (Z axis in Fig. 2(a)) by Ta-O chains, as described by Calvert and Draper in 1962,⁴¹ and by Lehovc in 1964.⁹ The arrangement of oxygen vacancies in the Ta_4O_9 structure prior to relaxation is shown for the XY and ZY planes in Fig. 2(b-c). Within the Ta_2O_3 planes, vacancies exclusively form in threefold coordinated positions and aggregate in a pair-wise manner with 2.50 Å distance between them. The in-plane distance between symmetry-equivalent v_{O} 's is 9.69 Å, which is half the diagonal of the XY plane of the supercell; i.e. $1/2 [(12.50\text{Å})^2 + (14.80\text{Å})^2]^{1/2} = 9.69\text{Å}$. The minimum distance between symmetry inequivalent v_{O} in different pairs is 7.21 Å. This implies that, while v_{O} aggregate pair-wise, pairs arrange themselves with maximal pair-to-pair spacing in the plane. v_{O} 's form in the same lattice position in each Ta_2O_3 plane, resulting in a chain-like aggregation in the out-of-plane direction with v_{O} pairs spaced 3.87 Å apart (see Fig. 2(c)).

Fig. 2(d-f) depicts the local environment surrounding two neighbouring v_{O} 's. The removal of two neighboring O atoms leaves the two nearest Ta atoms only fourfold coordinated and the two second-nearest Ta atoms fivefold coordinated as shown by the polyhedra in frame (e). However, during the structural rearrangement, nearby twofold coordinated O atoms shift closer to the O-deprived Ta atoms. As seen in (f), this raises the coordination number of all involved atoms by 1; the fourfold coordinated Ta atoms become fivefold coordinated, the fivefold coordinated Ta atoms become sixfold coordinated, and the shifted twofold coordinated O atoms become threefold coordinated. The rectangular arrangement of Ta ions surrounding the pair site is intact, albeit slightly compressed. The inter-planar distance has increased by 0.04 Å, from 3.83 Å to 3.87 Å which is a relatively minor expansion of $\sim 1\%$, likely owing to the fact that the Ta-O chains in the out-of-plane direction are intact.

The newfound Ta_4O_9 structure can be reduced to a primitive cell with 26 atoms, which is depicted in Fig. 3. This primitive structure contains two neighboring v_{O} , and belongs to space group number 10 (P2/m). The lattice vectors and Wyckoff positions for this structure are listed in Table I.

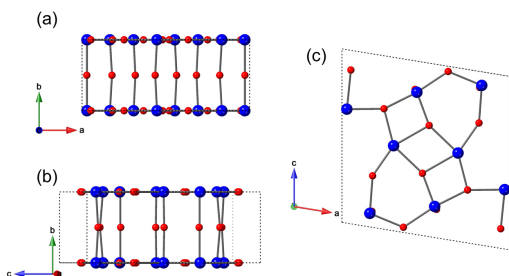


Figure 3. Primitive cell of the ground-state structure of Ta_4O_9 .

Table I. Wyckoff positions for the primitive Ta_4O_9 cell. Lattice parameters are: $|\mathbf{a}| = 9.29\text{Å}$, $|\mathbf{b}| = 3.87\text{Å}$, $|\mathbf{c}| = 9.47\text{Å}$, with angle $\beta = 99.3^\circ$.

Element	u	v	w	Wyckoff
O	0.7493	0.0	0.3052	2m
O	0.9470	0.0	0.1133	2m
O	0.9716	0.5	0.3483	2n
O	0.5200	0.0	0.6410	2m
O	0.6825	0.5	0.5048	2n
O	0.1785	0.5	0.0920	2n
O	0.4362	0.5	0.8360	2n
O	0.3665	0.0	0.0300	2m
O	0.8173	0.0	0.7024	2m
Ta	0.9708	0.0	0.3427	2m
Ta	0.6922	0.0	0.5094	2m
Ta	0.1661	0.0	0.0784	2m
Ta	0.4469	0.0	0.8207	2m

B. Electronic properties of Ta_4O_9

We now proceed to characterize the electronic properties of the newfound primitive cell, beginning with the band structure and orbital-Projected Density of States (PDOS). Since PBE is known to underestimate band gaps, we performed a single-point calculation with the Heyd-Scuseria-Ernzerhof (HSE) functional on the PBE-relaxed structure, using a k grid reduced to $(2 \times 5 \times 2)$ from $(3 \times 6 \times 3)$. The Ta_4O_9 band structure visualized in Fig. 4(a) exhibits two bands localized in the middle of the gap, resulting from the two removed O atoms. The PDOS spectrum in Fig. 4(b) shows that the orbital character of the defect state is primarily Ta d, secondarily O p and tertiarily Ta s (see the inset). The band edges of Ta_4O_9 are otherwise well aligned with those of Ta_2O_5 . The defect state is filled according to the location of the Fermi energy for this state, with an energy gap of 1.12 eV between the defect state and the conduction band minimum.

A thorough analysis of the nature of these two mid-gap bands may help to understand the particular stability of the oxygen divacancy center that gives rise to the Ta_4O_9 structure. In the following, we analyze the wave function at the Γ point of the two mid-gap states, which we will refer to as Highest Valence Band (HVB) and second-highest Valence Band (SHVB).

From an electrostatic point of view, it is expected that the four electrons needed to compensate the two O^{2-} vacancies will localize in the two TaO_5 complexes (the only Ta left fivefold coordinated after the reconstruction). This localization would imply a change in the nominal oxidation state of these two Ta ions from +5 to +3, thus filling some of their d orbitals. Another important consideration is that the two TaO_5 complexes, which adopt a distorted square pyramidal shape, are very close to each other with just a void region between the bases of the two pyramids. In this scenario, the distance between the two pentacoordinated Ta ions is only 2.94 Å, and substantial overlap between their corresponding d orbitals may occur. A significant overlap of the d orbitals is corroborated by the wave functions of the SHVB and HVB shown in Fig. 5.

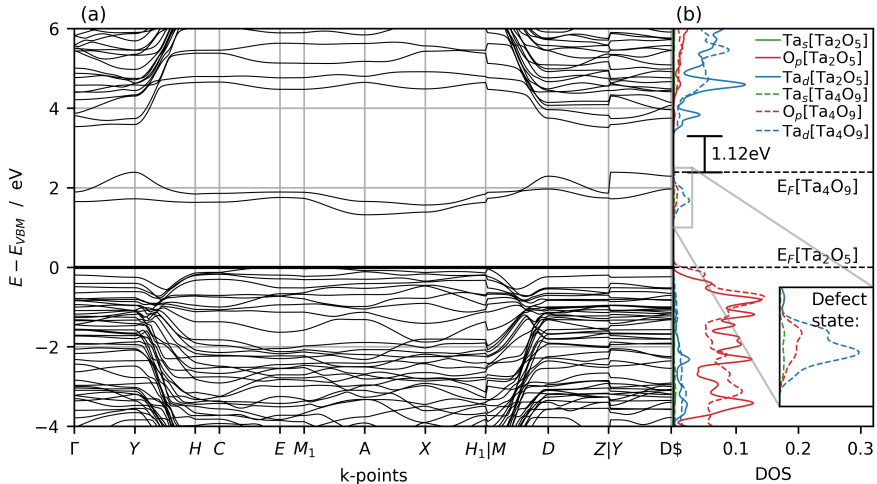


Figure 4. (a) Band structure of Ta_4O_9 , and (b) PDOS for both $\lambda\text{-Ta}_2\text{O}_5$ and Ta_4O_9 . Inset in (b) zooms in on the defect state of Ta_4O_9 .

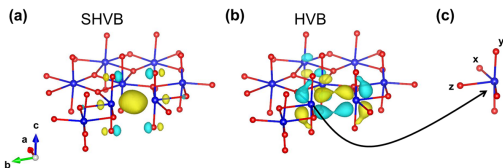


Figure 5. (a) SHVB and (b) HVB of the pair defect calculated at the Γ point. Isosurface colors represent positive and negative signs, respectively. (c) Local axis on a fivefold coordinated Ta ion.

HVB has a character of a bonding orbital between the d_{yz} orbitals of the two pentacoordinate Ta ions (the local axis of the distorted square pyramids is shown in Fig. 5(c)). SHVB has a character of a bonding orbital between the $d_{3z^2-r^2}$ orbitals of the two pentacoordinated Ta ions. The equatorial part of the $d_{3z^2-r^2}$ orbitals has disappeared due to the slight hybridization with the Ta s orbitals (see inset of Fig. 4(b)). The bonding interaction between the Ta d orbitals in SHVB is so strong that it makes the state resemble an F center, i.e. a state fully localized in the void left by an anionic vacancy. This intense interaction between the d orbitals of the two TaO_5 complexes restores the missing bonds to complete full sixfold coordination for every Ta ion in the system, conferring the Ta_4O_9 structure unique stability.

IV. Conclusions

We have combined DFT calculations and CE to perform a structure search for v_{O} -defective $\lambda\text{-Ta}_2\text{O}_5$. We found a phase with stoichiometry Ta_4O_9 at the midpoint between Ta_2O_5 and TaO_2 , which is stable with respect to phase separation of the latter two structures. The Ta_4O_9 structure has a highly or-

dered defect distribution with five distinct features: i) vacancies form exclusively on threefold coordinated sites, ii) vacancies aggregate pair-wise on neighboring sites, iii) vacancy pairs are arranged with maximal in-plane spacing, iv) vacancy pairs form on equivalent sites in successive planes, mimicking the chain-like atomic order in the out-of-plane direction. v) Nearby twofold coordinated O atoms shift closer to undercoordinated Ta atoms, which are thus compensated for their loss in coordination number due to the defects. The high degree of order in the defect structure allowed us to reduce the ground state supercell to a monoclinic primitive cell consisting of 26 atoms (Ta_8O_{18}).

We further characterized the ground state structure with respect to PDOS and frontier orbital wave functions. The pair defect results in a localized and filled mid-gap defect state with predominantly Ta d orbital character and lesser contributions from O p and Ta s. Spatially, the wave function associated with the defect pair is localized between the individual v_{O} sites, and projected primarily onto the d orbitals of the nearest Ta neighbors. The two Ta atoms closest to the defect site are sufficiently close that these d orbitals overlap, forming a bonding orbital. This metal bonding restores the Ta atoms to full sixfold coordination, explaining the extraordinary stability of the pair defect. Finally, the newfound ground state is non-magnetic and non-metallic.

The most immediate study concerning the Ta_4O_9 phase is to find experimental pathways to synthesize it. If successful, it is worthwhile to investigate the Ta_4O_9 surface for catalysis applications, since the nature and concentration of the defect states may have a profound impact on the catalytic properties of the surface. Finally, it is worth investigating whether the pair-defects found for Ta_4O_9 may linger in ReRAM device crystallites when switching to the OFF state, and if so, how they might influence crucial parameters like ON/OFF current

ratio and device longevity.

Acknowledgments

The authors acknowledge support from the Independent Research Fund Denmark (DFF), Grant No. 6111-00145B.

Data Availability

The data that support the findings of this study are available from the corresponding author upon reasonable request.

References

- G. Guo and J. Huang, "Preparation of mesoporous tantalum oxide and its enhanced photocatalytic activity," *Materials Letters* **65**, 64–66 (2011).
- Z. Awaludin, T. Okajima, and T. Ohsaka, "Preparation of reduced tantalum pentoxide by electrochemical technique for oxygen reduction reaction," *Journal of Power Sources* **268**, 728–732 (2014).
- T. Beline, J. H. D. da Silva, A. O. Matos, N. F. Azevedo Neto, A. B. de Almeida, F. H. Nociti Junior, D. M. G. Leite, E. C. Rangel, and V. A. R. Barao, "Tailoring the synthesis of tantalum-based thin films for biomedical application: Characterization and biological response," *Materials Science and Engineering: C* **101**, 111–119 (2019).
- M.-J. Lee, C. B. Lee, D. Lee, S. R. Lee, M. Chang, J. H. Hur, Y.-B. Kim, C.-J. Kim, D. H. Seo, S. Seo, U.-I. Chung, I.-K. Yoo, and K. Kim, "A fast, high-endurance and scalable non-volatile memory device made from asymmetric $\text{Ta}_2\text{O}_5\text{-x}/\text{TaO}_{2-x}$ bilayer structures," *Nature Materials* **10**, 625–630 (2011).
- C. Joseph, P. Bourson, and M. D. Fontana, "Amorphous to crystalline transformation in Ta_2O_5 studied by raman spectroscopy," *Journal of Raman Spectroscopy* **43**, 1146–1150 (2012).
- Y. Yang, S. Choi, and W. Lu, "Oxide heterostructure resistive memory," *Nano Letters* **13**, 2908–2915 (2013).
- Y. Li, S. Sanna, K. Norrman, D. V. Christensen, C. S. Pedersen, J. M. G. Lastra, M. L. Traulsen, V. Esposito, and N. Pryds, "Tuning the stoichiometry and electrical properties of tantalum oxide thin films," *Applied Surface Science* **470**, 1071–1074 (2019).
- S. Uthanna, S. V. J. Chandra, G. M. Rao, and J. F. Pierson, "Influence of substrate temperature on the structural, dielectric and optical properties of RF magnetron sputtered Ta_2O_5 films," *IOP Conference Series: Materials Science and Engineering* **8**, 012025 (2010).
- K. Lehovec, "Lattice structure of $\beta\text{-Ta}_2\text{O}_5$," *Journal of the Less Common Metals* **7**, 397–410 (1964).
- P.-H. Chang and H.-Y. Liu, "Structures of tantalum pentoxide thin films formed by reactive sputtering of Ta metal," *Thin Solid Films* **258**, 56–63 (1995).
- Y. Li, Y. E. Suyolcu, S. Sanna, D. V. Christensen, M. L. Traulsen, E. Stamate, C. S. Pedersen, P. A. van Aken, J. M. García Lastra, V. Esposito, and N. Pryds, "Tuning the resistive switching in tantalum oxide-based memristors by annealing," *AIP Advances* **10**, 065112 (2020).
- Y. Ma, J. M. Goodwill, D. Li, D. A. Cullen, J. D. Poplawsky, K. L. More, J. A. Bain, and M. Skowronski, "Stable metallic enrichment in conductive filaments in TaO_x -based resistive switches arising from competing diffusive fluxes," *Advanced Electronic Materials* **5**, 1800954 (2019).
- Z. Wei, Y. Kanzawa, K. Arita, Y. Katoh, K. Kawai, S. Muraoka, S. Mitani, S. Fujii, K. Katayama, M. Iijima, T. Mikawa, T. Ninomiya, R. Miyanaga, Y. Kawashima, K. Tsuji, A. Himeno, T. Okada, R. Azuma, K. Shimakawa, H. Sugaya, T. Takagi, R. Yasuhara, K. Horiba, H. Kumigashira, and M. Osahima, "Highly reliable TaO_x reram and direct evidence of redox reaction mechanism," in *2008 IEEE International Electron Devices Meeting (IEDM, 2008)* pp. 1–4.
- J. J. Yang, J. P. Zhang, F. Miao, M. D. Pickett, R. D. Kelley, G. Medeiros-Ribeiro, and R. S. Williams, "High switching endurance in TaO_x memristive devices," *Applied Physics Letters* **97**, 232102 (2010).
- L. Aleshina and S. Loginova, "Rietveld analysis of x-ray diffraction pattern from $\beta\text{-Ta}_2\text{O}_5$ oxide," *Crystallography Reports* **47**, 415–419 (2002).
- W. Andreoni and C. A. Pignedoli, " Ta_2O_5 polymorphs: Structural motifs and dielectric constant from first principles," *Applied Physics Letters* **96**, 062901 (2010).
- S.-H. Lee, J. Kim, S.-J. Kim, S. Kim, and G.-S. Park, "Hidden structural order in orthorhombic Ta_2O_5 ," *Physical Review Letters* **110**, 235502 (2013).
- R. M. Fleming, D. V. Lang, C. D. Jones, M. L. Steigerwald, D. W. Murphy, G. B. Alers, Y. H. Wong, R. B. Van Dover, J. R. Kwo, and A. M. Sergent, "Defect dominated charge transport in amorphous Ta_2O_5 thin films," *Journal of Applied Physics* **88**, 850–862 (2000).
- R. Waser, R. Dittmann, G. Staikov, and K. Szot, "Redox-based resistive switching memories – nanoionic mechanisms, prospects, and challenges," *Advanced Materials* **21**, 2632–2663 (2009).
- G.-S. Park, Y. B. Kim, S. Y. Park, X. S. Li, S. Heo, M.-J. Lee, M. Chang, J. H. Kwon, M. Kim, U.-I. Chung, R. Dittmann, R. Waser, and K. Kim, "In situ observation of filamentary conducting channels in an asymmetric $\text{Ta}_2\text{O}_5\text{-x}/\text{TaO}_{2-x}$ bilayer structure," *Nature Communications* **4**, 1–9 (2013).
- P. W. C. Ho, F. O. Hatem, H. A. F. Almurib, and T. N. Kumar, "Comparison on TiO_2 and TaO_2 based bipolar resistive switching devices," in *2014 2nd International Conference on Electronic Design (ICED)* (IEEE, 2014) pp. 249–254.
- N. Schönberg, W. G. Overend, A. Munthe-Kaas, and N. A. Sörensen, "An x-ray investigation of the tantalum-oxygen system," *Acta Chemica Scandinavica* **8**, 240–245 (1954).
- J. Niebuhr, "Die niederen oxide des tantalums," *Journal of the Less-Common Metals* **10**, 312–322 (1966).
- N. Terao, "Structure des oxides de tantalum," *Japanese Journal of Applied Physics* **6**, 21–34 (1967).
- Y. Muraoka, Y. Fujimoto, M. Kameoka, Y. Matsuura, M. Sunagawa, K. Terashima, T. Wakita, and T. Yokoya, "Preparation of TaO_2 thin films using NbO_2 template layers by a pulsed laser deposition technique," *Thin Solid Films* **599**, 125–132 (2016).
- A. N. Khitrova, V. V. Klechkovskaya, and J. Pinsker, "Electron diffraction investigation of tantalum dioxide in thin films," *Kristallografiya* **12**, 1044–1050 (1967).
- Y. Guo and J. Robertson, "Oxygen vacancy defects in Ta_2O_5 showing long-range atomic re-arrangements," *Applied Physics Letters* **104**, 112906 (2014).
- H. Jiang and D. A. Stewart, "Enhanced oxygen vacancy diffusion in Ta_2O_5 resistive memory devices due to infinitely adaptive crystal structure," *Journal of Applied Physics* **119**, 134502 (2016).
- J.-H. Hur, "Theoretical studies on oxygen vacancy migration energy barrier in the orthorhombic λ phase Ta_2O_5 ," *Computational Materials Science* **169**, 109148 (2019).
- J. H. Chang, D. Kleiven, M. Melander, J. Akola, J. M. García-Lastra, and T. Vegge, "CLEASE: a versatile and user-friendly implementation of cluster expansion method," *Journal of Physics: Condensed Matter* **31**, 325901 (2019).
- G. Kresse and J. Hafner, "Ab initio molecular dynamics for liquid metals," *Phys. Rev. B* **47**, 558–561 (1993).
- G. Kresse and J. Hafner, "Ab initio molecular-dynamics simulation of the liquid-metal-amorphous-semiconductor transition in germanium," *Phys. Rev. B* **49**, 14251–14269 (1994).
- G. Kresse and J. Furthmüller, "Efficiency of ab-initio total energy calculations for metals and semiconductors using a plane-wave basis set," *Computational Materials Science* **6**, 15–50 (1996).
- G. Kresse and J. Furthmüller, "Efficient iterative schemes for ab initio total energy calculations using a plane-wave basis set," *Phys. Rev. B* **54**, 11169–11186 (1996).
- P. E. Blöchl, "Projector-augmented wave method," *Phys. Rev. B* **50**, 17953–17979 (1994).
- J. P. Perdew, K. Burke, and M. Ernzerhof, "Generalized gradient approximation made simple," *prl* **77**, 3865–3868 (1996).
- J. Heyd, G. E. Scuseria, and M. Ernzerhof, "Hybrid functionals based on a screened coulomb potential," *The Journal of Chemical Physics* **118**, 8207–8215 (2003).
- J. Heyd, G. E. Scuseria, and M. Ernzerhof, "Erratum: "hybrid functionals based on a screened coulomb potential" [j. chem. phys. 118, 8207 (2003)]," *The Journal of Chemical Physics* **124**, 219906 (2006).
- J. Heyd and G. E. Scuseria, "Efficient hybrid density functional calculations in solids: Assessment of the heyd-scuseria-ernzerhof screened coulomb hybrid functional," *The Journal of Chemical Physics* **121**, 1187–1192 (2004).
- H. J. Monkhorst and J. D. Pack, "Special points for brillouin-zone integrations," *Phys. Rev. B* **13**, 5188–5192 (1976).

⁴¹L. D. Calvert and P. H. G. Draper, "A proposed structure for annealed anodic oxide films of tantalum," *Canadian Journal of Chemistry* **40**, 1943–1950 (1962).

This thesis is submitted in candidacy for the degree Doctor of Philosophy at the Technical University of Denmark (DTU). It presents work carried out in the period January 2017 to August 2020 at the Department for Energy Conversion and Storage, Section for Atomic Scale Materials Modeling.

Department of Energy Conversion and Storage

DTU Energy

Technical University of Denmark

Anker Engelunds Vej, Building 301

2800 Kgs. Lyngby

info@dtu.dk

www.energy.dtu.dk